



# **Nucleation kinetics and flow-driven crystallization of lithium phosphate**

Ph.D. Dissertation

**Michael Emmanuel**

Supervisors:

Dr. Ágota Tóth

Dr. Dezső Horváth

**Doctoral School of Chemistry**

University of Szeged, Faculty of Science and Informatics,  
Department of Physical Chemistry and Materials Science

Szeged, 2022

# Contents

<b>1</b>	<b>Introduction</b>	<b>3</b>
<b>2</b>	<b>Literature Review</b>	<b>7</b>
2.1	Crystallization/Precipitation . . . . .	7
2.2	Classical Nucleation Theory . . . . .	9
2.3	Mixing conditions for precipitation . . . . .	15
2.3.1	Precipitation in a well-stirred system . . . . .	15
2.3.2	Precipitation induced by flow . . . . .	17
2.4	2-dimensional precipitation in microfluidic system . . . . .	19
2.5	3-dimensional precipitation . . . . .	22
<b>3</b>	<b>Aims</b>	<b>26</b>
<b>4</b>	<b>Materials and Methods</b>	<b>28</b>
4.1	Materials . . . . .	28
4.2	Methods . . . . .	28
4.2.1	Well-stirred system . . . . .	28
4.2.2	Flow-driven temporal evolution in microfluidics . . . . .	29
4.2.3	Flow-driven 3D precipitation system . . . . .	30
<b>5</b>	<b>Analytical Methods</b>	<b>31</b>
5.1	Determination of induction time . . . . .	31
5.2	Image Analysis . . . . .	32
5.3	Techniques . . . . .	33
5.3.1	Ultraviolet-visible spectrophotometry . . . . .	33
5.3.2	Scanning electron microscopy . . . . .	33
5.3.3	X-ray diffractometry . . . . .	33
5.3.4	Density measurement . . . . .	34
5.3.5	Viscosity measurement . . . . .	34
5.3.6	Conductivity measurement . . . . .	35
<b>6</b>	<b>Results and Discussions</b>	<b>37</b>
6.1	Speciation of precipitates and complex ions . . . . .	37

6.2	Nucleation in well-stirred system . . . . .	41
6.3	Quasi 2D crystallization in microchannel . . . . .	50
6.3.1	Modeling of the concentration field in the microchannel . . . . .	57
6.3.2	Microstructure of lithium phosphate from microchannels . . . . .	59
6.4	3D temporal evolution of precipitate structure . . . . .	61
<b>7</b>	<b>Summary</b>	<b>68</b>
	<b>Glossary</b>	<b>71</b>
	<b>Bibliography</b>	<b>73</b>
	<b>Appendix</b>	<b>91</b>
<b>I</b>	<b>Pressure and injection rate parameters</b>	<b>91</b>
<b>II</b>	<b>Determination of Induction time</b>	<b>92</b>
<b>III</b>	<b>Converting and renaming image list files</b>	<b>94</b>
<b>IV</b>	<b>ImageJ Macro for measuring particle size</b>	<b>95</b>
<b>V</b>	<b>Calculation of the speciation of ions</b>	<b>99</b>
	<b>Acknowledgements</b>	<b>102</b>

# Chapter 1

## Introduction

The development of rechargeable batteries [1, 2] and the high demand for electric cars in recent years have led to increased popularity of lithium ion. Lithium is not only useful in the battery technology but also has gained widespread industrial interest. It is an effective desiccant [3] for ceramics and glass due to the high hygroscopy of its bromide and chloride salts. The hollow-shaped lithium phosphate catalyzes propylene oxide isomerization [4], lithiated esters are high temperature resistant lubricants [5], and various lithium salts are used as medicine for the treatments of mental illnesses [6].

With all these applications of lithium, the common source depends on its mining from minerals [7], certain soil [8], underground [9], or geothermal waters [10, 11]. These activities are costly and detrimental to the environment, hence recovery from the spent lithium ion batteries is a very important step in using a completely environment-friendly source of energy [8, 12].

With the increasing need for energy, in 2021 battery manufacturing consumed 74% of the total lithium production [13]. This increases the burden on the source of lithium. Therefore, understanding the formation of its ions from solution will increase the efficacy of the recovery process to boost production. According to a report, there is hardly less than 1.0% of reused lithium ions. This is in part due to its large deposit that is being extracted worldwide to meet the ever-increasing necessity [14], with less regard to the environmental impact. The lack of recycling of lithium ions is also related to the higher expenses involved, compared to mining from its minerals [15]. In the recovery of lithium ion, the spent materials are converted through a series of leaching steps, and then converting into the battery grade precipitates as carbonates [16], phosphates [17, 18], and hydroxides [19].

Global greenhouse gas emission is increasing with time, and one of the major culprits is energy generation for the increasing industrialization [20]. Industrialization in developing countries and fast-growing global economies are the major contributors to the global trend [21, 22]. The whole world is doing its best to reduce this global catastrophe by designing ways of obtaining green and renewable forms of energy [23]. The development of effective alternative energy sources, which are green and safe will go a long way to curb global

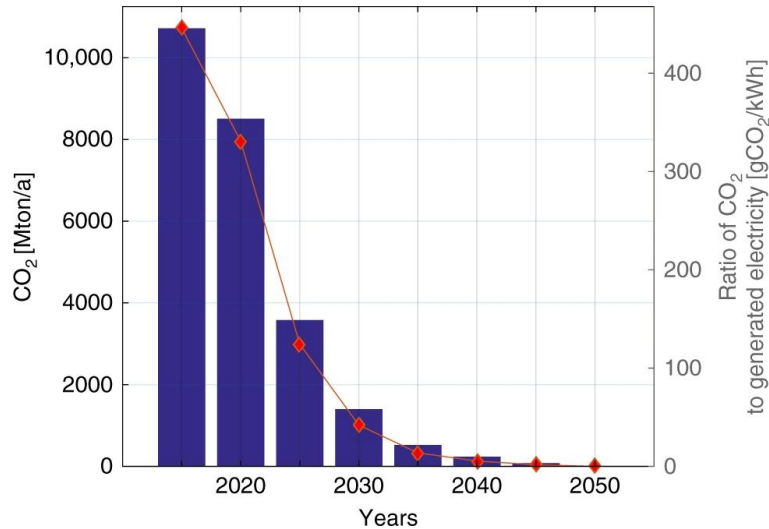


Figure 1.1: Global greenhouse gas emission for the transmission period 2015-2050, reproduced from ref. [29]

warming. Recycling is one important step toward reducing greenhouse gas emission.

Recycling entails the re-conversion of spent materials for reuse in the same form or converted into another useful form leading to easing the extraction of raw materials [24]. It is estimated that there is about 13 million tons of economically recoverable lithium metal reserve all over the world [25]. The consumption of lithium in 2015 increased from around 34 kilotons to 49 kilotons in 2019, with the need for traditional battery production soaring from 25% to 71% within this period [26]. Australia, Argentina, Chile, China, and Zimbabwe in 2019, according to a report [26], mined a total of 68 kilotons of lithium [27]. China, Japan, and South Korea have the highest lithium consumption because of their electric car manufacturing and other electronic wares. Even though China produced about 7,500 tons of lithium in 2019, more lithium had to be imported to meet their yearly requirement [28]. Modeling results revealed that by the end of 2050, it is possible to reach 100% zero-carbon emission (Fig. 1.1) [29], meaning total independence from fossil fuels. This development will increase the demand for lithium and other elements used for energy storage, leading to increased excavation of mines. These mining activities are quite detrimental to the environment: from the destruction of landscape to the pollution of air and water by heavy-duty machinery and waste dump [30, 31]. In the future, with the growing world population and requirement for energy, the sources of lithium will gradually deplete, hence recycling will be of utmost importance to balance demand and supply.

As an important step to complement the high need for lithium ion batteries, several measures are employed to reuse the spent lithium ion batteries and save the environment in the process. Recycling of this ion depends mostly on precipitation processes to convert the spent lithium ions to reusable form. In a laboratory scale lithium ion battery recycling the following processes could be employed. First, the lithium materials are sorted and separated

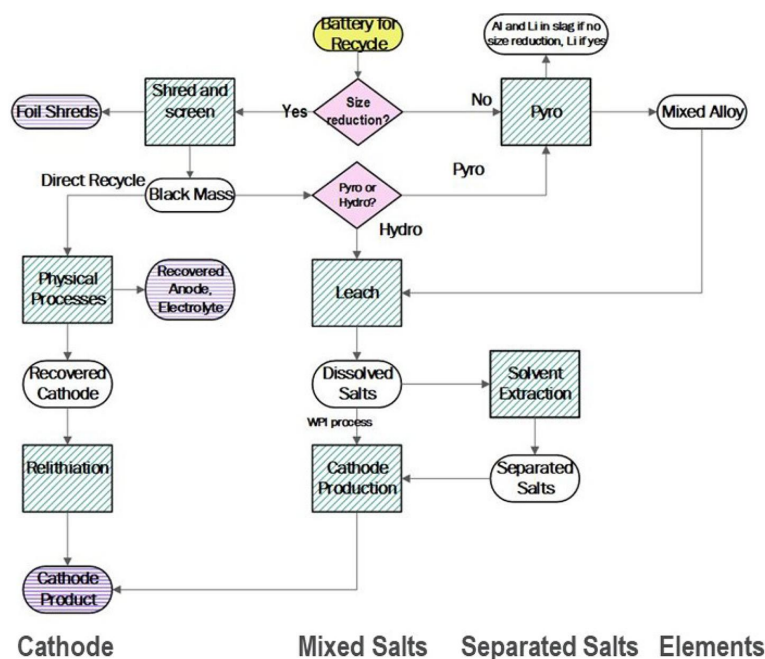


Figure 1.2: Possible recycling paths for lithium ion batteries, reproduced with permission from ref. [33]

from other chemical waste parts of the battery. After sorting, the active materials could be separated using N-methylpyrrolidone at 100 °C for 1 hour [32]. This step separates the polyvinylidene difluoride binder from the support and allows the collection of the copper and aluminium used, which after proper cleaning could be directly reused. Next is the lithium cobalt oxide dissolution, followed by the precipitation of cobalt hydroxide and filtration. The filtrate solution containing lithium chloride is then precipitated using phosphate or carbonate solutions. Due to the complexity of lithium ion batteries, so many other paths could be taken to achieve better recycling (Fig. 1.2) [33–38]. The common step in all the different routes is the precipitation step.

In order to understand and improve this recovery process, it is important to know the mechanism of crystal formation and growth. These mechanisms depend on several factors, such as supersaturation, temperature, presence of foreign materials, and mixing condition. During a rapid cooling crystallization, the rate of nucleation increases exponentially with higher supersaturation [39, 40]. Change in temperature also affects the energetics of the process and could be important in polymorph selection. For example, in the formation of calcium carbonate crystals, at room temperature, calcite and vaterite could easily be formed, whereas, at higher temperatures, aragonites appear in the mix [41].

A thermodynamic investigation on the recovery of lithium using phosphate precipitation was previously carried out. Results from this study showed that lithium phosphate can precipitate within a pH window of 11–13. It is reported that the lithium phosphate formed, could be decomposed by the addition of  $\text{FeCl}_3 \cdot 6\text{H}_2\text{O}$  at a pH range of 2.5–3.5 [42]. Although this

study considers the pH range and the thermodynamics for the recovery of lithium phosphate, it does not provide any information about its nucleation. In another study to recover lithium from spent lithium ion batteries, precipitation and electro dialysis are conducted. The lithium present in the leachate solution is precipitated by the addition of  $\text{Na}_3\text{PO}_4$  after the removal of other impurity metals such as  $\text{Al}^{3+}$ ,  $\text{Fe}^{2+}$ ,  $\text{Cu}^{2+}$ , at a pH of 5.3. Increasing the pH to about 7 favors the precipitation of  $\text{Zn}^{2+}$ ,  $\text{Ni}^{2+}$ ,  $\text{Co}^{2+}$ . Further increase in the pH of the leachate to 12 precipitated  $\text{Mn}^{2+}$ ,  $\text{Ca}^{2+}$ ,  $\text{Mg}^{2+}$  completely. At a slightly higher pH of up to 13,  $\text{Li}^+$  is recovered. It is reported that temperature is a more important factor in controlling the yield than seeding the solution [43].

According to classical nucleation, crystallization takes place in the following steps: the molecules, atoms, or ions in the solution first reach supersaturation and come together to form a cluster or nucleus. If the size of this assemblage is smaller than a critical size, the cluster will re-dissolve. But when its size is larger than the critical size, a stable nucleus is formed and subsequent growth occurs [44]. During precipitative crystallization, nucleation and growth are very important parameters to investigate. Change in solution properties such as turbidity [45], pH [46], conductivity [47], and temperature [48] could be employed as indicators towards the nucleation process. It is feasible to use systems like microfluidics to study the growth of a single crystal through flow-driven or droplet-based techniques [49]. The bulk characteristics of a well-defined architectural buildup can be effectively described using a precipitation system in the form of a chemical garden or hydrothermal vent structures [50].

A mathematical model could be formulated to explain these crystallization steps. Assuming that the solution is well mixed throughout the volume and that the collision frequency is proportional to the product of the number of particles, one could propose a kinetic model for solid-state reactions. These studies are usually aimed at obtaining rate constants that can be employed to explain the progress of a homogeneous crystallization reaction [51, 52]. Even though most models assume that the nucleation is always homogeneous, it is still feasible to take into consideration the presence of foreign bodies leading to heterogeneous nucleation in the kinetic model [53]. It plays a part in the nucleation process more than expected, especially when the reaction takes place at moderate to low supersaturations. The size, the number, and the shape of the foreign surface along with its interaction with the nucleus formed, determine the level of heterogeneity in the reaction. With this level of effect, it is very difficult to totally eliminate the presence of heterogeneity, except in cases where the reacting solution has a very high supersaturation [54–56].

This research consists of three major parts. First, the nucleation kinetics of the precipitation of lithium phosphate is investigated in a well-stirred system. Then a quasi 2-dimensional microfluidic setup is employed to describe the growth of polycrystalline lithium phosphate. Finally, a 3-dimensional lithium phosphate precipitate structure, like a chemical garden, is prepared, and its growth characteristics in a flow-driven system are analyzed and presented.

# Chapter 2

## Literature Review

### 2.1 Crystallization/Precipitation

The physical transformation (phase transition) of a solution due to its supersaturation into a solid is referred to as precipitation. When these solid particles rearrange to form a highly organized structure, the process is known as crystallization [57]. A solution is said to be supersaturated when the solute concentration is higher than the equilibrium solute concentration (solubility).

Nucleation and crystal development are two main processes in crystallization, both of which are influenced by thermodynamic and chemical factors. Nucleation is the step in crystallization where dispersed solute molecules or atoms form clusters on a microscopic scale (elevating solute concentration in a given region) that become stable under the given operating conditions [58].

Different types of nucleation can occur in a system. The most common type is spontaneous or homogeneous nucleation which is an instantaneous formation of nuclei from the reacting species without the addition of any external material [59]. Another type of nucleation is heterogeneous nucleation, which involves the triggering of nucleation due to the presence of dust particles, other impurities present in the solution, or the walls of the reactor. In this case, the nucleation is termed primary heterogeneous nucleation. On the other hand, if nucleation is caused by the presence of an added solute crystals, it is referred to as secondary heterogeneous nucleation [59].

In order to estimate the nucleation kinetics in a reactive precipitating system, induction time measurements are usually carried out. The time difference between the moment of supersaturation formation and the identification of crystals for a constant supersaturation is called the  $t_{ind}$ . The induction time, according to Mullin [60], is made up of three components as

$$t_{ind} = t_r + t_n + t_g , \quad (2.1)$$

where  $t_r$  is the time required for the system to achieve a quasi-steady-state cluster distribu-

tion,  $t_n$  is the time required for the formation of critical nuclei, and  $t_g$  is the time required for the critical nucleus to grow to a detectable crystal.

A minimum amount of energy, so-called activation energy of nucleation, is required for the ions to overcome the energy barrier and transform into a stable nucleus. It is important therefore, to note the contribution of the activation energy to the formation of a nucleus in a precipitation system because it determines how fast the precipitation should occur. In a reactive chemical system, the temperature should be sufficiently high for an appreciable number of molecules with translational energy equal to or higher than the activation energy for chemical reaction to proceed at a tolerable rate [61].

Alongside nucleation, crystal growth also takes place. Crystal growth refers to the continued size expansion of a nucleus once it reaches the critical cluster size. It is an equilibrium process in which solute molecules or atoms precipitate out of solution or decay by monomer detachment and dissolve back into the solution depending on the properties of the surface of the nuclei. It is possible to examine the growth of crystals after nucleation and their accompanying propagation mechanism using different crystallization methods. Several theories have been postulated about crystal growth pathways. One of which is the surface energy theory, which states that a growing crystal takes a shape or form which guarantees a minimum surface energy. Another is the diffusion concept, which assumes that particles are continuously deposited on a crystal face at a rate depending on the concentration gradient between the point of deposition and the bulk of the solution. The adsorption layer theory, suggested by Volmer (1939), states that crystal growth is a discontinuous process, involving adsorption of matter layer-by-layer on the crystal surface [62–64]. For effective investigation of crystal growth, a microfluidic system is mostly used [65, 66].

Nucleation or growth may predominate over the other depending on the environment, hence influencing the crystal size distribution. When nucleation occurs at a faster rate than growth, numerous crystals are formed with varying crystal sizes, and when growth dominates nucleation, usually occurring at low supersaturation, the particle size distribution becomes smaller [54–56].

Single crystals of proteins have been produced efficiently in droplet-based microfluidic devices [67–69] where the nucleation and the growth are decoupled by varying the flow rate and the reactant concentrations [70, 71]. When reactants are pumped parallel to each other from different inlets into a microchannel, one-dimensional inorganic membranes may develop [50, 72, 73], offering the ease of monitoring the tubular growth of a confined chemical garden.

## 2.2 Classical Nucleation Theory

Although crystal nucleation has significant impact on the shape of the final product and its application in medicine, glass, and ceramic technology [74], there is little known about the process itself. Most of what is known are theoretical assumptions due to the complexity of the underlying mechanisms [75]. The classical nucleation theory (CNT), stems from the research of Gibbs (1948), which is based on the condensation of a vapour to a liquid, and may be extended to crystallization from melts and solutions [76]. This is the most common theoretical model used to quantitatively study the kinetics of nucleation [77]. Classical nucleation theory makes a number of assumptions, such as treating a microscopic nucleus as a macroscopic droplet with a well-defined surface whose free energy is calculated using an equilibrium property called the interfacial tension [78]. Furthermore, its rate is approximated using equilibrium properties, even though the phenomenon occurs out of the thermodynamic equilibrium. This theory is also based on the assumption that clusters of a certain size can increase by adding monomers or disperse by spontaneously releasing a monomer into the surrounding solution. Processes, however, involving clusters that are larger than the monomers are not taken into account [79]. It assumes that a nucleus only forms when stable clusters come together to generate a large surface where growth takes place. In order to become a stable nucleus, clusters must reach a certain critical size [80, 81]. In Fig. 2.1, the sum of the surface excess free energy  $\Delta G_S$ , which is the excess free energy between the surface of the particle and the bulk of the solution, and the volume excess free energy  $\Delta G_V$ , i.e., the excess free energy between a very large particle ( $r = \infty$ ) and the solute in solution is equal to the total excess free energy  $\Delta G$ . A small solid particle of solute is assumed to be a sphere of radius  $r$ , and the solute in a solution, such that

$$\Delta G = \Delta G_S + \Delta G_V = 4\pi r^2 \gamma - \frac{4}{3}\pi r^3 \Delta g_v, \quad (2.2)$$

where  $\Delta g_v$  is the free energy change of the transformation per unit volume and  $\gamma$  is the interfacial tension between the developing crystalline surface and the supersaturated solution.  $\Delta G_S$  is a positive quantity whose value is proportional to  $r^2$ .  $\Delta G_V$  is a negative quantity proportional to  $r^3$  in a supersaturated solution. Since  $\Delta G_S$  and  $\Delta G_V$  are of opposite signs and vary differently with the radius of the nucleus,  $\Delta G$  passes through a maximum free energy  $\Delta G_{crit}$  value corresponding to the radius of a critical nucleus  $r_c$  [60].

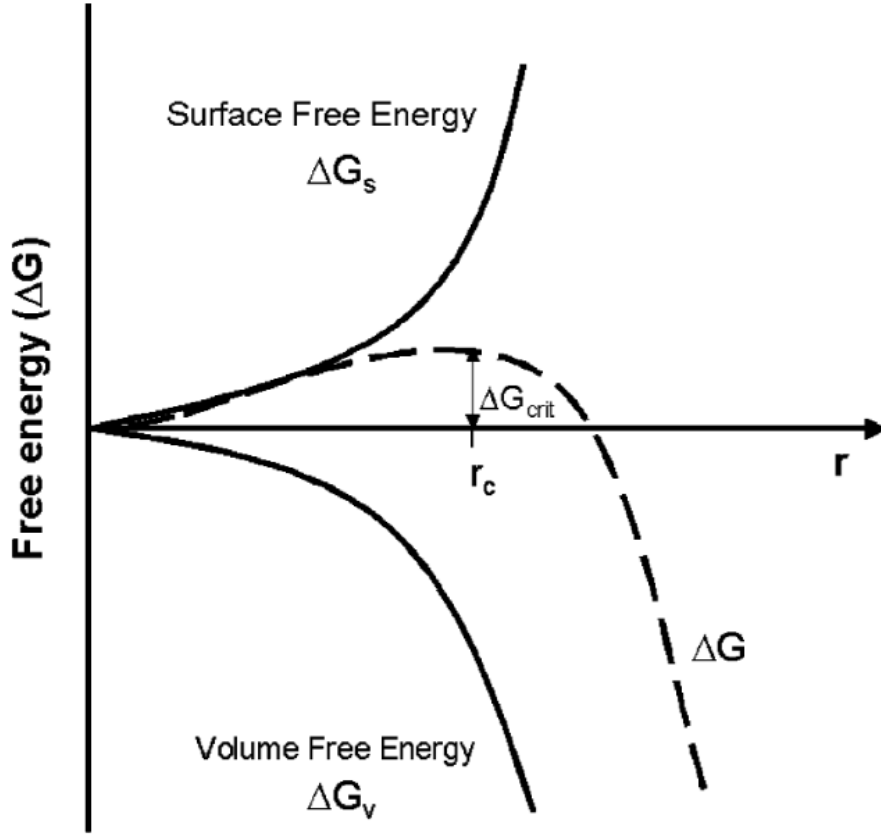


Figure 2.1: Free energy diagram for nucleation, reproduced with permission from ref. [82]

For a spherical cluster,  $\Delta G_{crit}$  is obtained by maximizing Eqn. 2.2 to give

$$\Delta G_{crit} = \frac{4\pi r_c^2 \gamma}{3}. \quad (2.3)$$

Although Fig. 2.1 demonstrates why a particle larger than the critical size is stable [82], it does not explain how much energy,  $\Delta G_{crit}$ , is required to make a stable nucleus. This can be explained in the following way: at constant temperature and pressure, the energy of a fluid system remains constant, however, this does not imply that the energy level remains constant throughout the fluid. There will be fluctuations in the energy around a constant mean value in the molecules that make up the system, and nucleation will be favored in the supersaturated regions where the energy level temporarily rises to a higher value [60]. The nucleation rate  $J$ , i.e., the number of nuclei formed per unit time per unit volume, can be expressed in the form of the Arrhenius-type equation commonly used for the rate of a thermally activated process:

$$J = A \exp\left(-\frac{\Delta G_{crit}}{k_b T}\right), \quad (2.4)$$

where  $k_b$  is the Boltzmann constant and  $T$  is the absolute temperature. From the Gibbs–

Thomson equation for non-electrolyte, the radius of the nucleus can be written as

$$r = \frac{2\gamma v}{k_b T \ln S}, \quad (2.5)$$

and its substitution into Eqn. 2.3, then into Eqn. 2.4, when  $r = r_c$ , where  $S$  is the solution supersaturation, Eqn. 2.4 becomes

$$J = A \exp \left( -\frac{16\pi\gamma^3 V^2}{3k_b^3 T^3 \ln^2 S} \right), \quad (2.6)$$

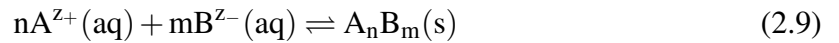
where  $V$  is the volume of the solute given by

$$V = \frac{M_w}{\rho_c N_A} \quad (2.7)$$

with  $M_w$  as the molecular weight of the crystal,  $\rho_c$  the density of the crystal, and  $N_A$  as the Avogadro constant.  $A$  is the prefactor, which is determined from kinetic considerations and is given by

$$A = \frac{f^* c_0 z}{S} \quad (2.8)$$

where  $f^*$  is the collision frequency of the ions, molecules, or clusters in the solution,  $z$  is the Zeldovich factor that accounts for the possibility of a critical cluster growing into a large crystal, and  $c_0$  is the concentration of the active nucleation site [83]. Equation 2.6 indicates that the rate of nucleation depends on three main variables: absolute temperature  $T$ , degree of supersaturation  $S$ , and interfacial tension between the particle surface and the solute in the solution ( $\gamma$ ). The supersaturation, for a general reaction



is given by

$$S = \frac{a_{A^{z+}}^n a_{B^{z-}}^m}{K_{sp}} \quad (2.10)$$

with  $K_{sp}$  being the solubility product of the solid precipitate,  $a_{A^{z+}}$  and  $a_{B^{z-}}$  are the activities of the reacting ions. Since  $t_{ind} = (J V)^{-1}$ , Eqn. 2.6 reduces to [60]

$$t_{ind} = A' \exp \left( \frac{B}{\ln^2 S} \right), \quad (2.11)$$

where  $A' = (A V)^{-1}$  and the thermodynamic parameter  $B$  is given as

$$B = \frac{16\pi v^2 \gamma^3}{3k_b^3 T^3}, \quad (2.12)$$

which can be obtained from the direct fitting of the plot of  $t_{ind}$  as a function of  $S$ .

Most reported experimental data fittings used the above definition of the classical nucleation theory for the determination of nucleation kinetic parameters, neglecting the contribution of the ions in solution and the dependence of  $A$  on the chemical potential  $\mu$  [84]. A more accurate examination of experimentally determined  $J(\mu)$  dependence must take into account the fact that  $A$  can fluctuate significantly with  $\mu$ , especially when  $A$  is modified by the means of temperature change. For example, Eqn. 2.6 shows that accounting for the  $A(\mu)$  dependence in vapours or solutions can be done with adequate accuracy, especially at high supersaturation, by using  $\ln(J/S)$  and  $\ln A$  instead of  $\ln J$  and  $\ln A$  [84].

Since the time taken for a nucleus to appear in the solution ranges from very short to extremely long on an experimental timescale, one of the achievements of CNT is explaining and quantifying this immense variation. Fairly concessional data of nucleation rates showing agreement with CNT have been reported for the nucleation process during water condensation [85, 86]. At low water content, diffusion cloud chamber experiments show a good approximation to the expected critical supersaturations for ethanol, methanol, and water nucleation, as well as for a binary mixture of o-xylene and m-xylene and for ethanol-water systems [87, 88].

A drawback associated with the CNT is that at high temperatures nucleation rates are over-predicted, while at low temperatures they are under-predicted [89]. Various attempts have been made to address these discrepancies by explicitly accounting for cluster microscopic features. The validity of such expanded models, however, is contested. One issue is the sensitivity of nucleation rate to the free energy  $G$ , such that even minor differences in the microscopic parameters can result in huge changes in the projected nucleation rate [90]. Because of this, making predictions based on fundamental principles is practically difficult. Models must instead be fitted to experimental data directly, which limits the capacity to assess their basic validity.

Nielsen (1964) described an empirical approach to the nucleation process, expressing a relationship between the induction period,  $t_{ind}$  and the initial concentration of the supersaturated solution  $c$  [91]

$$t_{ind} = kc^{1-p}, \quad (2.13)$$

where  $k$  is a constant and  $p$  is the number of molecules in a critical nucleus. Although this is an over-simplification, it is suggested that the induction time represents the time needed for the assembly of a critical nucleus. Even though this theory is also based on the assumption of cluster formation, they disagree about how supersaturation affects the size of a critical nucleus. The classical nucleation theory implies that the nucleus size is determined by supersaturation, whereas this empirical theory suggests a smaller but constant nucleus size regardless of the supersaturation [91]. With all its drawbacks stemming from the many assumptions, CNT is a fairly reasonable approximate model for fitting experimental data in

the crystallization of hard spheres [92].

Other models derived from the CNT and mostly used in numerical modelling of nucleation have been developed in the past to explain nucleation. These include a fusion of the extended-modified-liquid-drop model and the dynamic nucleation theory [93], the self-consistent classical theory [94], the diffusive interface theory [95], the perturbative density functional approximations [96], and the semi-empirical density functional approximation [97]. Gránásy and Iglói [94] presented a detailed review on the comparison of experiments and modern theories of crystal nucleation. Recently Karthika *et al.* [78] also compared classical and nonclassical nucleation theories. Other most recent reviews of nucleation theories are done by Vekilov, (2020) [98], where the deviations from classical nucleation pathways to nonclassical mechanisms are discussed. Whitehead, *et al.*, (2021) [99] carried out a critical analysis of classical nucleation theory, and its application to silver halide, semiconductors, metals, and metal oxide nanoparticles. Ramirez, *et al.*, (2021) [100] provided further evidences against the alleged failure of the classical nucleation theory below the glass transition temperature.

Classical nucleation theory has been used in different crystallization studies, for example, in barite systems, crystallization follows the homogeneous pathway and the rate of nucleation could be affected by some physical and chemical factors that are covered by the CNT. Upon addition of NaCl solution greater than 3.0 M, the induction time of barite nucleation increases due to the substitution of the sodium ion into the lattice of the barite [101]. The influence of several different solutes, such as sulfites and copolymers on the nucleation kinetics was extensively investigated [102, 103]. It is implied that at low doses, sulfite ions enhance barium sulfate crystallization, doing so by possibly promoting de-solvation of the barium ion to form a weak complex with it [102]. The presence of copolymers of maleic acid and vinyl sulphonic acid, on the other hand, is found to slow down the growth rate while increasing the nucleation rate [103, 104]. When strontium salt is added during the barite crystallization, the crystal size distribution of the final product is affected. In Sr(II)-free solution, the observed barite nucleation rates are consistent with the CNT in which barite crystals had a nonuniform size distribution and different morphologies. Nanotomography demonstrated that the addition of  $\text{Sr}^{2+}$  increases nucleation rates, which is likely due to the adsorbed  $\text{Ba}^{2+}$  and  $\text{Sr}^{2+}$  serving as precursor sites on which nucleation occurs. Strontium(II) ion, however, limits the growth concurrently, resulting in a uniform dispersion of smaller crystals [105].

In the conversion of ACC to vaterite, three stages are reported. The dehydration and ordering of ACC preceding the considerable crystallization of vaterite are considered the first step, followed by vaterite growth, then ripening [106]. The addition of sulphate ions to the system decreases the crystallization rate constant during the growth of vaterite, as compared to the pure ACC system. This decrease could be a result of the adsorption of the sulphate ion, blocking the nucleation sites on the growth of the spherulitic vaterites.

These phenomena are also observed during calcite growth in the presence of sulphate ions [107, 108]. In general, the formation of calcite follows the dehydration of ACC to vaterite, then transformation of vaterite to calcite through dissolution and reprecipitation [109]. The addition of citrate increases the lifetime of ACC. A slight change in the local atomic structure of ACC is observed from synchrotron radiation particle distribution functions analysis, which indicates that the citrate acts as a template for generating specific interatomic distances [110].

The formation of the nickel oxalate precipitate follows a two-step process proven by spectrophotometric measurements [45]. The reactant ions first form an uncharged complex of  $\text{Ni}(\text{COO})_2$ . Two of those complexes may collide to produce a nucleus that will either disintegrate or grow in size, inducing crystallization. It could be assumed that the rate of reaction is proportional to the concentration of the  $\text{Ni}(\text{COO})_2$ , hence a power law fitting of the induction time data as a function of the supersaturation of the solution is described by a  $2^{\text{nd}}$ -order kinetics. When the curve is fitted by Eqn. 2.11, it is obtained that the trend in the induction time is also perfectly described by the CNT [45].

The link between the exponents in a simple power law – obtained from the relationship between the induction time and the concentration of the reactants – and the microstructure of precipitates is established for oxalate precipitates. The complexity of the microstructures increases as the exponent as shown in Fig. 2.2 [111] for the precipitation of alkaline earth metal and some transition metal ions with oxalate ions, with the most complex microstructure for barium oxalate.

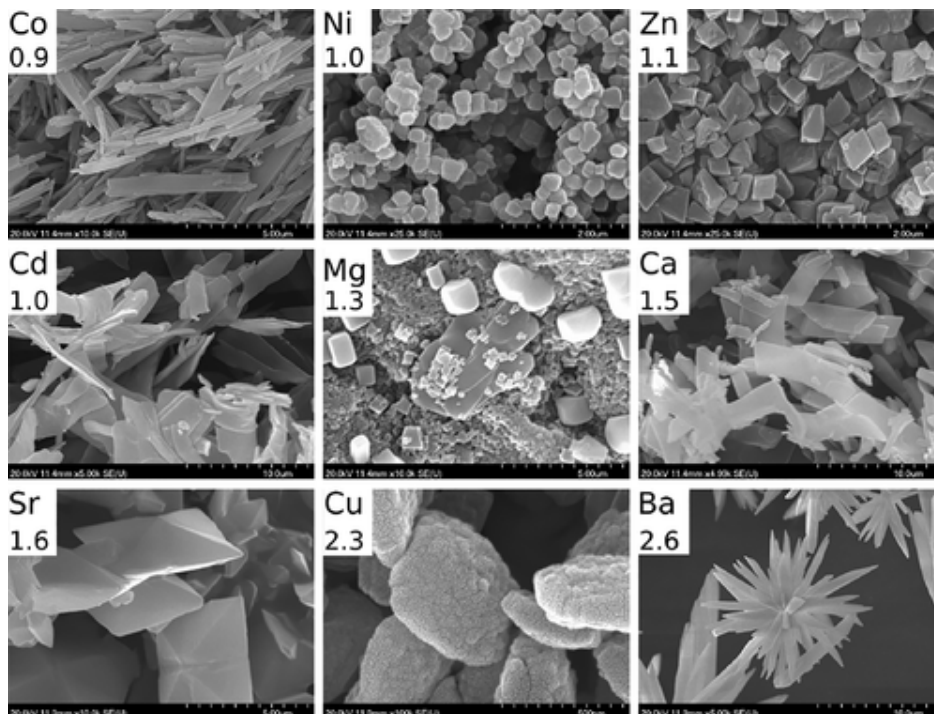


Figure 2.2: SEM micrographs of the precipitate microstructures arranged in ascending exponent order, reproduced from ref. [111]

Hydrolytic nucleation and growth of titanium (IV) oxide nanoparticles are investigated

using dynamic light scattering (DLS) and UV-visible spectrometry. The correlation between the DLS data and UV-visible spectrophotometric data is determined by chemically freezing the hydrolysis at different reaction times. The solid  $\text{TiO}_2$  together with the unreacted Ti in the supernatant solution is quantified using inductively coupled plasma - optical emission spectroscopy. The total amount of the  $\text{TiO}_2$  is independent of the period that sampling was made, indicating that only the size of the particle increases. This made it possible to compare the results obtained from DLS and UV-visible spectrometry easily. The trend found in both methods suggests that the increase in turbidity is a sole function of particle size and not the overall particle numbers [112]. A kinetic model considering the rapid hydrolysis of the Ti precursor to a primary particle or monomer of  $\text{TiO}_2$ , followed by a slow dimerization and then particle growth, is developed to explain the formation of  $\text{TiO}_2$  nanoparticle [112, 113].

## **2.3 Mixing conditions for precipitation**

Over the years, different methods have been reported for efficient precipitation and crystallization of inorganic and organic salts. These methods range from large-scale reactors to microreactors. The method used to study the precipitation process depends on the type of ion and supersaturation range of the reactant mixture. Other conditions such as the method of mixing or intensity of mixing are considered vital [114, 115]. We, therefore, reviewed some experimental studies involving precipitation in continuously or well-stirred systems and flow-driven systems.

### **2.3.1 Precipitation in a well-stirred system**

In this arrangement, stirring the reacting solution distributes supersaturation throughout the reactor. In order to achieve proper solution mixing, a mechanical stirring device or ultrasound energy is mostly employed. Several studies have been reported, where agitation plays a vital role in controlling nucleation, data reproducibility, and improving particle size distribution [116, 117].

The precipitation of lithium carbonate is studied following a  $\text{CO}_2$  stripping from a slightly acidic  $\text{LiHCO}_3$  solution through continuous stirring to achieve supersaturation [118]. The reaction kinetics for this process is described by a second-order rate expression, and the apparent activation energy indicates that the growth of  $\text{Li}_2\text{CO}_3$  under constant stirring is a diffusion-controlled process. By injecting a  $\text{Na}_2\text{CO}_3$  solution into a well-stirred solution of  $\text{Li}_2\text{SO}_4$ , the formation of lithium carbonate was investigated as well. Induction times characterized by the appearance of a solid phase are determined using a focused beam reflectance measurement. Particle size decreases with increasing stirring speed [119]. Similarly, ultrasound has the capacity to increase cavitation leading to a higher recovery of  $\text{Li}_2\text{CO}_3$  with lower particle size distribution compared to a stirred system, paving a way for efficient recov-

ery [120]. Calorimetric measurement is also used to determine the kinetic parameters for the crystallization of  $\text{Li}_2\text{CO}_3$  from  $\text{Li}_2\text{SO}_4$  and  $\text{Na}_2\text{CO}_3$  solutions, by measuring the temperature changes between the initial condition and the final state of the reaction when the  $\text{Li}_2\text{CO}_3$  is formed under constant stirring. The growth of the crystal between 333–353 K is dominated by the chemical reaction [121], while diffusion and transport processes are insignificant.

The contribution of mixing to the enantiomorph selectivity of sodium chlorate crystals is studied and reported by Callahan *et al.*, (2014). In the absence of stirring, all the product crystals have the same enantiomorphism as the seed crystal. This implies that in quiescent situations where the seed boundary layer has not been disrupted, the solute molecules would adhere to the seed in the bulk solution, resulting in seed-similar nucleation of products. When the crystallization is carried out in the presence of continued agitation prior to, during, and post-seeding, a mixture of 94% crystals similar to the seed crystal and the opposite enantiomorph are found in the solution [117].

In a glycine-water system, the effect of stirring is monitored in two reactors of different dimensions (50 mL and 500 mL), while maintaining the same stirrer tip speed to obtain equal bulk fluid velocities [122]. Larger reactors produce crystals of bigger sizes as compared to those obtained from smaller reactors, because the bigger reactors have lower mixing intensity leading to faster nucleation and growth [123, 124].

Mixing quality affects nucleation rate during crystallization [125, 126]. In a continuous reactant injection and product withdrawal system consisting of a marine-type impeller stirring setup – where the stirrer is made of blades and suspended in the reactor without contact with the vessel –  $\text{Ca}(\text{COO})_2$  is precipitated. This method allows for an effective monitoring of the process parameters online [125, 127]. Similarly, using a double-feed semi-batch stirred tank reactor, which allows partial filling of reactants with the flexibility of adding more as time progresses,  $\text{BaSO}_4$  crystals are precipitated from  $\text{Na}_2\text{SO}_4$  and  $\text{BaCl}_2$  solutions. The even distribution of supersaturation throughout the solution by continuous stirring slows down the fast nucleation and influences particle size distribution [126, 128, 129]. The formation of different polymorphs of  $\text{CaCO}_3$  is mostly affected by the mixing procedure. Needle-shaped aragonites are formed when reactants are not agitated or when very low ultrasound energy is applied. Under constant agitation and long maturing time, calcites are formed [130].

The influence of ultrasound energy enhances nucleation in lysozyme crystallization as the induction time is shortened when the solution is ultrasonicated. Furthermore, it leads to a more uniform crystal size distribution as compared to the control system in the absence of any agitation. This effect is more pronounced when the solutions are of very low supersaturation. Prolonged exposure to ultrasound resulted in the formation of smaller sized crystals and could lead to absorption of too much energy, causing denaturation of the lysozyme [131, 132].

The advantages offered by a well-stirred system include the high reproducibility of ki-

netic data and the homogeneous distribution of ions within the reacting solution. The ease of temperature manipulation offered by this system is an added advantage.

### 2.3.2 Precipitation induced by flow

The possibility of using flow to induce reactant mixing during precipitation has been popularised and effectively applied for studying crystal nucleation and growth. It is discussed in many circumstances that flow-driven systems create a concentration or density gradients with the capacity to selectively fine-tune and produce crystals of a given morphology [133–136]. With the aid of a flow-driven system, high purity calcite crystals were produced in a Hele-Shaw reactor, while in a constantly agitated system, in the absence of a concentration or density gradient, a mixture of polymorphs forms [133]. This method is not restricted to polymorph selection, it can be extended to macroscopic pattern formation in a 2D flow system [134]. Different patterns of calcium carbonate precipitate form in a Hele-Shaw reactor, where the amount of the precipitate is reduced as both the concentration and the injection rate of the solution is increased. This is caused by the reduction in permeability due to the rise in the viscosity of the injected solution with the concentration.

Calcium silicate is one of the major constituents of cement [137] which is typically produced under constant stirring. However, interesting spatiotemporal patterns form when the precipitation reaction between calcium chloride and sodium silicate is carried out by injecting a solution of calcium ions into a flat Hele-Shaw reactor containing a silicate solution at 20 mm depth. At first, an open tube forms, making up a four-arm spiral to display a floral-like structure. Due to the gradual lowering of the concentration of the reactants further away from the inlet, the spiral growth transitions to radial growth. Another important change in the symmetry is the breaking of the radial growth to fingers [138].

This method is also employed to analyze the formation of  $\alpha$ -Co(OH)<sub>2</sub> by injecting a solution of CoCl<sub>2</sub> containing water-in-oil microemulsion into NaOH solution in a Hele-Shaw reactor. The evolving patterns consist of concentric circles separated by regular deformations (see Fig. 2.3). The dark-field images of the patterns show boundaries deviating from smooth circles to jagged or sinusoidal patterns as the hydroxide ion concentration is increased [135]. The total area of the circle from the dark-field images increases linearly as the injection rate and inversely as the hydroxide ion concentration. This is due to either the breakdown of the microemulsion or due to patterns strongly affected by the precipitation of  $\alpha$ -Co(OH)<sub>2</sub>.

In a similar work by Balog *et al.* [139], several precipitate patterns of metallic oxalates are investigated, ranging from Mg to Zn. A shorter reaction timescale for the formation of alkaline earth oxalates is observed. The precipitate patterns obtained for alkaline earth metal oxalates exhibit symmetry deformation at higher injection rates (see Fig. 2.4a) due to the formation of hydrodynamic instabilities as aggregated precipitate particles are washed away and accumulate at the bottom. The level of the deformation depends on the molecular weight

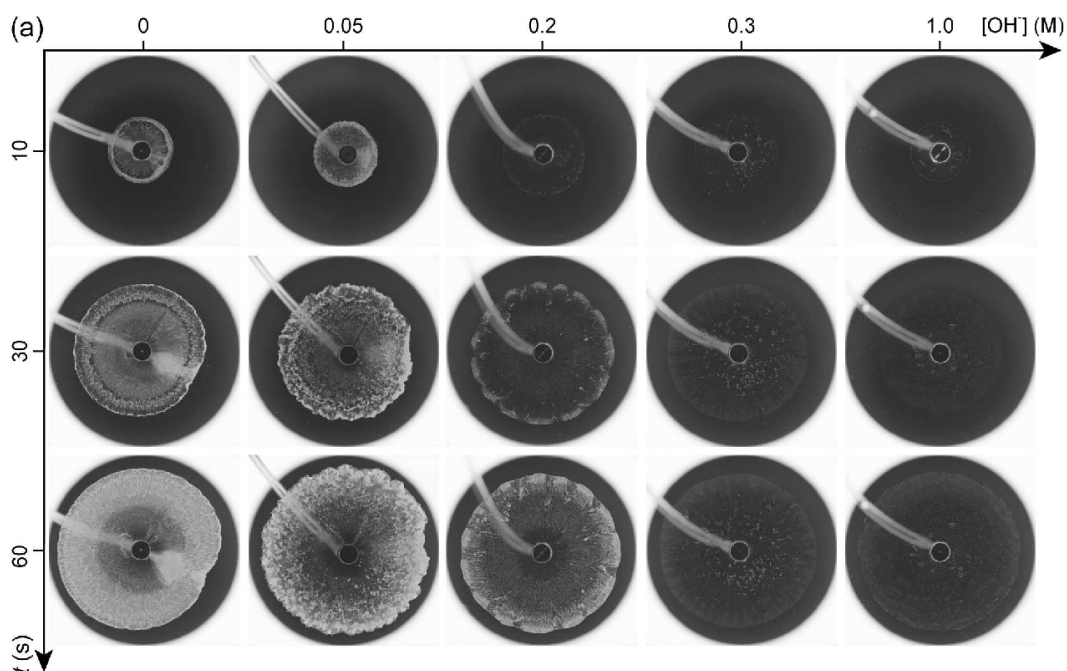


Figure 2.3: Temporal sequence of experimental patterns obtained for different NaOH concentrations, reproduced from ref. [135]

of the metal ion. For the transition metal oxalates, however, circular patterns are maintained because the injected and the static solutions are not affected by the particle sedimentation as shown in Fig. 2.4b.

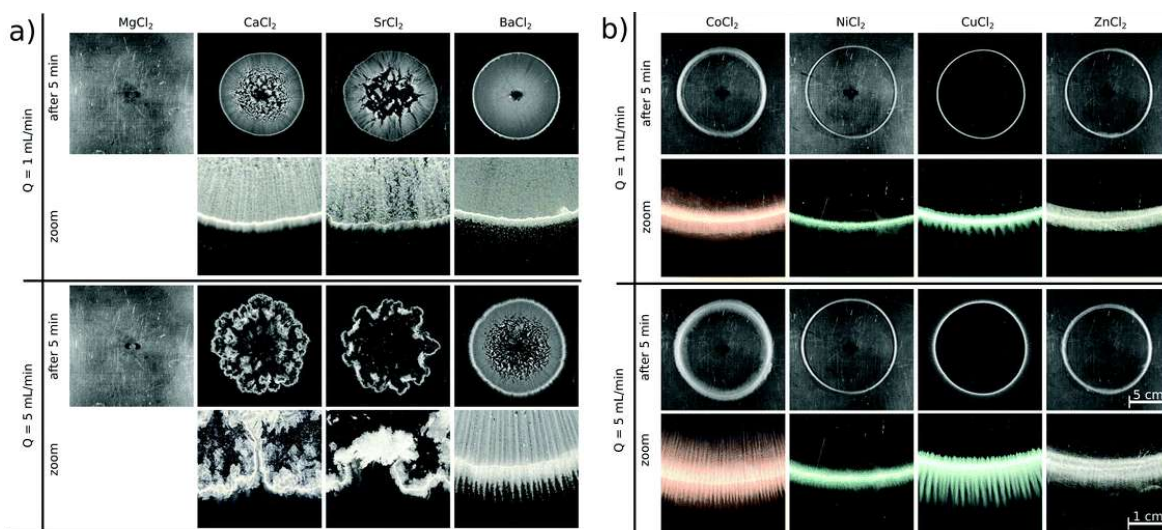


Figure 2.4: Different pattern formation corresponding to elements family: complex (a), simple (b), reproduced from ref. [139]

Flow-driven systems offer opportunities for the spatial separation of a mixture of metallic oxalates such as copper and cobalt oxalates through precipitation by serving as a form of a selective separation technique. For example, when a solution containing a mixture

of  $\text{Co}^{2+}$  and  $\text{Cu}^{2+}$  is injected into a solution of  $(\text{COO})_2^{2-}$  in a flat Hele-Shaw reactor, the density difference between the solutions yields a gravity current, leading to the formation of a radially symmetrical precipitate pattern. Three precipitate zones are observed and characterized. Analysis of the samples collected from each of the precipitation zones shows that the tip of the radial pattern contains mostly  $\text{Co}(\text{COO})_2$ , followed by a region of transition where a mixture of both the  $\text{Co}(\text{COO})_2$  and  $\text{Cu}(\text{COO})_2$  is present. The inner circle consists of mostly  $\text{Cu}(\text{COO})_2$  as identified by scanning electron microscopy and X-ray diffraction [140, 141]. Similarly, polymorphs of 5-methyl-2-[(2-nitrophenyl)amino]-3-thiophenecarbonitrile (ROY), are separated using a flow-driven system by injecting acetone solution of ROY at different concentrations into a Hele-Shaw reactor containing water. Red prism is selectively favored near the injection point, while yellow needles formed at the tail end [136].

Flow-driven system could also be employed in the investigation of the formation of chemical garden precipitate structures. It provides an easy way of studying and characterizing the physicochemical properties of a chemical garden. Since the chemical gardens generated from solid pellets do not yield reliable data for the study of its kinetics, the flow system offers more reliable and reproducible data. Numerous studies have been done on different flow-driven chemical garden formations, for example, the growth of tubular structures at the interface between two solutions by chemical precipitation [142–144] have been studied and reported, and many others in progress.

## 2.4 2-dimensional precipitation in microfluidic system

Microfluidic systems offer a means to study the formation of a quasi 2-dimensional precipitate or crystal. More attention is given to this method because of its high-throughput and microliter reactant consumption. It also has the capacity to provide thermodynamic and kinetic data for improving industrial processes by offering more explanation on nucleation and growth mechanism [65]. The small volume used in a microfluidic system is of particular importance for nucleation. The mean nucleation period ( $\propto 1/V$ ) may be longer than the crystal growth per unit time, resulting in only one nucleation event being statistically observed: this mononuclear process is critical for assessing nucleation kinetics and exploring polymorphism [145]. The co-flow design of a microfluidic system also allows the effective screening of crystal polymorphs [146], essential for creating a desired crystalline material. The small volume of solution used in microfluidic devices is harnessed to study the different polymorphs of  $\text{KNO}_3$  crystal by ensuring the formation of a mononuclear crystal [147]. Raman micro-spectroscopy is carried out on the droplets containing the crystal revealing vibrational signatures corresponding to several polymorphs of  $\text{KNO}_3$ .

A microfluidic device is utilized for the rapid probing of solubility diagrams of a solution of adipic acid. Using hundreds of nanoliter-volume droplets, solutions are collected with a

slight difference in their solute content and the application of a temperature gradient allows for the direct evaluation of a concentration-temperature phase diagram [148]. This method is very cheap and efficient as several solubility curves can be accessed in less than an hour on a large temperature range using only a few hundred microliter of solution. In a similar vein, a microfluidic tool is used to generate monodispersed microreactors (as shown in Fig. 2.5) by injecting oil (silicone) through inlet (1), and the aqueous solution of  $\text{KNO}_3$  through inlet (2). When the stream of the aqueous phase meets the stream of the oil at the intersection of the inlets, the aqueous phase forces the formation of a meniscus, and the continuous injection of the oil produces a droplet containing the reactant solution. The temperature ( $T_1$ ) is maintained as the oil droplets containing the aqueous phase flow along the channel. A large temperature quench is applied to the droplets as they arrive at the position with  $T_2$ , and the nucleation kinetics is investigated by determining the probability of crystal presence in the droplet with time [49]. The nucleation parameters obtained from classical nucleation theory for this reaction suggest a heterogeneous nucleation mechanism with more than one nucleation site due to the relatively large droplet size.

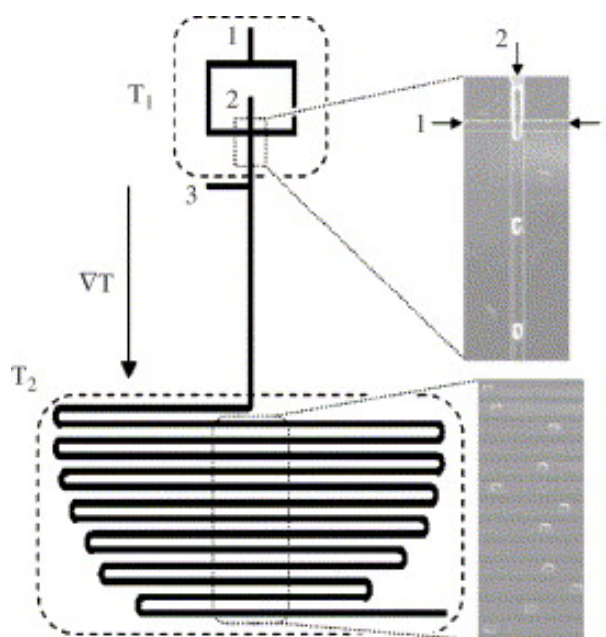


Figure 2.5: A schematic diagram of a microfluidic reactor for investigating nucleation kinetics. Oil is injected from the inlets 1, and the aqueous solution is injected from inlet 2. Oil can also be injected via inlet 3 to enhance the flow of the droplet. Reproduced with permission from ref. [49]

Controlled evaporative crystallization can be monitored, and parameters such as nucleation rate and crystal growth rate can easily be obtained for protein crystals in a microfluidic system [149]. Since XRD measurement is an important technique in identifying the crystals produced, and harvesting the crystals from such a small volume is somewhat tedious, it is possible to carry out *in situ* measurements of X-ray diffraction on-chip. The effect of the

material of the chip, the diffraction background due to the oil phase, and radiation damages must all be accounted for during the investigation [150].

In order to understand pathological microcalcification, a microchannel with similar dimensions to the collecting duct in human kidneys was adapted as a biomimetic model for calcium oxalate formation [151]. The confinement offered by the microfluidic system slows down the conversion of the unstable amorphous calcium carbonate into the crystalline form as opposed to the well-stirred reaction where the stable crystalline form appears within seconds to minutes of mixing [152–154].

The small solution volume used in microfluidics increases the surface/volume ratio, because of that, the surface of the material affects the nucleation and results in heterogeneous nucleation. Heterogeneous nucleation is rarely considered in microfluidic systems even though it is almost impossible for the nucleation to take place without the surface of the channel influencing it [155]. In order to study this surface effect, microfluidic devices with patterned silicon wafers were created using microfabrication techniques. The patterning of distinct doping sites (*p*-Si and *n*-Si) provides varied surface charge conditions on the material, which operate as a spatial nucleation site. The effects of the electrostatic repulsive force between the doped silicon surface and charged protein molecules reduced the crystallization around the selected nucleation site [155].

The measured induction periods for crystallization within a microfluidic system are stochastic due to its small volume, but deterministic models utilized by some researchers [149] to estimate nucleation kinetics for these systems fail to reflect this randomness. Stochastic models for nucleation at small length scales proposed for the scenario of constant supersaturation caused by changes in temperature [81] do not apply to evaporation-based microfluidic crystallization when the supersaturation varies throughout the experiment. An advantage of using evaporation-based microfluidic crystallization is that each experiment often creates a crystal and hence yields induction time data, even if the nucleation kinetics are unknown [149].

Hydrothermal vents are modeled in a confined 2D microfluidic reactor to explain ion transport across protocell membranes in Hadean hydrothermal vents [156]. By injecting the sodium hydroxide and manganese chloride solutions simultaneously into separate inlets of a Y-shaped microchannel, a precipitate tube forms. The diameter of this precipitate structure is measured as it extends toward the direction of the  $\text{Mn}^{2+}$  solution while static in the vicinity of the sodium hydroxide. The width of the precipitate structure scales to the square root of time, characteristic of a diffusive transport mechanism. The dependence of the growth rate on the concentration of the sodium hydroxide is linear, while on the  $\text{Mn}^{2+}$  is quadratic. The accelerated transport of the metal ion across the thin gel membrane on the precipitate surface causes such a difference in the ionic transport dynamics [156].

The merits of using a microfluidic system include the high throughput [149], ease of fabrication, time-saving, low material consumption [145], relatively cheap and easy to use

and handle. The major demerit is the difficulty in obtaining purely homogeneous nucleation due to the small volume of the reactants used [149, 155].

## 2.5 3-dimensional precipitation

In crystallization studies, the formation of a 3D precipitate structure, yielding chemical gardens and hydrothermal vents, is also of great importance as it provides an explanation for the formation of many natural structures. The work resulting in what we now call the chemical garden is originated in 1646 when Johann Glauber discovered the formation of inanimate plant-like forms upon placing transition metal salt crystals in water glass [157]. From then on, numerous research has been conducted to provide an explanation to its formation (for a review see Barge *et al.*, [157]) and possibly to explain the origin of life here, on Earth [158, 159]. One of these attempts is made by mimicking the conditions of a soda-type ocean found on Enceladus (Saturn's moon) in the laboratory [160]. This chemical garden phenomenon has been discovered to occur in nature as hydrothermal vents or chimneys [161–165] and rusts on metals [166, 167]. Researchers over the ages have been fascinated with these chemical structures; this allure has led to the studies into its formation kinetics, mechanism and even the physics of the resulting structures [168]. Scientists are now focusing on the growth behavior, patterns formation [169, 170], and oscillations [171] occurring for this process out of equilibrium.

The fascination with chemical gardens did not only stop within the Earth's ground gravity. Buoyancy-aided growth occurs for the chemical gardens grown under the influence of the gravitational field on earth, leading to the formation of upward growing structures. In microgravity, buoyancy is eliminated resulting in the development of randomly oriented chemical garden structures through the action of forced convection and osmosis [172].

The preparation of a macroscopic self-assembled chemical structure stems from the appearance of a reasonable chemical gradient, which continuously induces dissolution, diffusion, and other transport processes, besides precipitation as described in Fig. 2.6. First of all, dissolution takes place around the metal salt placed in an alkaline solution to form a semipermeable membrane enclosing an acidic solution. The high osmotic pressure in the acidic solution enables more water to flow through the semipermeable membrane and cause the rupture of the membrane, releasing the osmotic pressure. As the process continued repeatedly, precipitation takes place to build a structure rising towards the more alkaline zone.

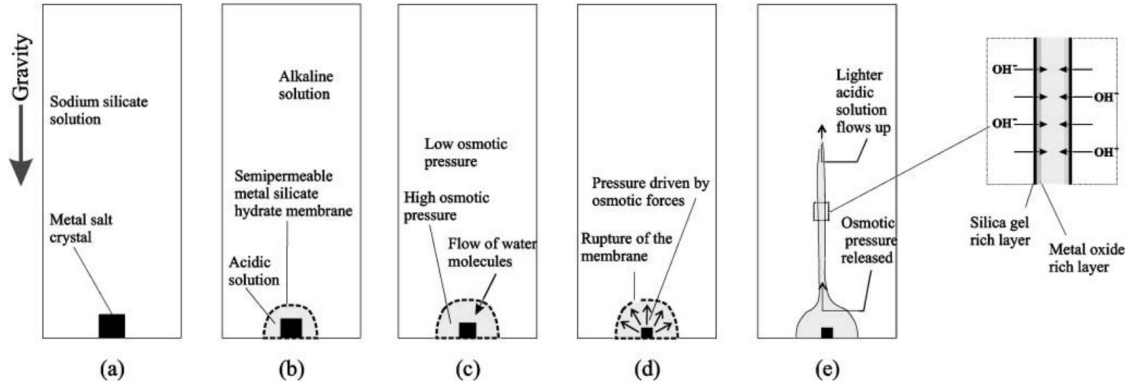


Figure 2.6: Steps involved in the formation of classical chemical garden structure, reproduced from ref. [173]

In an investigation of the dynamics of open tubular precipitate structures, it is highlighted that when multiple aluminium silicate chemical gardens grow from the same chemical source, they compete for the resources. Short and wider tubes tend to consume more of the resources than slender and long tubes, hence halting the propagation of the latter. A model is also developed to explain how single tubes grow, and how multiple tubes interact with each other. The model is based on the relationship between the volume of the tube, the volume of the metal salt solution, the exterior radius of the tube, and the injection rate [142] as

$$\pi R_t^2 \frac{dz}{dt} = \alpha q_v \quad (2.14)$$

where  $R_t$  is the tube radius,  $dz/dt$  is the linear growth rate of the tube,  $\alpha$  is a dimensionless constant, and  $q_v$  is the injection rate. For multiple tubes, additional parameters, such as the total flow coming out of the source, the pressure difference across the membranes at the base of the tubes, and the redistribution of fluid flow between the tubes as they grow [173], are considered by

$$q_{total} = \sum_i q_i(t) \quad (2.15)$$

where  $q_{total}$  is the total flow rate coming out of the source, and  $q_i$  is the flow rate through the  $i$ th tube as a function of time to allow for the redistribution of flow between the tubes as they grow. This explains why obtaining reproducible kinetic information from a pellet in silicate solution is very difficult as the number of tubes cannot be predicted and controlled [174].

The growth of a chemical garden structure by precipitation in the interface between two solutions is templated by a jet due to the solute gradients between the interfaces. The injection of aqueous ammonia into a solution of ferrous sulphate leads to the evolution of a jet on which precipitates of iron hydroxide with varying oxidation states form along the jet. Analysis of the tube evolution showed a simple scaling parameter, with lengths and time evolving linearly with the mean velocity of the jet. Following this model system, the growth of the

structure can be simulated using advection-dominated flow [144]. Self-organization to produce tubular structures in iron-ammonium-sulphate solution has been reported [142]. First, the oxidation of iron takes place, followed by precipitation on the surface of a bubble that hangs at the edge of the tube. The tube then separates from the bubble, leaving behind a ring of material. The chemical and redox gradients formed between the two solutions resulted in a radial compositional layering within the tube wall.

Hollow copper silicate chemical gardens evolve through reactive precipitation, when copper sulphate solution is injected into a solution of sodium silicate [143]. A single gas bubble templates the growth of the chemical tube (see Fig. 2.7), resulting in an elongated structure with constant diameter. Measurement of the height of the tube as a function of time revealed that the bubble size determines the tube diameter. At higher silicate concentration, tubes are found to shrink to twisted ribbons. Competing forces dictate the critical tube diameter and the point at which the tube collapses.

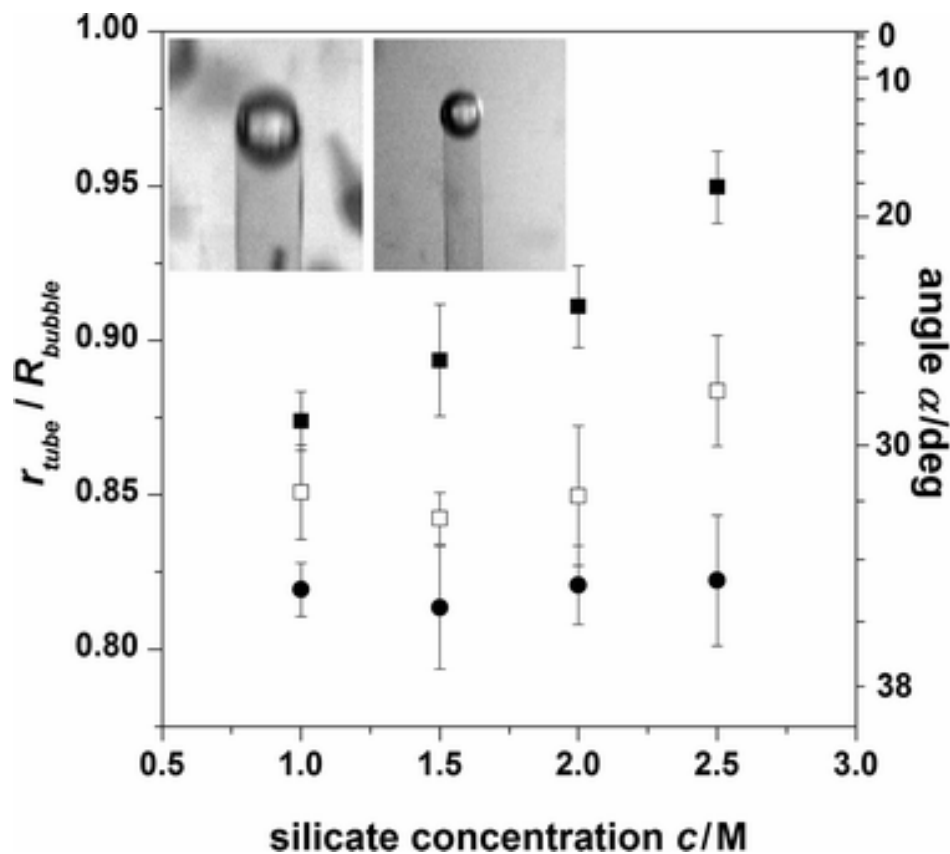


Figure 2.7: Bubble templated precipitate tube radii at different injection rates (■ 10 mL/hr, □ 5 mL/hr, ● 3 mL/hr), reproduced from ref. [143]

It was demonstrated that chemical gardens could be studied in a confined geometry [156, 175], which lowers the influence of buoyancy and reduces the spatial degree of freedom. When a solution of cobalt chloride is injected between two plates (from the central position) containing silicate solution, precipitation takes place upon the contact of the two solutions

giving rise to different quasi 3D patterns depending on the concentration of the individual reactants. Structural patterns develop from simple lobes at low reactants concentration, hairs, spirals, and worms at slightly high concentrations, to complex flowers and filaments at higher reactants concentration [170] as shown in Fig. 2.8.

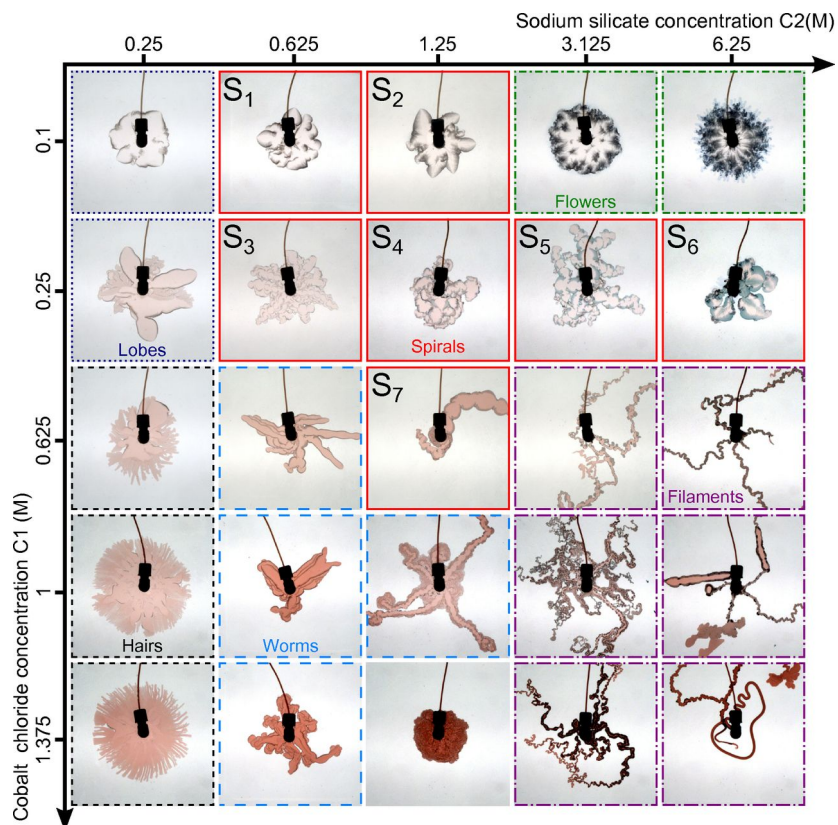


Figure 2.8: Classification of confined chemical gardens in a parameter space, reproduced from ref. [170]

Because chemical garden tubes have considerable electrochemical potential difference across them, this property could be harnessed for electric current generation. A sufficient amount of energy can be obtained when a solution containing sodium sulfide, sodium hydroxide, and methanol is injected into an acidic solution of a mixture of iron (II) and (III) chloride and sodium nitrate, then linking several of these cells in series. The electric current generated from this setup is sufficient to light an LED [176]. Chemical garden structures can also serve as flow-through reactors [177]. By forging a chemical garden structure from a catalytic material, it could offer a surface for the reactants to adsorb and be transformed in the process. This method might not be easy to handle due to the lack of rigidity of most of the tubes retrieved, but its application could open a vast universe in catalysis [178]. The chemical garden phenomenon also provides an opportunity for the fabrication of gradient composites [179] for artificial intervertebral disc [180], ablation heat shield, damping materials, and other engineering applications [181].

# Chapter 3

## Aims

Lithium salts especially phosphates and carbonates, have important applications ranging from biomedicine and catalysis, to battery technology, to mention but a few. Due to the high demand for clean energy and environmental concerns, lithium ion is been extensively used. This exhaustive usage increases the demand placed on the mining of lithium-containing minerals, causing more damage to the environment. It is possible to recycle and reuse spent lithium ion batteries hence curbing the effect of environmental pollution due to used battery disposal. The end product of lithium ion recycling is lithium phosphate, which can be reused directly as raw materials for battery production. The low solubility of lithium phosphate as compared to lithium carbonate or hydroxides makes it a better candidate for high precipitate yield. The quality of the recycled material depends on the nucleation and crystallization of the solution, leading to our study of crystallization for this lithium ion. Nucleation is a very complex and important step that shapes the morphology of the crystals formed at the end. Our aim is to study the nucleation kinetics and the dynamics of crystal growth in the lithium phosphate precipitation system. This investigation will provide data for effective modeling of the kinetic process. The specific objectives are as follows:

1. *To study the nucleation kinetics of lithium phosphate crystallization in a well-stirred system.*

Precipitation is preceded by nucleation, which determines how fast the precipitation process will take place, the quality of the final product, and the distribution of the particle size. We shall use a UV-visible spectrophotometer to measure the change in turbidity as a function of the time of a well-stirred solution of  $\text{Li}^+$  and  $\text{PO}_4^{3-}$  and then determine the kinetic parameter from the data obtained.

2. *To examine the growth characteristics of lithium phosphate polycrystals formed in a microfluidic system.*

It is possible to form single well-spaced crystals or polycrystals in a microfluidic system under very specific conditions, exploiting the small reactant volume and the con-

centration gradient generated by flow. The growth of lithium phosphate crystals shall be investigated by co-flowing the reactants into a microchannel by the use of a fully automated microfluidic system.

3. *To characterize the formation and growth of lithium phosphate chemical garden structure.*

Various methods of precipitation are available, one of which is the formation of chemical gardens or hydrothermal vents. The formation of lithium phosphate precipitate structure resembling chemical gardens shall be carried out by injecting a solution of the phosphate ions into a solution of lithium ions and then characterizing the precipitate structure that evolves.

# Chapter 4

## Materials and Methods

### 4.1 Materials

All the chemicals are of analytical grade and utilized as obtained. The following reagents were used: anhydrous LiCl (99%, Alfa Aesar), and hydrated  $\text{Na}_3\text{PO}_4 \cdot 12\text{H}_2\text{O}$  (Sigma-Aldrich). Reactant solutions were prepared in de-ionized water and filtered through a 25-mm syringe filter cap (cellulose acetate membrane with 0.2  $\mu\text{m}$  pore size, (VWR)). Cleaning of cuvette and microchannel was done with HCl 37% (AnalaR VWR).

### 4.2 Methods

#### 4.2.1 Well-stirred system

We prepared stock solutions of 1.0 M lithium chloride and 0.3 M sodium phosphate for the study of the  $\text{Li}_3\text{PO}_4$  precipitation. The process was monitored by measuring turbidity at 340 nm with a UV-visible spectrophotometer (UV-3100PC) equipped with an in-built magnetic stirrer and a thermostated cuvette holder (VWR A-100) (Fig. 4.1). The background turbidity is set with 2 mL LiCl solution in a standard commercially available quartz cuvette with 1 cm  $\times$  1 cm  $\times$  4 cm dimension, after which 1 mL solution was withdrawn. The reaction was started by pipetting 1 mL  $\text{Na}_3\text{PO}_4$  solution into the cuvette and stirring it. The turbidity measurement was repeated at least four times at room temperature for each set of concentration ranging from 0.18 M to 0.60 M for the LiCl and 0.060 M to 0.20 M for the  $\text{Na}_3\text{PO}_4$  solutions at a stoichiometric ratio of reactant concentrations, i.e.,  $R = [\text{Li}^+]_{\text{T}}/[\text{PO}_4^{3-}]_{\text{T}} = 3$ .

Thermal effects were studied with  $R = 3$  and  $[\text{Na}_3\text{PO}_4] = 0.030$  M at temperatures ranging between 25 and 50  $^{\circ}\text{C}$  with 0.01  $^{\circ}\text{C}$  precision.

After each experiment, the cuvette was removed and placed in 1 M HCl for a 5-min-long sonication (Elmasonic S 60 H) to dissolve any precipitate from the cuvette wall and crevices prior to washing with deionized water.



Figure 4.1: Experimental setup for the measurement of turbidity of a well-stirred solution

## 4.2.2 Flow-driven temporal evolution in microfluidics

The pressure generator (FLPG plus, Fluigent) we employed for this experiment produces high-quality dry air up to a maximum pressure of 2.3 bar. The generator was coupled to a flow controller (Flow EZ<sup>TM</sup>) in a dual lineup series enabling the control of the pressure to minimize the fluctuation in the flow. A flow sensor (Fluigent) was connected to each of the controller units to allow flow rate programming and increased reproducibility (see pressure and flow rate data in Appendix I).

Two separate reservoirs (Fluwell 1C-50) – one for lithium chloride and one for sodium phosphate – were used with PTFE tubings (ID = 0.5 mm) linked to the pressure controller as shown in Fig. 4.2. The tubings passing through the flow sensors were also connected to an H-shaped and irreversibly sealed channel (Microfluidic Chipshop) serving as a microreactor made from poly(methyl methacrylate) with channel dimensions of  $w = 300 \mu\text{m}$  middle width,  $150 \mu\text{m}$  inlet/outlet width,  $75 \mu\text{m}$  depth, and 13.5 mm in length. The microreactor was placed on an inverted research microscope (Nikon Eclipse Ts2R) coupled with a digital camera (Nikon LV-TV) to monitor the progressive growth of the particles in the microchannel, and images were saved at a set time interval to a computer system.

Equal volumes from analytical grade chemicals of LiCl and  $\text{Na}_3\text{PO}_4$  with  $[\text{Na}_3\text{PO}_4] = 0.1 \text{ M}$

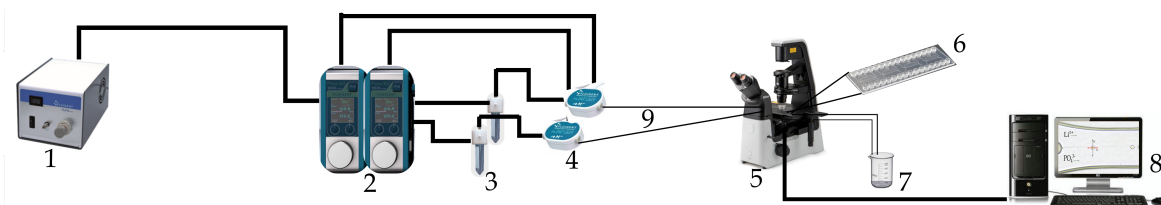


Figure 4.2: Fully automated microfluidic setup (not to scale): 1. Pressure generator, 2. Pressure controller - dual lineup series, 3. Reservoirs, 4. Flow sensors, 5. Microscope with camera, 6. Microreactor, 7. Drain reservoir, 8. Computer/readout, and 9. PTFE tube connectors

and  $R = 3$  corresponding to the stoichiometric ratio, 6 and 10 to non-stoichiometric compositions with LiCl in excess were prepared in deionized water, filtered through a 25-mm syringe filter cap (cellulose acetate membrane with  $0.2 \mu\text{m}$  pore size), and poured into the reservoirs. The flow rate was increased from  $0.1 \mu\text{L}/\text{min}/\text{channel}$  up to  $2.5 \mu\text{L}/\text{min}/\text{channel}$  for each separate experiment yielding a total the injection or flow rate  $q_v$  in the range of  $0.2 \mu\text{L}/\text{min} \leq q_v \leq 5 \mu\text{L}/\text{min}$ . The experiments were run for a maximum of 45 min to avoid clogging the reactor. The precipitated product was collected through the two outlets and kept for analysis. After stopping the flow, the entire system underwent a cleaning procedure: first, by pumping filtered deionized water into the channel at higher pressure, the precipitate formed in the microreactor was collected. Then 1.0 M hydrochloric acid was injected to dissolve any precipitate remaining in the microreactor, followed by purging the channels with deionized water again and blowing with dry air for about 2–4 minutes to dry the channels. The entire procedure was repeated 4–5 times for each chemical composition and injection rate.

### 4.2.3 Flow-driven 3D precipitation system

We prepared a solution of 6 M LiCl and placed 6 mL into a cuvette of  $1 \text{ cm} \times 1 \text{ cm} \times 30 \text{ cm}$  dimension. Using a syringe pump (kd Scientific), 0.6 M  $\text{Na}_3\text{PO}_4$  solution was pumped into the LiCl solution through a 0.4 mm internal diameter needle (for diagrammatic illustration of the experimental setup see Fig. 4.3). The pump rate was set in the range of  $10\text{--}50 \mu\text{L}/\text{min}$  and monitored with a digital camera, saving images every 5 s. Each of the experiments was repeated about 6–10 times.

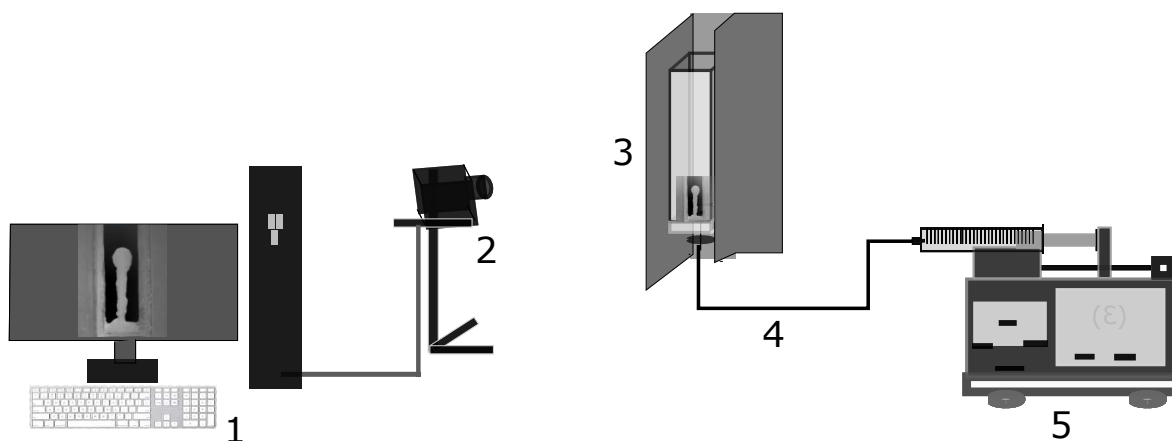


Figure 4.3: Experimental setup (not to scale): 1. processing unit, 2. digital camera, 3. reactor of dimensions  $1 \times 1 \times 10 \text{ cm}^3$  and support jacket with dark background, 4. connector tube, and 5. injection pump.

# Chapter 5

## Analytical Methods

### 5.1 Determination of induction time

When the turbidity of the solution is almost zero, it indicates that there are no solid particles present in the solution. The induction time is determined using a linear fitting of the portion of the profile where turbidity is almost zero, and then fitting it with a straight line using Mathematica. When the turbidity deviates significantly from linearity by up to 3 times the standard deviation of the background noise (Fig. 5.1), that point of deviation is recorded as the induction time (see Appendix II for the program).

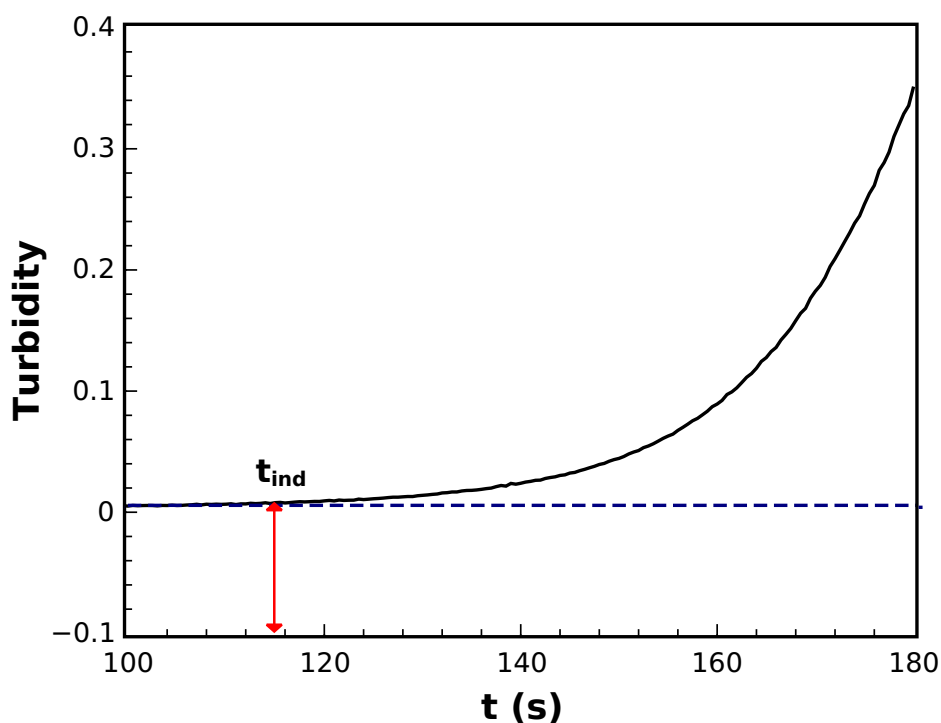


Figure 5.1: An example showing how the induction time ( $t_{ind}$ ) was determined from a turbidity-time measurement

## 5.2 Image Analysis

After the images were collected from the experiments, they were then converted to an easy to handle extension ".png", and automatically changed the time-stamped file names to a suitable series using an in-house program (for details of the program see Appendix III). The images were analyzed by a specially designed macro of ImageJ (for details of the program see Appendix IV). When the macro is run as a plugin in ImageJ, it aids the uploading of the image sequence and the drawing of a vertical, horizontal, or diagonal line on the image of the particle for the entire sequence. This macro automatically scans all the images in the sequence under the selected line and records their greyscale intensities. Lower intensities correspond to the boundaries of the particle. When the scan is complete, a data file is generated and saved in the same directory as the images. An in-house program `xlocext`, which differentiates the intensity values in the earlier generated data file, is then employed to locate the two extrema corresponding to the boundaries of the particle in the image sequence. As shown in Fig. 5.2, the intensity of the particle measured under a selected horizontal line placed on the image of the particle is represented by  $I_x$  and the differentiated intensity under the line by  $dI_x/dx$ . The differentiated maximum and minimum intensities  $m$  and  $n$ , respectively, correspond to the edges of the particle under the line. The resulting data file, containing the positions of maximum intensities, was then processed in a commercially available program (`qtplot`). The particle diameter  $d_x$  is determined from the difference  $|n - m|$ , for any particle growing along or transverse to the direction of flow. Similarly, this image analysis technique was employed to measure the growth of the 3D lithium phosphate precipitate structure.

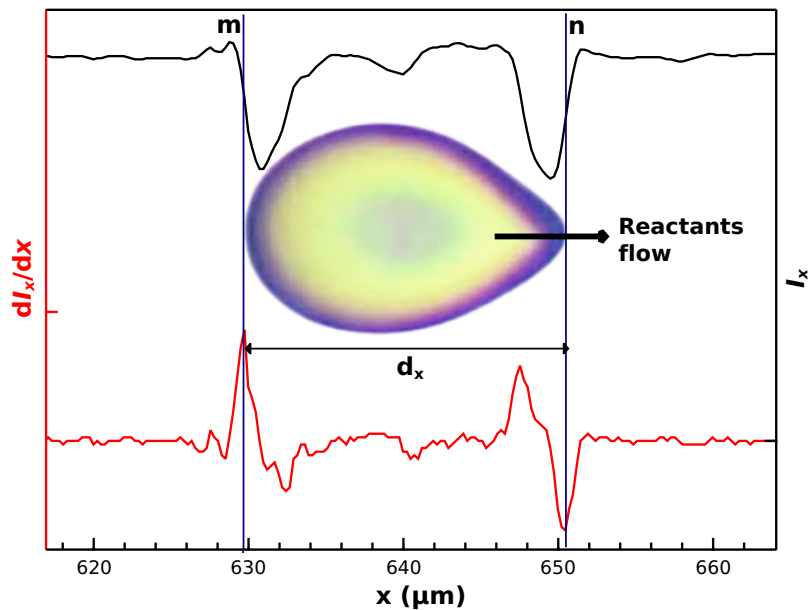


Figure 5.2: Detailed description for determination of the size of a particle along the direction of flow obtained from microfluidics experiment: the intensity of the particle under selection (black line) and the differentiated intensity under the selection (red line).

## **5.3 Techniques**

The following techniques were employed to aid the understanding of the precipitates formed during the course of the experiments.

### **5.3.1 Ultraviolet-visible spectrophotometry**

This technique works on the principle of absorption or reflectance of incident light in the ultraviolet and visible regions of the electromagnetic spectrum. Atoms and molecules undergo electronic transitions in this region of the spectrum. Absorption spectroscopy analyzes these transitions from the ground state to the excited state [182]. The most common samples for UV-visible spectrophotometry are liquids, however, the absorbance of gases and even solids can be studied. Samples are placed in a cuvette, then placed along the path of light to measure any changes in the solution composition. In our experiment, the presence of solid material in a sample leads to a change in the turbidity of the initial solution. The absorbance of the solution was measured at a fixed wavelength of 340 nm (to minimize the absorbance of the reactant solutions [45]) and recorded as the turbidity of the sample (see sections 4.2.1 and 5.1 for details).

### **5.3.2 Scanning electron microscopy**

SEM is a technique that uses a concentrated beam of electrons to scan the surface of a sample and obtain images about it. When electrons interact with atoms in the sample, they produce a variety of signals that carry information about the surface topography and composition of the material. A raster scan pattern is used to scan the electron beam, and the position of the beam is combined with the intensity of the detected signal to create an image [183, 184].

The microstructure of the particles from our experiments was determined from images by a scanning electron microscope (Hitachi S4700). The dry products were placed on an adhesive carbon paper and sputtered with gold in a vacuum for 1 minute to improve the conductivity of the surface of the particles, then microscopic images were taken. The vacuum accelerating voltage in the SEM was 20 kV for high resolution, at a working distance of 12 mm.

### **5.3.3 X-ray diffractometry**

In this method, X-ray impacting an array of regular shaped materials produces diffraction at certain angles of impact. This diffraction data which is found to be unique for different crystal systems aids the understanding of the arrangement of the crystallites. X-ray diffractometry (XRD) is a powerful tool that can provide information about the size of the crystallites

making up the crystal. It can also assist in the identification of the material of the sample.

The X-ray diffractograms of the powdered  $\text{Li}_3\text{PO}_4$  samples were recorded on a Philips X-ray diffractometer with copper ( $K\alpha = 0.1542$  nm) as the radiation source at ambient temperature in the  $2\text{--}70^\circ$  ( $2\theta$ ) range applying  $0.02^\circ$  step size. The sample was identified by comparing the diffraction patterns with the patterns in the in-built database of Match program. The percentage crystallinity was calculated as the ratio of the area of crystalline peaks to the the total area of all peaks. The crystallite sizes were determined using the Scherrer equation

$$\mathcal{D} = \frac{\mathcal{K} \lambda}{\beta \cos \theta} \quad (5.1)$$

where  $\mathcal{K} = 0.9$  is the Scherrer constant,  $\mathcal{D}$  is the crystallite size,  $\lambda$  is the wavelength of the radiation source,  $\beta$  is the width at half of the maximum intensity, while  $\theta$  is the Bragg angle in radians.

### 5.3.4 Density measurement

Density is the ratio of the mass of a solution to its volume. It can be measured directly using a density meter. A digital density meter works on the principle of oscillation of a U-shaped tube. When the tube is filled up with a sample, it begins to vibrate at a frequency depending on the sample in the tube. The frequency of oscillation is then correlated with the density of the sample [185].

The density of our sample was measured with  $10^{-4}$  g/cm<sup>3</sup> precision at room temperature by injecting the solution into a density meter (Anton Paar, DMA 500) and allowing it to stand until a stable reading is observed. The density meter was first calibrated by measuring the density of distilled water.

### 5.3.5 Viscosity measurement

Viscosity is the measure of the resistance of fluids to shear flow when an external force is applied. In general, to measure the viscosity of a solution, there are two methods available: the fluid remains stationary while an object passes through it, or the object remains stationary while the fluid flows around it [186] to measure the resistance. We measured the dynamic viscosity of our solutions directly with 1.0 % precision at room temperature using a rotational viscometer (Anton Paar, ViscoQC 300). We suspended the spindle of the viscometer in the static sample solution with the spindle rotating in the solution. The viscosity value was taken when the reading on the viscometer is stable after standing for a while.

### 5.3.6 Conductivity measurement

Conductivity is a measure of the ease at which a material allows the passage of electricity or heat through it. When ionic solids dissolve in water, ions are released, which conduct electricity. In order to measure these characteristics, a conductivity meter, consisting of four platinum electrodes is used. The electrodes are cylindrical and concentrically oriented. The outer set of electrodes receives an alternating current, then the potential between the inner electrode pair is determined.

To determine the solubility product of the precipitate, the conductivity electrode was placed in a 100 mL beaker containing 70 mL of distilled water. Then 7 g of the dried powdered precipitate was added to the distilled water and stirred continuously. The conductance of the resulting solution was measured on a conductivity meter (Thermo Orion, 420A Plus), in an interval of 20 s until a stable reading is obtained (Fig. 5.3). The conductivity  $\kappa = L \times \mathcal{C}$ , where  $\mathcal{C}$  is the cell constant determined separately and  $L$  is the conductance, was obtained from the measurement ( $L_0$ ) after subtracting the conductivity of ion-exchanged water giving  $\kappa = 0.102 \pm 0.003 \text{ S m}^{-1}$ . From this value and the limiting ionic conductivities of the individual ions,  $\lambda_{iS}$ , the concentration of the electrolyte in solution  $c_{salt}$  was calculated as

$$c_{salt} = \frac{\kappa}{3\lambda_{\text{Li}^+} + \lambda_{\text{PO}_4^{3-}}} = 0.0026 \text{ M}, \quad (5.2)$$

with  $\lambda_{\text{Li}^+} = 0.00387 \text{ S m}^2 \text{ mol}^{-1}$  and  $\lambda_{\text{PO}_4^{3-}} = 0.02784 \text{ S m}^2 \text{ mol}^{-1}$  obtained from Ref. [187]. Hence, the solubility product,  $K_{sp}$ , is determined as

$$K_{sp} = 3^3 \cdot 1^1 \left( \frac{c_{salt}}{c^\theta} \right)^{3+1} = (1.3 \pm 0.2) \times 10^{-9}, \quad (5.3)$$

where  $c^\theta = 1 \text{ M}$  is the standard concentration.

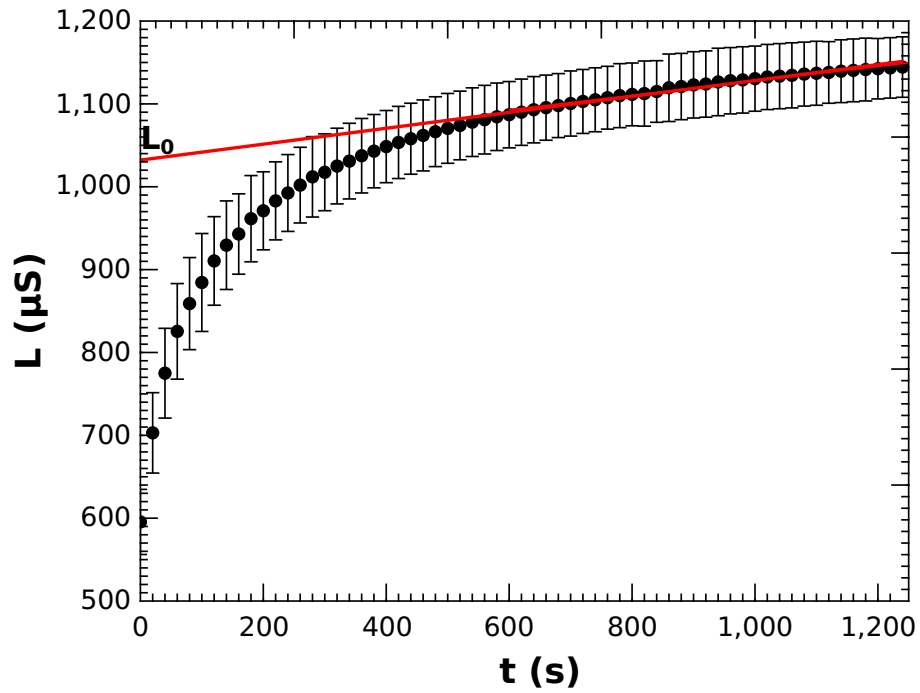


Figure 5.3: A plot of the conductance of a solution containing dispersed lithium phosphate solute as a function of time, with the red line fitted to the range with the slowest conductance change.

# Chapter 6

## Results and Discussions

### 6.1 Speciation of precipitates and complex ions

To determine the pH of the reaction where the lithium phosphate precipitate is at maximum with no or insignificant amount of other products, equilibrium calculations were performed, taking into account the precipitation of lithium phosphate



phosphate ion protonation along with their protonation constants,  $K_{H,i}$ , as



and complexation reaction with lithium leading to the formation of lithium hydroxide [188] according to the reaction



where  $\beta_1$  is the stability constant for LiOH complex [188].

The calculations were performed in the pH range 0–14 in 0.01 pH unit increments, with 0.09 M total lithium ion and 0.03 M total phosphate ion concentrations according to a balanced stoichiometric reactions. First of all, to determine the pH at which lithium phosphate precipitate appears in solution, we calculated the concentration of lithium ions and that of the phosphate ions. As long  $[\text{Li}^+]^3[\text{PO}_4^{3-}] < K_{sp}$ , there will be no precipitation according to

the following equations:

$$[\text{HPO}_4^{2-}] = [\text{H}^+][\text{PO}_4^{3-}]\text{K}_{\text{H1}} , \quad (6.6)$$

$$[\text{H}_2\text{PO}_4^-] = [\text{H}^+]^2[\text{PO}_4^{3-}]\text{K}_{\text{H1}}\text{K}_{\text{H2}} , \quad (6.7)$$

$$[\text{H}_3\text{PO}_4] = [\text{H}^+]^3[\text{PO}_4^{3-}]\text{K}_{\text{H1}}\text{K}_{\text{H2}}\text{K}_{\text{H3}} , \quad (6.8)$$

$$[\text{LiOH}] = \beta_1 \text{K}_w \frac{[\text{Li}^+]}{[\text{H}^+]} . \quad (6.9)$$

The concentration of the phosphate ion was calculated from the balance equation given as

$$[\text{PO}_4^{3-}]_{\text{T}} = [\text{PO}_4^{3-}] + [\text{HPO}_4^{2-}] + [\text{H}_2\text{PO}_4^-] + [\text{H}_3\text{PO}_4] , \quad (6.10)$$

and the  $[\text{Li}^+]$  from that given as

$$[\text{Li}^+]_{\text{T}} = [\text{Li}^+] + [\text{LiOH}] . \quad (6.11)$$

Once  $[\text{Li}^+]^3[\text{PO}_4^{3-}] > \text{K}_{\text{sp}}$ , precipitate appears, hence, we modified the calculation to take it into consideration (the input data file in Wolfram Mathematica is described in detail in Appendix V) according to the following equations:

$$[\text{PO}_4^{3-}]_{\text{T}} = [\text{PO}_4^{3-}] + [\text{HPO}_4^{2-}] + [\text{H}_2\text{PO}_4^-] + [\text{H}_3\text{PO}_4] + [\text{Li}_3\text{PO}_4\text{s}] , \quad (6.12)$$

$$[\text{Li}^+]_{\text{T}} = [\text{Li}^+] + [\text{LiOH}] + 3[\text{Li}_3\text{PO}_4\text{s}] . \quad (6.13)$$

Figure 6.1 shows that at  $\text{pH} < 8.2$ , there is no lithium phosphate precipitation. The solution contains the complex ions of  $\text{HPO}_4^{2-}$ ,  $\text{H}_2\text{PO}_4^-$  and  $\text{Li}^+$ . But as the pH increases above 8.2, lithium phosphate precipitate begins to appear in the solution. At a pH range of 11–12, the amount of lithium phosphate precipitate is at a maximum, which is up to 30 % of the initial lithium ion concentration. In this pH range, the dominant species in the solution is the lithium phosphate precipitate, while the amount of lithium hydroxide is negligible. This, therefore, prompted the use of a tribasic sodium phosphate whose solution has a pH of 12 to maximize the precipitation of the lithium phosphate.

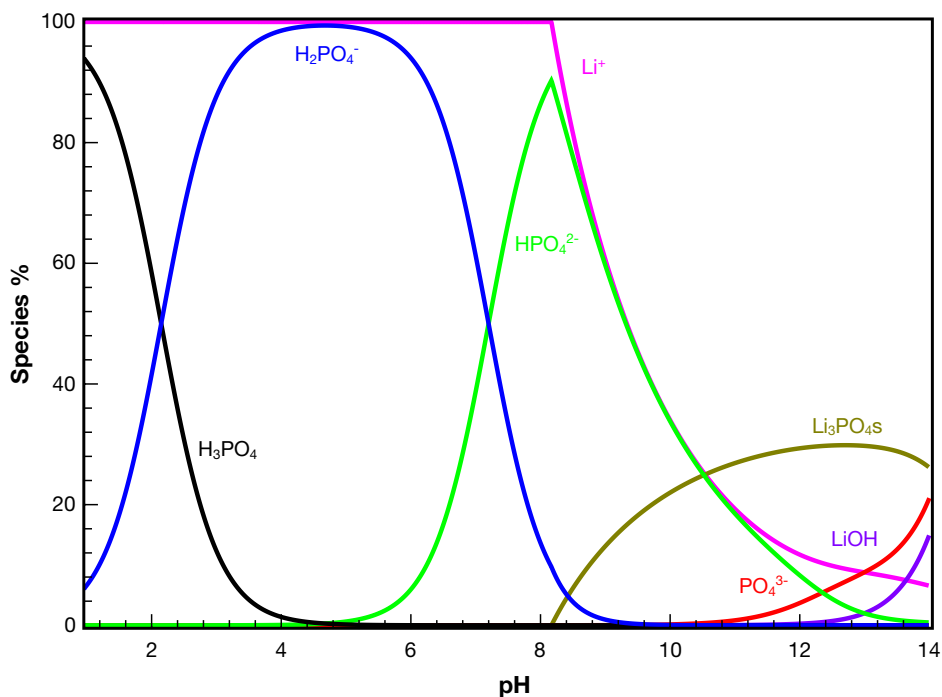


Figure 6.1: Speciation diagram for the precipitation of lithium phosphate,  $[\text{Li}^+] = 0.09 \text{ M}$  and  $[\text{PO}_4^{3-}] = 0.03 \text{ M}$ .

When the reactant ratio is increased to 6 and 10 at constant  $[\text{PO}_4^{3-}]_{\text{T}}$ , as used in the experiments with a microfluidic system, the pH for the formation of lithium phosphate and the percentage of the initial amount of lithium ion consumed decreases as shown in Fig. 6.2(a) and 6.2(b) with the amount of lithium hydroxide formed still at a negligible percentage at the working pH range of 11–12.

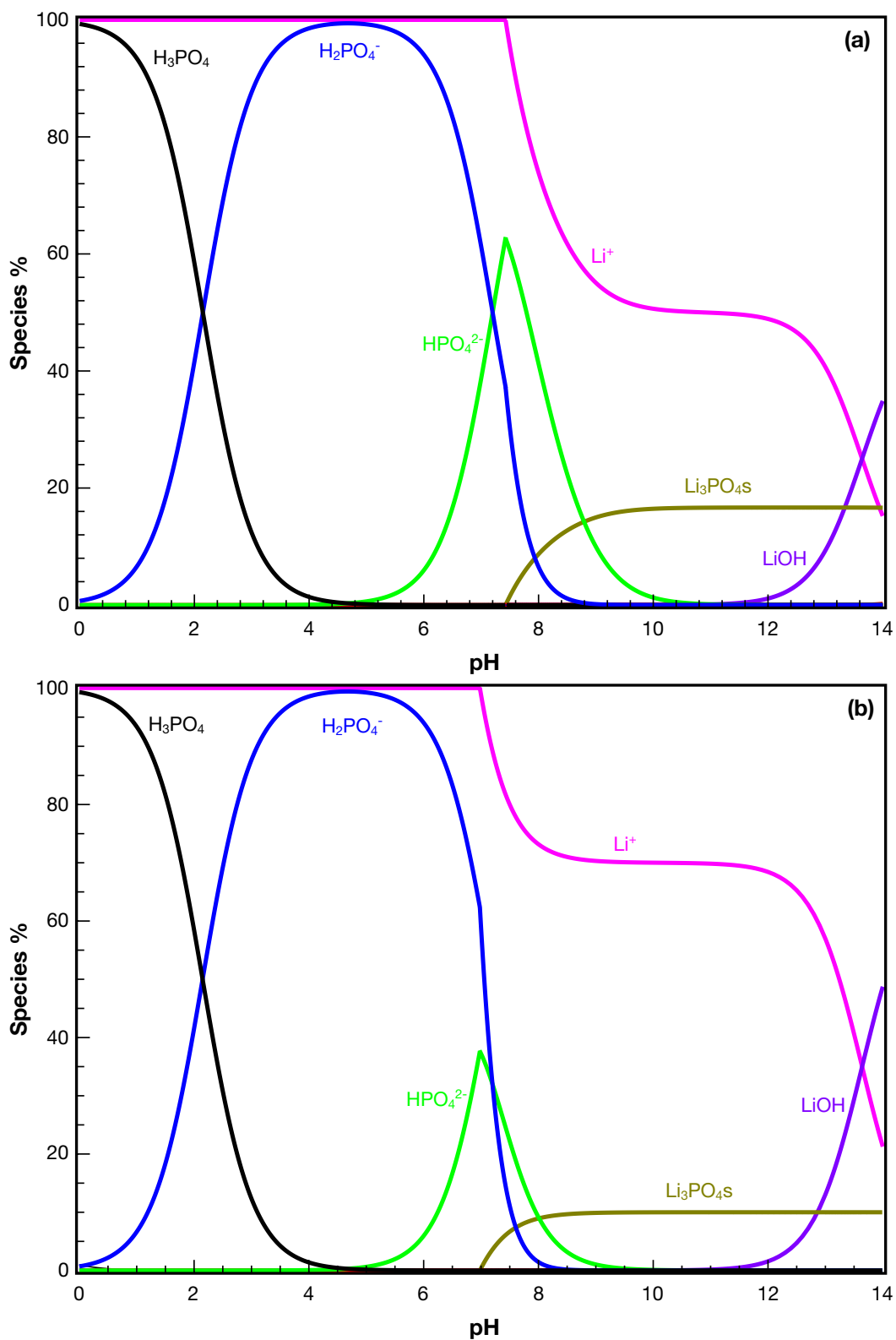


Figure 6.2: Speciation diagram for the precipitation of lithium phosphate,  $[\text{Li}^+] = 0.18 \text{ M}$  and  $[\text{PO}_4^{-3}] = 0.03 \text{ M}$  (a), and  $[\text{Li}^+] = 0.3 \text{ M}$  and  $[\text{PO}_4^{-3}] = 0.03 \text{ M}$  (b).

## 6.2 Nucleation in well-stirred system

From the spectrophotometric measurements, we obtained turbidity-time progression of the reaction consisting of an initial interval where the turbidity of the solution is almost zero indicating no apparent reaction or the formation of a visible particle (1) as shown in Fig. 6.3. This is followed by a period of a rapid increase in turbidity from where nucleation and growth begin (2). The growth could be dominated by either the increase in the number of nucleation sites or in crystal size until maximum turbidity or plateau is reached. The solution finally becomes saturated with the precipitate (3) with a possibility of aggregation. The plateau reached in turbidity is also dependent on the concentration of the reactants, with the highest plateau obtained at the highest concentration investigated (Fig. 6.3). As detailed in section 5.1, the induction time,  $t_{ind}$ , was determined from the turbidity-time profile and used to calculate the kinetic parameters for nucleation.

Although it was often reported that induction times for given conditions (stirring rate, temperature, reaction vessel) are stochastic between experimental repeats, especially at small volumes [189, 190], those obtained from our experiments are fairly reproducible in the concentrations and time ranges with minimal fluctuations. The increase of reactant concentration not only shortens the induction period by increasing the reaction rate, but also increases the turbidity at the end of the growth period due to the production of more precipitates.

We have not observed the dependence of the induction time on the material of the cuvette

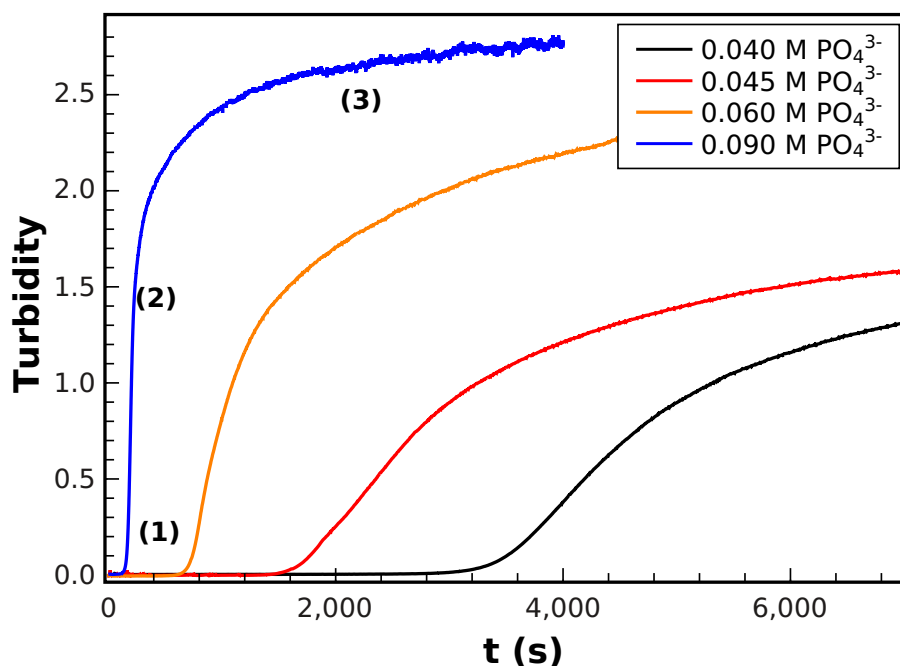


Figure 6.3: Typical turbidity-time profile for the precipitation of lithium phosphate with no apparent reaction (1), nucleation and growth (2), saturation and/or aggregation (3)

or solid contamination in the solution, suggesting that homogeneous nucleation dominates the process. This is indicated by the similarity in induction times regardless of the material of the cuvette as seen in Table 6.1. When the solutions are unfiltered and may contain impurities, we observed a shorter induction time in both of the cuvettes. These observations are in accordance with the very high supersaturation used ( $S = 1.0 \times 10^4 - 2 \times 10^6$ ) and the filtration of the reacting solutions prior to mixing, in which case induction times are relatively short and the rate of nucleation is fast, with no time for external particles, such as dust or quartz surface, to induce nucleation significantly.

Table 6.1: Induction times for the precipitation of lithium phosphate in glass and quartz cuvettes at different concentrations.

$[\text{PO}_4^{3-}]$ (M)	<i>Material</i>	<i>Solution</i>	$t_{ind}$ (s)	<i>Stdev.</i>
0.06	glass	Filtered	562	36
0.06	quartz	Filtered	565	36
0.06	glass	Unfiltered	313	60
0.06	quartz	Unfiltered	369	6
0.10	glass	Filtered	46	6
0.10	quartz	Filtered	45	6
0.10	glass	Unfiltered	37	4
0.10	quartz	Unfiltered	38	3

The induction time is inversely proportional to the rate of nucleation [60]. Hence the concentration dependence is sought as a power law in the form of

$$rate \propto \frac{1}{t_{ind}} = a'[\text{PO}_4^{3-}]^b \quad (6.14)$$

as shown in Fig. 6.4 because the reactant ratio is kept constant at  $R = 3$ . The experimentally determined exponent in the power law is the reaction order,  $b = 4.25 \pm 0.04$ . This indicates that the association of reactant ions takes place in the apparent rate determining step for nucleation. The apparent rate constant for nucleation is  $a' = (3.5 \pm 0.3) \times 10^{-3} \text{ M}^{-b} \text{ s}^{-1}$ .

We have developed a kinetic model for the precipitation of lithium phosphate [191] con-

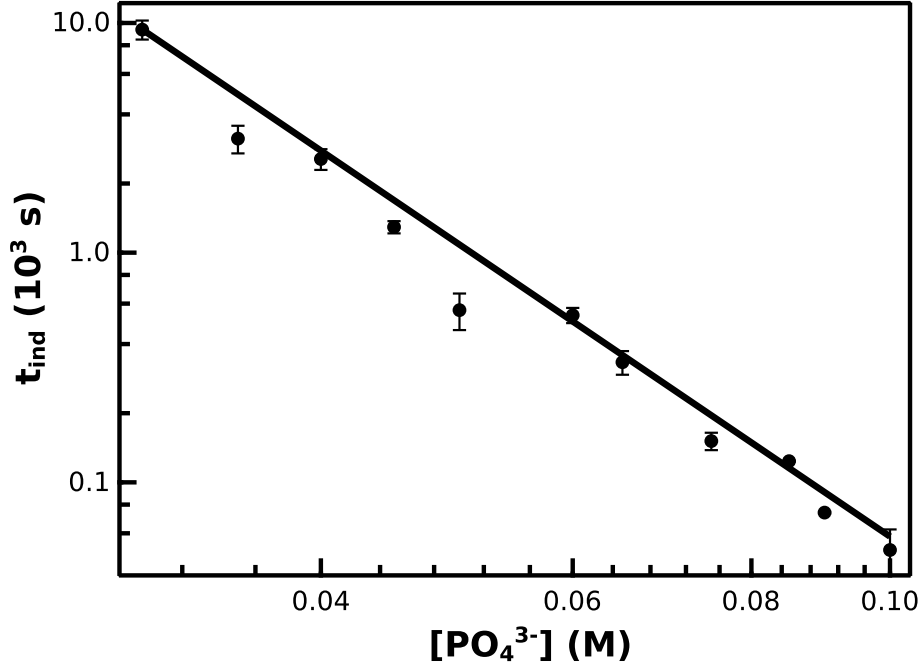
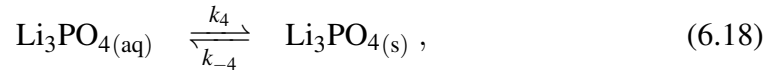
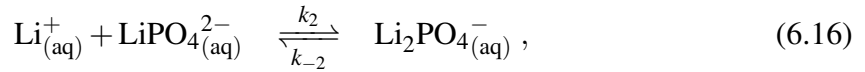
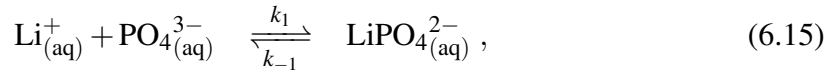


Figure 6.4: Nucleation rate as a function of concentration at  $T = 25\text{ }^\circ\text{C}$ . The solid line shows the fitting by Eqn. 6.14.

sisting of the following steps [191]: \*



where  $k_i \ll k_{-i}c^0$ ,  $i \in [1, 3]$  at room temperature,  $k_i = 0.378\text{ m}^3/(\text{s mol})$ ,  $k_{-i} = 10^5\text{ s}^{-1}$ ,  $i \in [1, 3]$ ,  $k_{-4} = 500\text{ s}^{-1}$ ,  $k_4 = k_{-4}/KK_{sp}$ , with  $K$  being the overall equilibrium constant and  $K_{sp}$ , the solubility product of lithium phosphate. When a cluster of a colloidal lithium phosphate is formed, it either grows or dissolves back into the solution until a critical cluster size is reached, as described by the assumptions of CNT model [80, 81]. When a stable cluster is formed, it rearranges and come together to form a crystal surface from which growth into a detectable size takes place.

This concentration dependence is also related to the CNT, according to which nucleation rate  $J$  can be expressed as a function of supersaturation [60] as described by Eqn. 2.6 with

\*The modelling was carried out by Paszkál Papp, therefore the details are not included in the dissertation.

the supersaturation  $S$  being defined as

$$S = \frac{[\text{Li}^+]^3[\text{PO}_4^{3-}]}{K_{sp}} \quad (6.19)$$

where  $K_{sp} = (1.3 \pm 0.2) \times 10^{-9}$  is the solubility product of lithium phosphate, determined from independent conductance measurements. Since  $t_{ind} \propto J^{-1}$ , Eqn. 2.11 is fitted on the measured data in Fig. 6.5 from which the kinetic parameter is  $A = 1.016 \pm 0.560$  and the thermodynamic parameter is  $B = 908 \pm 106$ . The volume  $V = 8.014 \times 10^{-29} \text{ m}^3$  of the solid particle is according to Eqn. 2.7 [83], with  $M_w = 115.79 \text{ g/mol}$  and  $\rho_c = 2.397 \text{ g/cm}^3$ . From the volume of the solute, the kinetic parameter is  $A' = (12.3 \pm 6.8) \times 10^{27} \text{ m}^{-3} \text{ s}^{-1}$ , similar to typical values estimated by CNT for homogeneous nucleation [192, 193], indicating that CNT can be effectively used in the estimation of nucleation parameters of  $\text{Li}_3\text{PO}_4$ . The interfacial energy,  $\gamma$ , was then calculated from Eqn. 2.12 as  $\gamma = 84 \pm 3 \text{ mJ m}^{-2}$ .

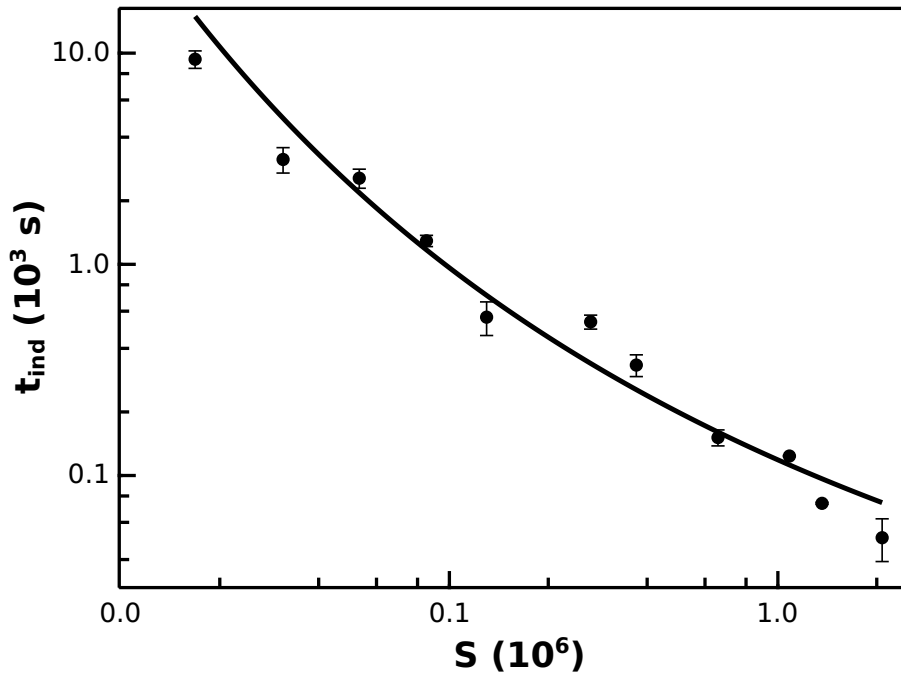


Figure 6.5: Induction time as a function of supersaturation. The solid line indicates data fitting with Eqn. 2.11

The surface tension falls in the range of 68–97  $\text{mJ m}^{-2}$  found for weakly soluble inorganic salts like  $\text{CaHPO}_4 \cdot 2\text{H}_2\text{O}$ ,  $\text{CaSO}_4 \cdot 2\text{H}_2\text{O}$ ,  $\text{CaCO}_3$  [194–196]. The value also matches the estimation of solid-liquid interfacial tension by Mersmann's equation [197], according to

$$\gamma_{SL} = 0.414 k_B T \left( \frac{\rho_c N_A}{M_w} \right)^{2/3} \ln \left( \frac{c_S}{c_L} \right) \quad (6.20)$$

where  $c_S = \rho_c/M_w = 20.7$  M is the concentration of the solid while  $c_L = 2.6$  mM is the solubility in the liquid phase, resulting in  $\gamma_{SL} = 82$  mJ m<sup>-2</sup>.

From the parameters determined in the CNT, it is justified that the steps involved in the nucleation of Li<sub>3</sub>PO<sub>4</sub> are such that the spontaneous formation of a stable colloidal cluster from the ions in solution alone led to the formation of a nucleus from which the crystals grow. Although insignificant contributions of heterogeneous surfaces might affect the nucleation, many experimental data fittings done in the literature neglect the contributions of the ionic chemical potential to the supersaturation of the solution. An example is a work of Sohnel and Mullin (1978) [194] where the nucleation kinetics of calcium carbonate was determined. The supersaturation calculated did not take into account the contribution of the ions to the chemical potential and the prefactor in the CNT. This led to a fitting of two straight lines on the data and a separation into two regions having different nucleation mechanisms. If the contribution of the ions to the chemical potential, and subsequently to the prefactor, is accounted for, then

$$\ln t_{ind} = \ln \frac{A'}{S} \exp\left(\frac{B}{\ln^2 S}\right) \quad (6.21)$$

will perfectly fit the experimental data and a single mechanism can be used to describe the nucleation. As illustrated in Fig. 6.6, a fitting with Eqn. 6.21 over the experimental data gives an excellent fit and shows that if the contribution of the ions is not neglected, the linear form of CNT has a bend as in the experimental points [84]. At very high supersaturation the first

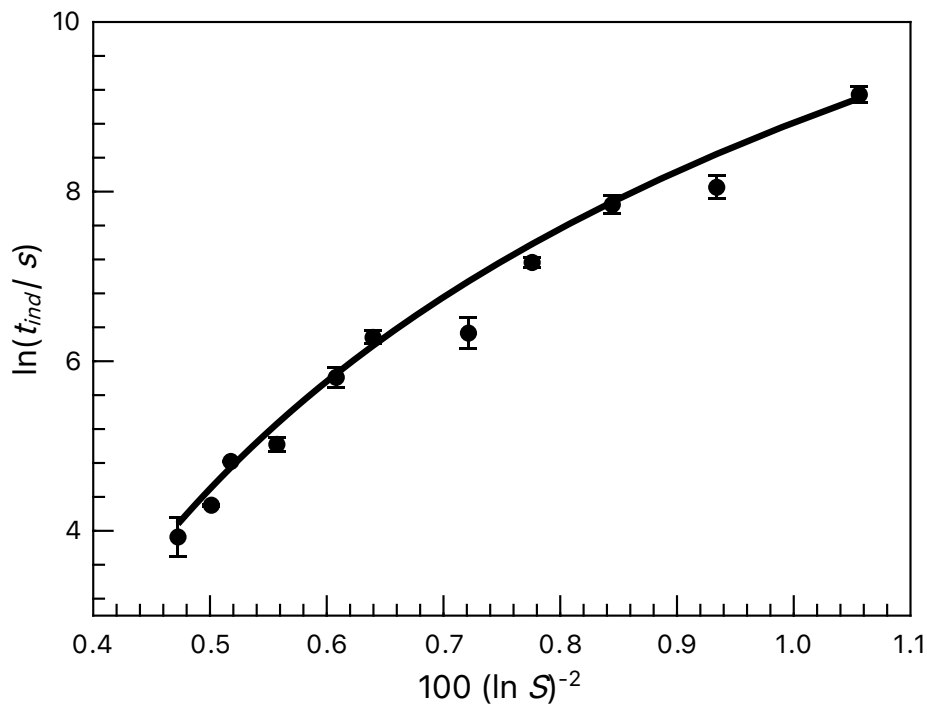


Figure 6.6: Induction time as a function of supersaturation. The solid line indicates data fitting with Eqn. 6.21

part of Eqn. 6.21,  $\ln A'/S$  dominates, hence the bend in the fitted data as opposed to when the supersaturation is low and  $1/\ln^2 S$  dominates.

Because of the temperature dependence of the rate coefficients, induction time is expected to increase exponentially with  $T^{-1}$  as

$$t_{ind} \propto \exp\left(\frac{E_a}{RT}\right) \quad (6.22)$$

with constant initial concentrations, since the solution density variation is negligible in the experimental conditions. Figure 6.7 illustrates that a 10 % increase in temperature results in a magnitude increase of reaction rate and, in accordance, a tenfold decrease in the induction time. Direct application of Eqn. 6.22 for induction times, however, indicates that nucleation is slower at higher temperature than expected from measurements at lower temperature with the exponential dependence in Eqn. 6.22. The apparent activation energy at temperatures above 35 °C is about half of that found at lower temperatures (86.3 kJ/mol vs. 175 kJ/mol). This suggests that the rate determining step in the nucleation process is preceded by reaction steps so that the apparent rate coefficient contains several others with different activation energies.

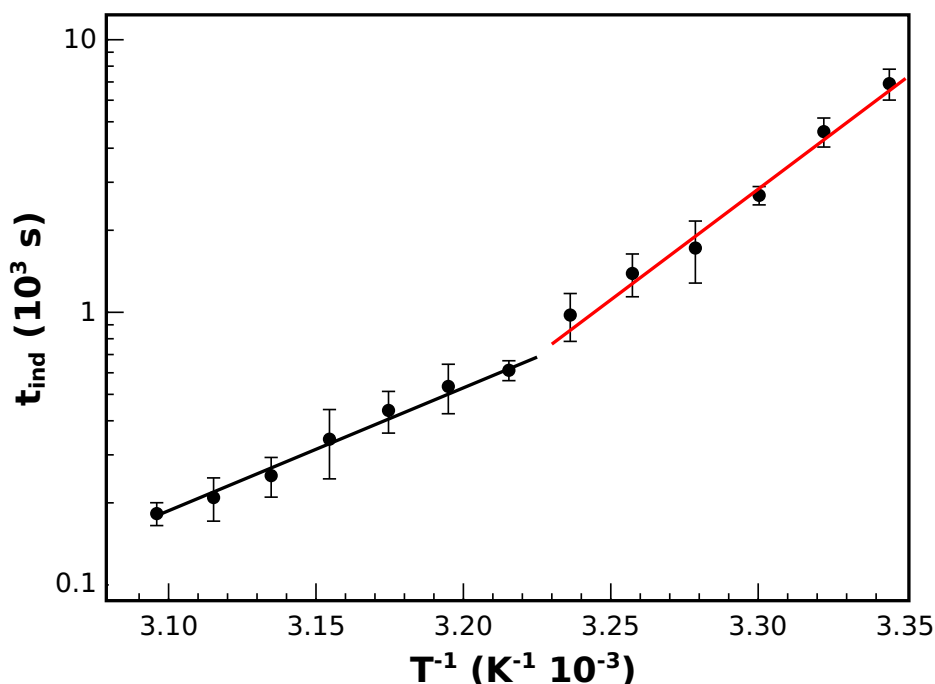


Figure 6.7: Temperature dependence of the induction time for stoichiometric composition with  $[Na_3PO_4] = 0.030$  M. The solid lines correspond to the fitting with Eqn. (6.22).

## Microstructure

Two different crystalline structural forms can be distinguished by SEM images of the precipitates obtained in the well-stirred system (Fig. 6.8(a-f)); at the induction time (a,d), after induction time (b,e), and at the end of the precipitation process (c,f). One of the forms is a flat-sheet-like crystal (Fig. 6.8(d), red square), and the other is a floral shaped crystal (Fig. 6.8(d), green dashed-square) arising from the aggregation of fractured flat-sheet-like crystals caused by vigorous stirring. During fracturing, defects develop where oriented attachment is favored, changing the symmetry of the final morphology. This breakage and aggregation process continuously occur throughout the reaction period giving rise to the mixture of the two forms. Far from the induction time aggregation of the two forms sets in. Similar trend is observed at 36 °C. At 50 °C, however, the crystals grow fast, such that well-defined mixture of the crystals appear almost immediately. The length of the longer side of the flat-sheet-

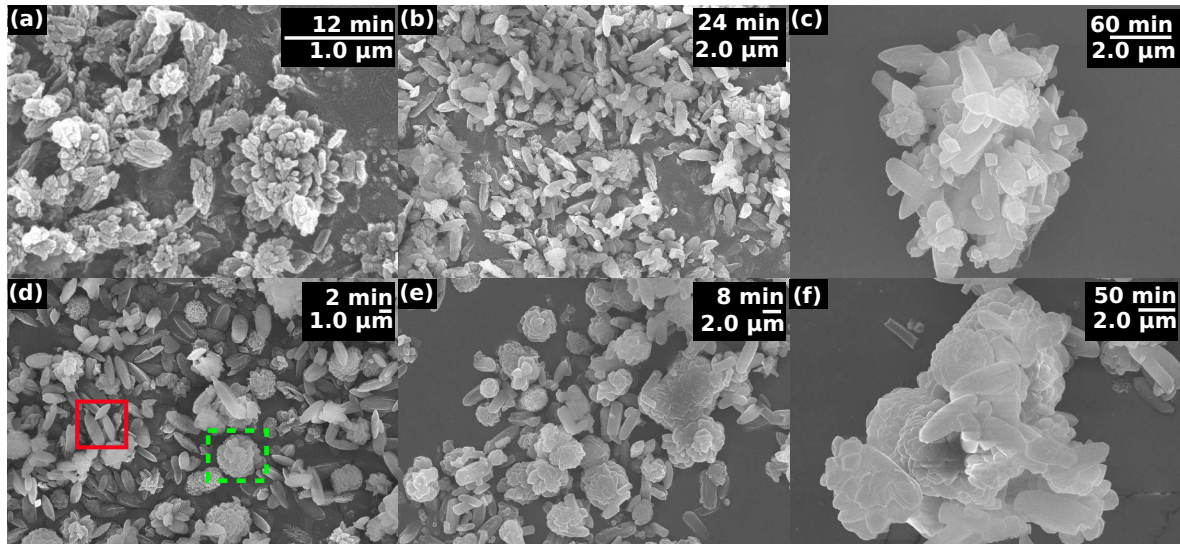


Figure 6.8: SEM images of particles obtained at different temperatures and at different crystallization time: 36 °C (a-c), and 50 °C (d-f), at concentration of 0.03 M : 0.09 M  $[\text{PO}_4^{3-}] : [\text{Li}^+]$  respectively. Red square indicates the flat-sheet-like crystals, and green square shows the floral shaped crystal formed through the aggregation of fractured poorly developed flat-sheet-like crystals caused by vigorous stirring.

like crystals was measured for images obtained at 36 °C, and 50 °C. The results show that at 36 °C and at the induction time (Fig. 6.9(a)), the crystals are mono-dispersed with size  $\approx 0.1 \mu\text{m}$  and polydispersity index  $PDI = 0.07$  where

$$PDI = \left( \frac{\sigma}{2d} \right)^2 \quad (6.23)$$

with  $\sigma$  being the standard deviation of the particle size distribution and  $d$  the average size of the particles. The crystals then grow to an average size of  $\approx 1.0 \mu\text{m}$  and aggregate resulting

to a polydispersed particle size distribution with  $PDI = 0.28$ , 12 min after the induction time. At the end of the investigation time, the crystals grow to an average size of  $\approx 2.0 \mu\text{m}$  and also polydispersed with  $PDI = 0.27$ . Similar trend was observed in the particle size distribution at  $50^\circ\text{C}$  (Fig. 6.9(b)) with polydispersed particles throughout the investigation period.

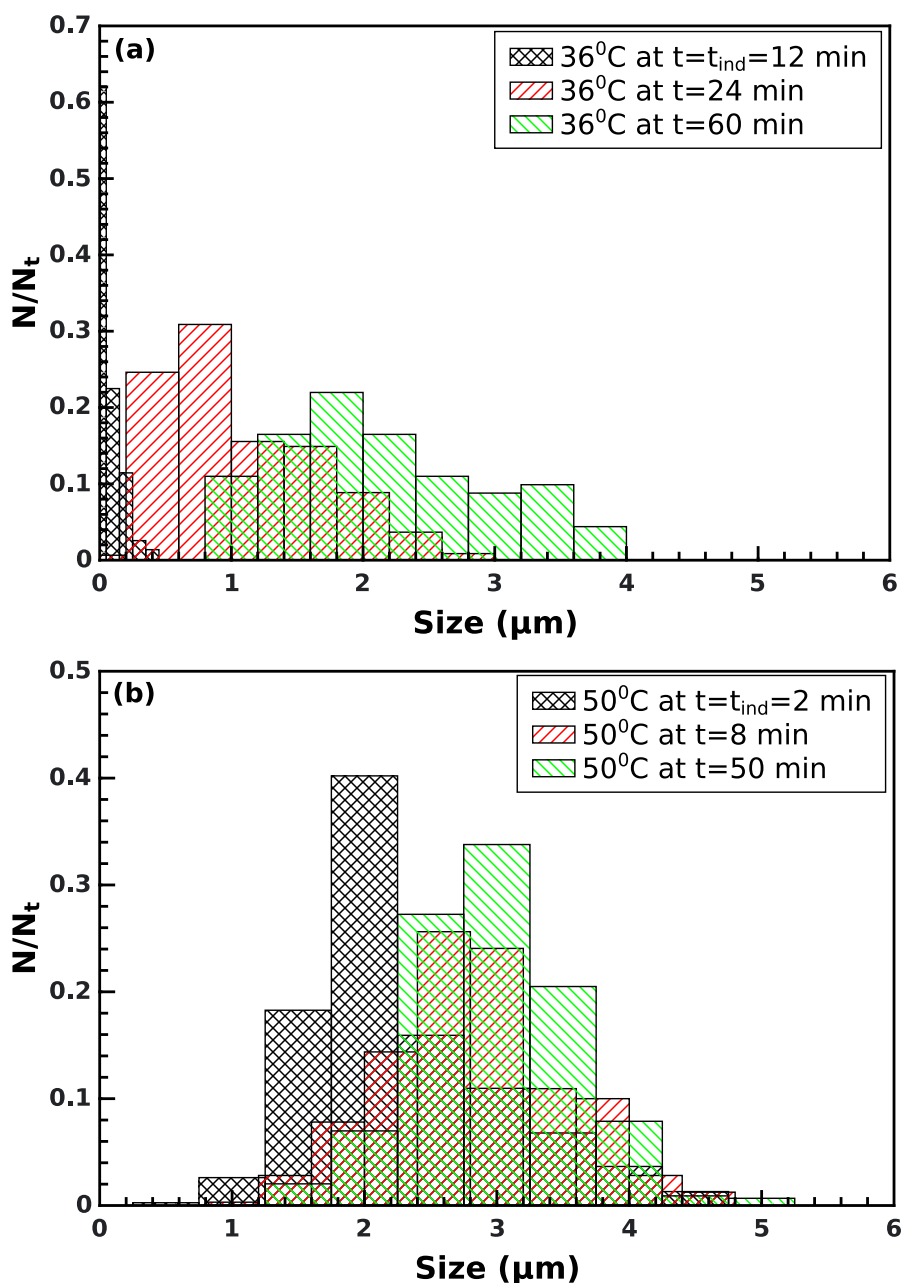


Figure 6.9: Particle size distribution for flat-sheet-like crystals determined from the SEM images of particles collected at  $[\text{Na}_3\text{PO}_4] = 0.03 \text{ M}$  for  $R = 3$  at  $36^\circ\text{C}$  (a) and  $50^\circ\text{C}$  (b).

X-ray diffraction data revealed that the crystals formed are orthorhombic, belonging to the  $Pmn2_1$  space group, known as  $\beta$ - $\text{Li}_3\text{PO}_4$  (Crystallography Open Database, COD:9012500) [198, 199] as in Fig. 6.10, independent of the temperature between 25 and 50 °C.

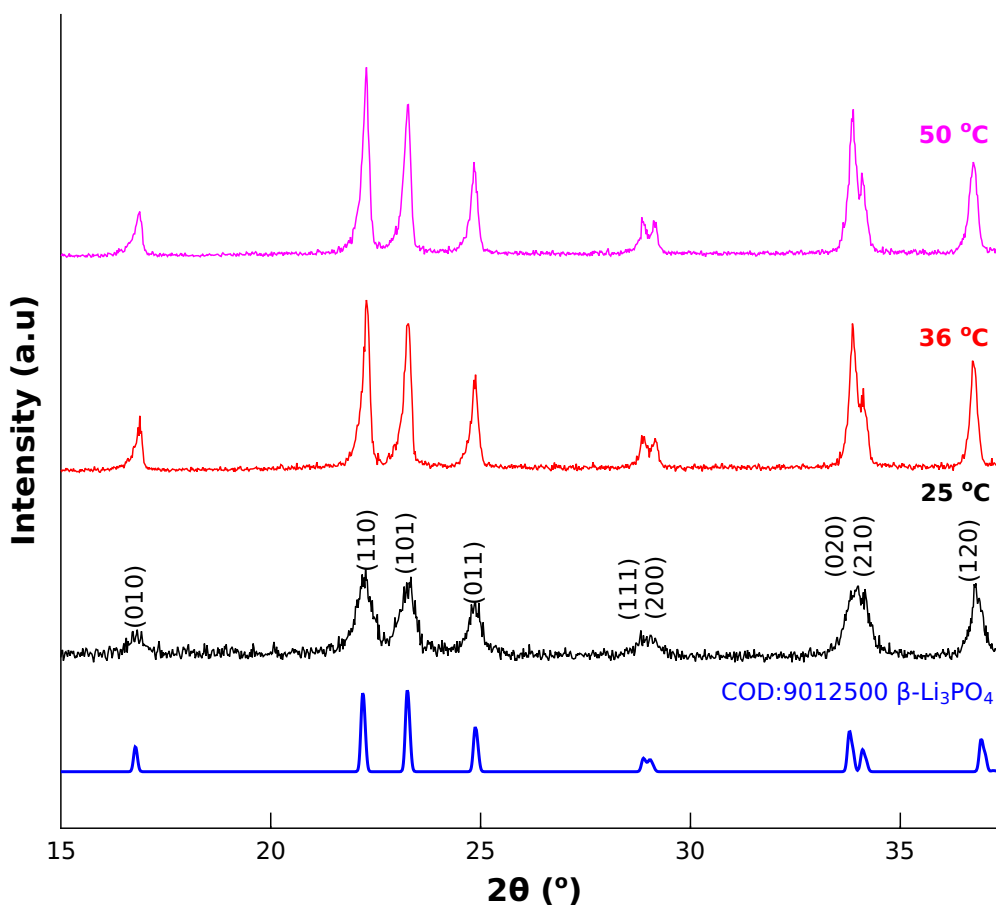


Figure 6.10: X-ray diffractograms of samples prepared in well-stirred experiment when  $R = 3$  at 25 °C, 36 °C, and 50 °C, and standard diffractograms from crystallographic open database for  $\beta$ -lithium phosphate.

At moderate temperature, the average crystallite size summarized in Table 6.2 increases as precipitation progresses. Crystallinity ranges from 59% to 83%, with lower values corresponding to the room-temperature case. Crystallinity increases with time, suggesting that there is a form of ordering taking place from the appearance of the first nucleus. There is one exception, at higher temperature, where the formed material is aggregated leading to a decrease in crystallinity.

Table 6.2: Crystal lattice parameters ( $a, b, c$ ), average crystallite size ( $\mathcal{D}$ ) and crystallinity ( $w_{c,X}\%$ ) for samples with  $[\text{LiCl}] = 0.3 \text{ M}$  and  $[\text{Na}_3\text{PO}_4] = 0.1 \text{ M}$ .

$T$ (°C)	$t$ (min)	$a$ (Å)	$b$ (Å)	$c$ (Å)	$\mathcal{D}$ (Å)	$w_{c,X}$ %
25	180	6.1724	5.3025	4.8856	181	59
36	12	6.0385	5.2649	4.8900	224	68
36	24	6.0836	5.2774	4.6766	222	71
36	60	6.1257	5.2548	4.8950	252	79
50	2	6.1292	5.2774	4.7395	268	72
50	8	6.1292	5.2527	4.8768	313	83
50	50	6.1250	5.2649	4.8900	326	69
<b>COD:9012500</b>		<b>6.1150</b>	<b>5.2394</b>	<b>4.8554</b>	-	-

### 6.3 Quasi 2D crystallization in microchannel

By the use of a fully automated microfluidic setup, lithium chloride and sodium phosphate solutions were injected simultaneously with the same flow rate into a microreactor. The two reactants come into contact near the middle of the channel - with the actual position depending on the ratios of the reactants - where nuclei begin to form. The precipitation takes place along the flow giving rise to a so-called contact line. The nucleation itself is stochastic in time, implying that the time of appearance of the first precipitate particle in the channel is not a reproducible entity due to the small volume of the reacting solutions.

Injecting the reactants at a stoichiometric concentration ratio  $R = 3$ , it was observed that the first particles appear about 8–10 min after starting the flow along the contact line. There are many nucleation sites yielding small sized precipitate particles and hence hindering the growth of the individual particles (see Fig. 6.11(a)).

Upon increasing  $R$  to 6, even after injecting the reactants for 15–20 min, fewer nuclei appear initially as orthorhombic crystals then grow into spherical aggregates which evolve separately as shown in Fig. 6.11(b) [200]. These well-spaced particles along the contact line are the result of the high number of cations in the system compared to the anions due to the lithium ion excess leading to a charge imbalance.

To characterize the growth of individual particles, a minimum of three parallel experiments have been performed with  $R = 6$ , when  $[\text{PO}_4^{3-}] = 0.1 \text{ M}$  for flow rates ranging from 1.0 – 5.0  $\mu\text{L}/\text{min}$ . This reaction ratio and concentration are selected because at this composition the charge imbalance dictates the formation of well-spaced particles whose growth can be characterized. For the selected particles, their position is monitored as a function of time. A typical growth profile is illustrated in Fig. 6.12, where the temporal evolution of the edge of a precipitate particle is presented transverse to the direction of flow, with  $y = 0$  corresponding to the center vertical plane of the channel and  $y > 0$  to the side of the lithium

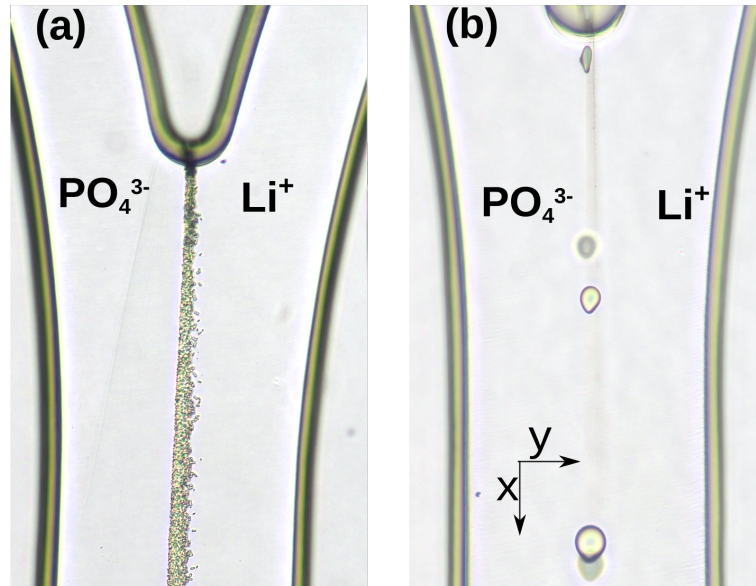


Figure 6.11: Precipitate particle growth in microchannel with  $w = 300 \mu\text{m}$ ,  $q_v = 3.0 \mu\text{L}/\text{min}$  and chemical composition (a)  $R = 3$ , (b)  $R = 6$  at  $t = 45 \text{ min}$ .

source. The distance between the two positions yields the diameter of the particle as it grows transverse to the direction of flow, i.e., along the  $y$ -axis, which is also measured in order to construct the growth profiles. The crystals form mainly in the vicinity of the contact line but on the side of the lithium chloride inlet which is due to its higher concentration gradient.

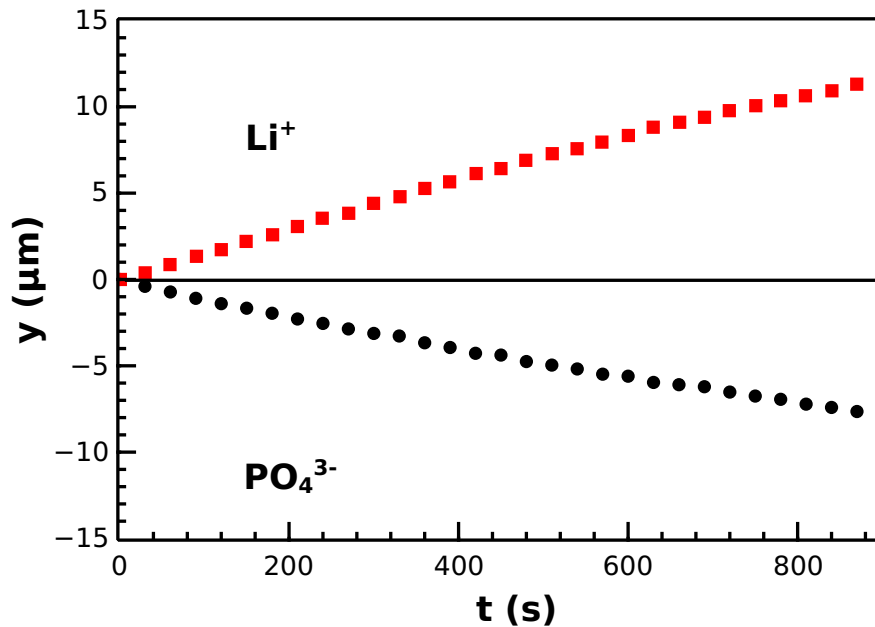


Figure 6.12: Example of the growth characteristics of the transverse extent of a single particle  $638 \mu\text{m}$  from the inlet with  $R = 6$  and  $q_v = 2.5 \mu\text{L}/\text{min}$ . Position  $y = 0$  corresponds to the middle of the channel. The edge plotted with "●" faces the side of the sodium phosphate inlet.

A similar technique is applied to determine the particle growth along the flow allowing us to observe the effect of flow in both directions. First, at a given flow rate, several particles are chosen and their growth characteristics are determined. One example case is summarized in Fig. 6.13, where growth profiles along two directions are depicted for sev-

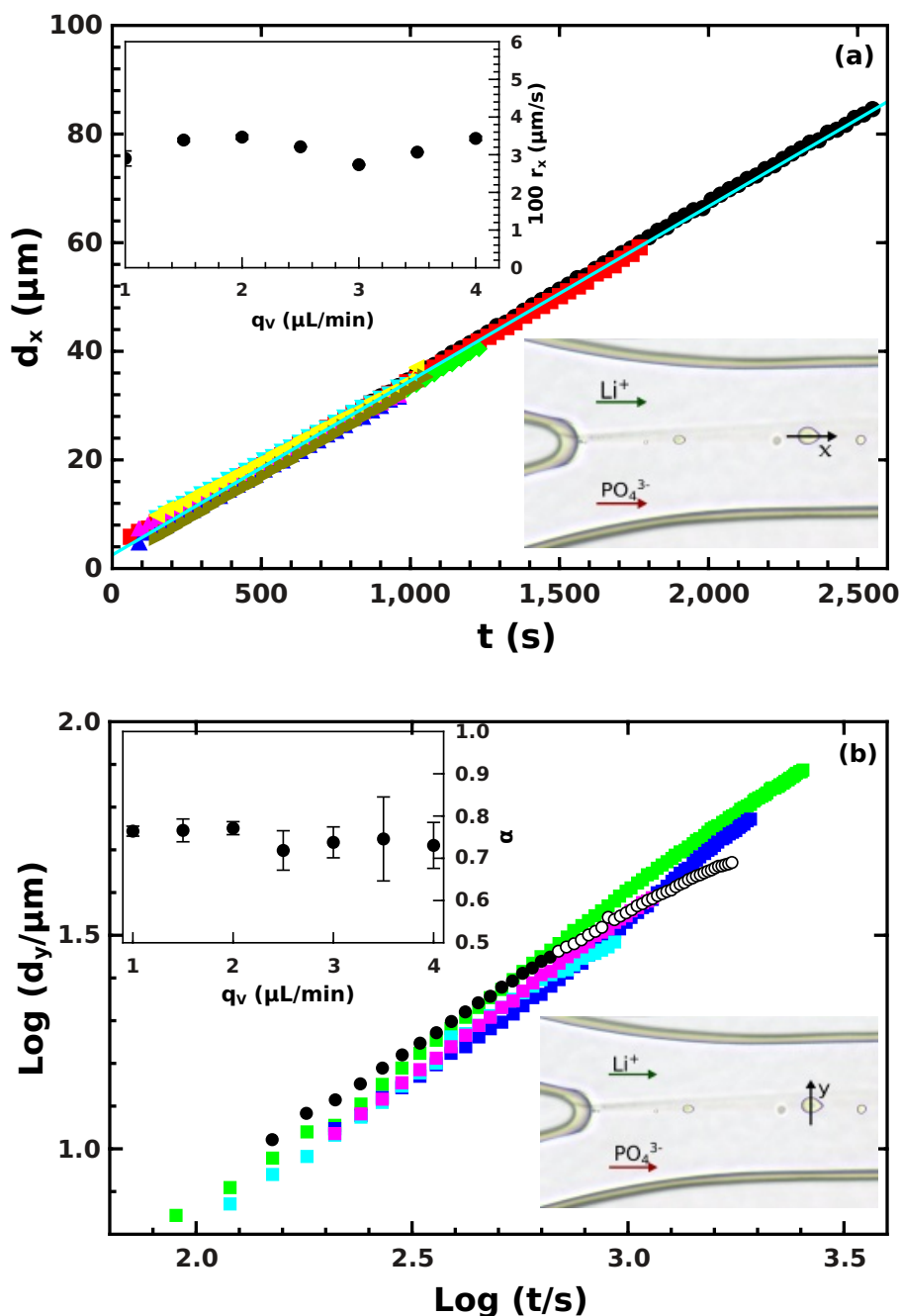


Figure 6.13: Precipitate particle growth profiles for  $q_v = 2.5 \mu\text{L}/\text{min}$  along (a) and transverse to (b) the reactant flow. Particles are 315–1064  $\mu\text{m}$  from the inlet. In (a) the inset shows the independence of growth rate ( $r_x$ ) of the injection rate. In (b) the inset shows the scaling exponent ( $\alpha$ ) of the transverse growth rate.

eral particles. For a given injection rate, the particle diameters along the direction of flow increase linearly in time (cf. Fig. 6.13(a)) for the individual particles independent of the time of appearance and their position as long as the particles are sufficiently separated from each other. From the slope, therefore, we can obtain the constant growth rate of the particles along flow  $r_x$  of  $(3.2 \pm 0.3) \times 10^{-2} \mu\text{m}/\text{min}$  along the flow independent of the particle position and for injection rates in the range of  $1.0 \mu\text{L}/\text{min} \leq q_v \leq 5.0 \mu\text{L}/\text{min}$ . This observed behavior implies that the supersaturation cannot change significantly along the direction of flow (for detailed explanation see Section 6.3.1). This can be rationalized by considering the mean linear flow rate, which falls in the range of 1.1–3.0 mm/s leading to a residence time of less than one second in the view area for the injected fluid. The precipitation reaction is the rate-determining factor yielding a reaction-controlled growth [201] along the flow as the reactants are continuously brought to the contact line by the flow.

The precipitation process in the transverse direction, however, slows down. The size of the precipitate particles along the  $y$ -axis  $d_y$  scales with time  $t$  according to the power law

$$d_y = kt^\alpha \quad (6.24)$$

with  $k$  and  $\alpha$ , the fitting parameters, as shown in Fig. 6.13(b), where the exponent  $\alpha$ , is invariant to the injection rate under our experimental conditions. This is the result of the decrease in supersaturation as the ions move away from the contact line, which lowers the driving force of precipitation. The fast supply of reactants by the flow affects the entire width of the microchannel, therefore the determined exponent is greater than 0.5, which is characteristic of reactions between initially segregated reactants with only diffusional support [202]. Also, in general, the size of the microchannel has no effect on the size or growth rate of the particle. Experiments conducted in a smaller microchannels of  $75 \mu\text{m}$  gave a similar result as those conducted in channels of higher diameter up to  $300 \mu\text{m}$ . This is due to the fact that the minimum amount of ions required for the formation and growth of the particle can be obtained regardless of the channel size and continuously replenished by the flow.

There is a gradual transformation in the shape of the polycrystals formed in the microchannel, when the injection rate is increase from  $0.2 \mu\text{L}/\text{min}$  to  $5.0 \mu\text{L}/\text{min}$  and  $R$  is set to 10 as shown in Fig. 6.14. At low injection rate the crystals are spherical and grow symmetrically maintaining their shape under the investigation period. Upon increasing the injection rate, the particles are smaller at the same time. Furthermore their shapes are slightly distorted, eventually leading to an obovate structure.

Analysis of the growth characteristics indicates that for particles growing under very low injection, a linear profile is observed along and transverse to the flow, yielding within experimental error, the same growth rate of  $(2.6 \pm 0.2) \times 10^{-2} \mu\text{m}/\text{s}$  in both directions (Fig. 6.15 (a)). On the other hand, as the injection rate increases, we observed a deviation in the growth rates yielding a faster rate along the direction of flow and a slowing down transverse

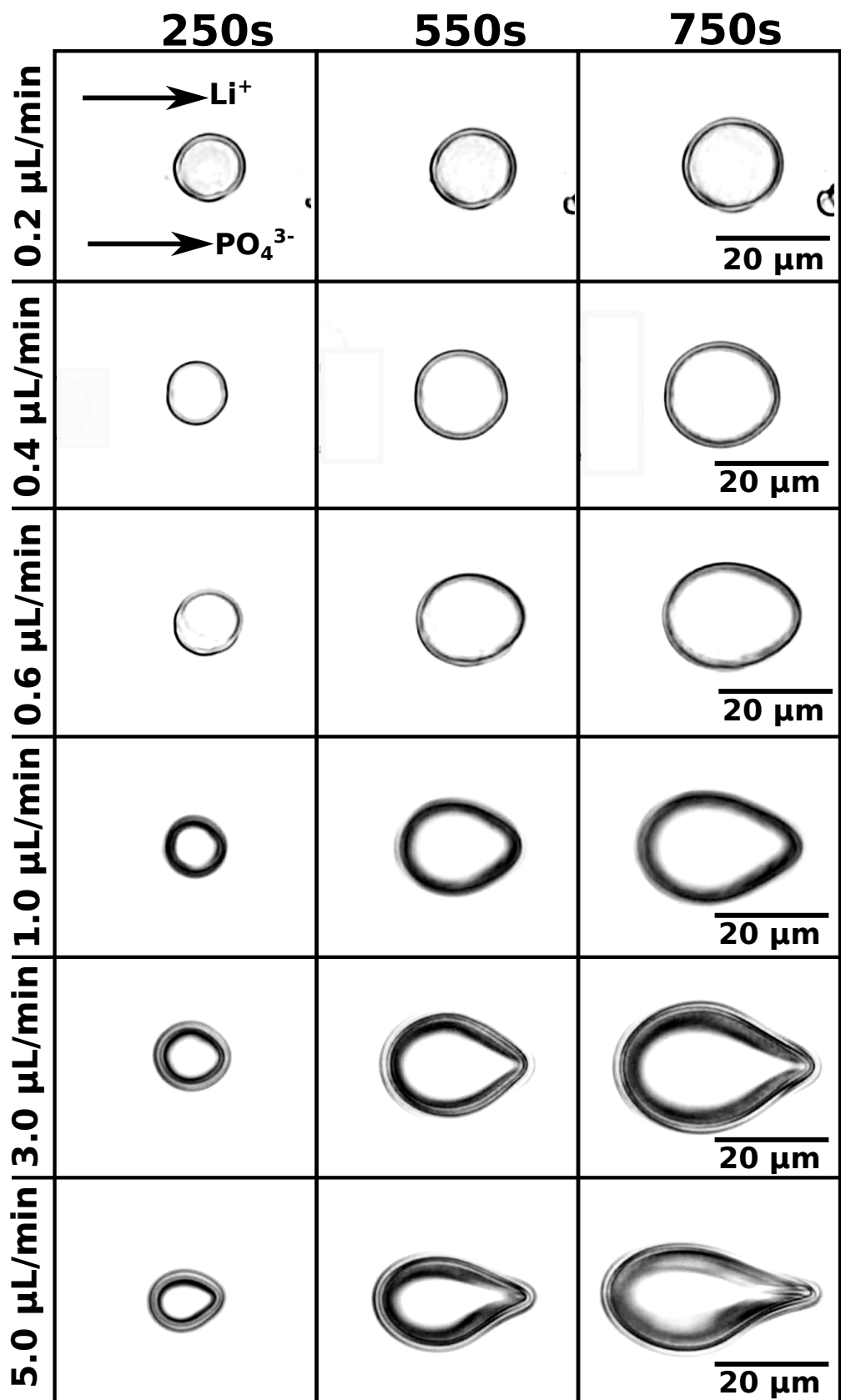


Figure 6.14: Image sequence showing how the increasing injection rate causes a gradual distortion in the particle shape, at  $R = 10$ , when  $[\text{Li}^+] = 0.75\text{M}$ .

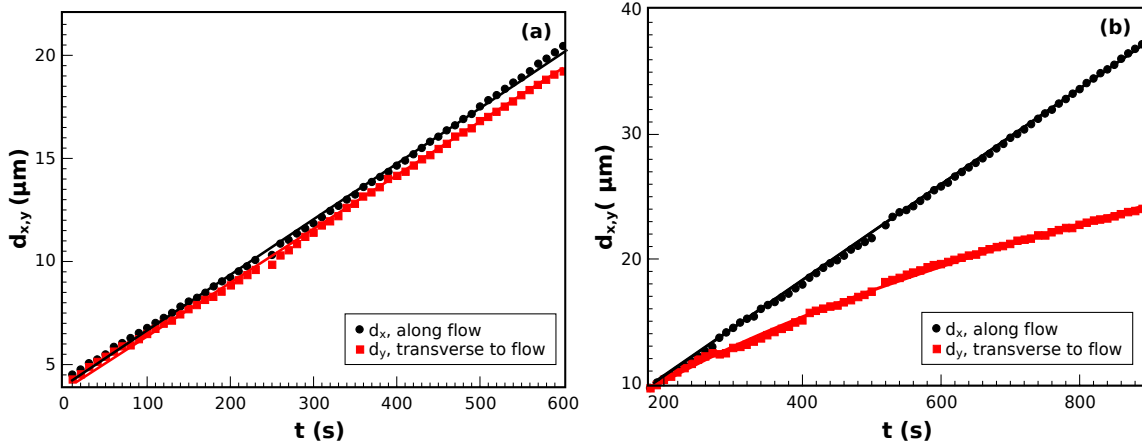


Figure 6.15: Typical profile of a particle growing along (black cycles) and transverse (red squares) to the direction of flow at  $R = 10$  when  $[\text{PO}_4^{3-}] = 0.075 \text{ M}$ :  $q_v = 0.2 \mu\text{L}/\text{min}$  (a), and  $q_v = 3 \mu\text{L}/\text{min}$  (b).

to the flow (Fig. 6.15 (b)). This difference in growth rate led to the distortion in the shape of the particle to form the obovate structures (Fig. 6.14).

At lower injection rates the longer residence time of the ions in the channel offered by the slow velocity of the reacting ions distributes the supersaturation evenly in both directions. The diffusion rate transverse to the direction of flow increases and equals the reaction rate along the direction of flow, making it possible for a circular structure to develop. The pressure exerted on the growing polycrystalline material is low, reducing the possibility of impacting its shape. On the other hand, when the injection rate is high, the reaction rate along the flow becomes greater than the diffusion rate transverse to flow. When the diffusion is not sufficient, the reactant ions tend to be continuously washed away reducing the mixing caused by diffusion, hence a distortion in the shape of the polycrystal appears. The high pressure due to the high injection rates also causes the asymmetric distortion giving rise to a pointy end seen in Fig. 6.14 when  $q_v$  is  $5 \mu\text{L}/\text{min}$ .

We investigated the effect of supersaturation by varying the initial concentration of reactants at  $R = 6$ , for three injection rates ( $1.0$ ,  $3.0$ , and  $5.0 \mu\text{L}/\text{min}$ ), since we know that the growth rate is not affected to a great extent by the injection rate and that the growth of the polycrystal along the direction of flow is reaction-controlled. With a higher number of ions in solution, the probability and frequency of collision increases, resulting in a faster growth rate. For a full characterization we have plotted in Fig. 6.16 from the origin the growth rates as a function of the concentrations as

$$r_x \propto [\text{PO}_4^{3-}] \quad (6.25)$$

$$r_x \propto [\text{Li}^+][\text{PO}_4^{3-}] \quad (6.26)$$

$$r_x \propto [\text{Li}^+]^2[\text{PO}_4^{3-}] \quad (6.27)$$

$$r_x \propto [\text{Li}^+]^3[\text{PO}_4^{3-}] \quad (6.28)$$

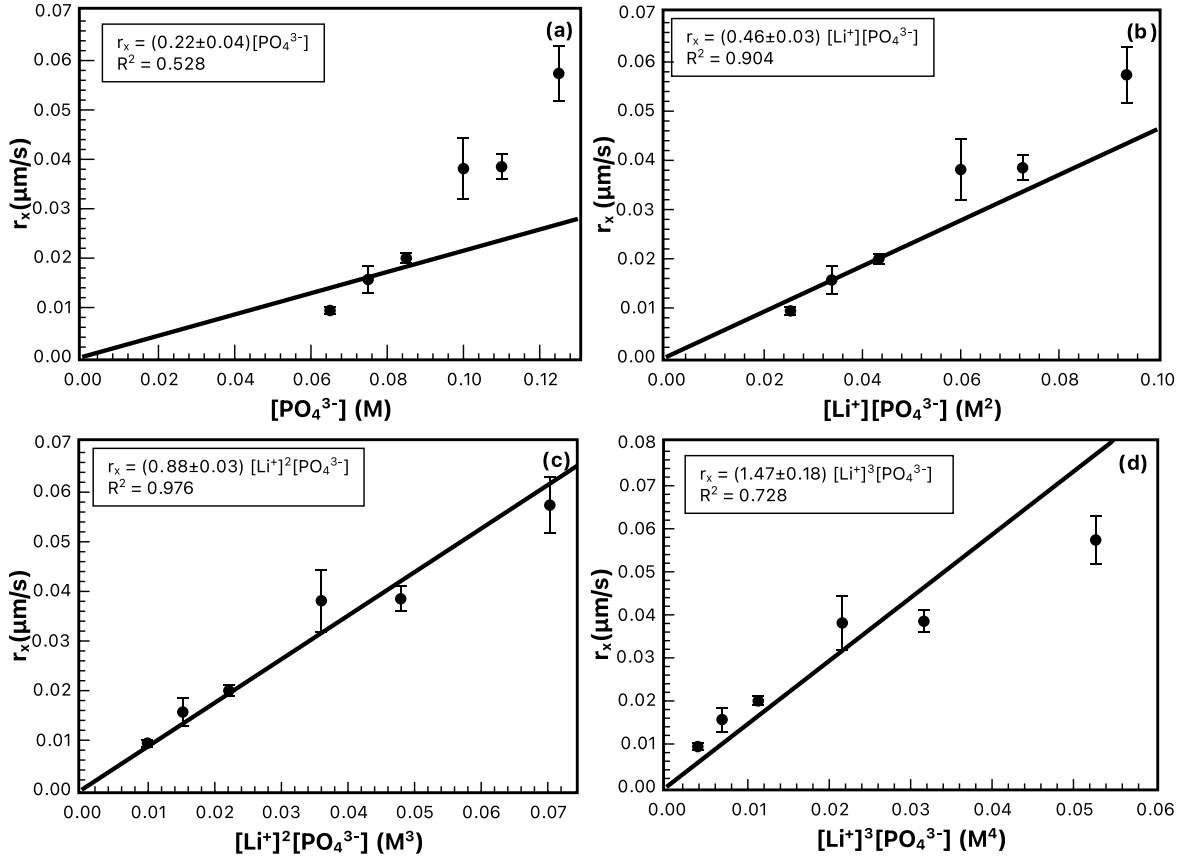


Figure 6.16: Growth rate along the direction of flow,  $r_x$  as a function of concentrations, at  $R = 6$ , for different rate laws with their linear fitting.

Comparing the fittings in Fig. 6.16, we can eliminate rate expressions of Eqns. 6.25, 6.26, and 6.28 because they do not represent a good fit to the experimental data. The fitting in Fig. 6.16 (c), on the other hand, shows the best agreement to the experimental data with  $R^2 = 0.976$ . This suggests that fast formation of  $\text{Li}_2\text{PO}_4^-$  complex takes place prior to the rate determining step in the growth. Therefore the proportionality represented by Eqn. 6.27 is the rate equation for the growth of lithium phosphate polycrystal in microfluidic system with a rate constant of  $(0.88 \pm 0.03) \mu\text{m s}^{-1} \text{M}^{-3}$ . To support this finding, we plotted the logarithm of the growth rate as a function of the logarithm of the concentration of the limiting reactant. The growth order  $\eta$  obtained from the fitting according to

$$\log r_x = \eta \log [\text{PO}_4^{3-}] + \beta, \quad (6.29)$$

is  $2.71 \pm 0.16$  as presented in Fig. 6.17, hence, affirming the rate law expression.

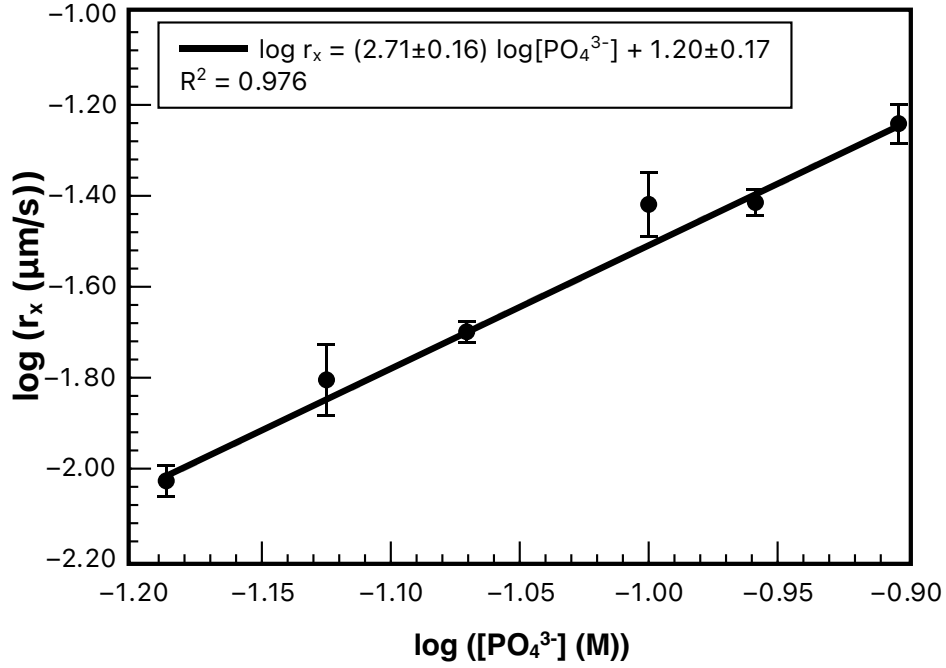


Figure 6.17: Growth rate along the direction of flow,  $r_x$  as a function of concentrations, at  $R = 6$ , for the determination of reaction order  $\eta$ .

### 6.3.1 Modeling of the concentration field in the microchannel

The flow in the reactor is laminar as indicated by the Reynolds number in the range of 0.09–0.36, calculated according to

$$Re = \frac{u_x d_H}{\nu} = \frac{2q_v}{(w+h)\nu} \quad (6.30)$$

where the hydraulic diameter ( $d_H$ ) for the microfluidic reactor is defined as  $d_H = \frac{2wh}{w+h}$  and kinematic viscosity  $\nu$  of the water as dilute solutions are involved. The Péclet number ( $Pe$ ), that is associated with the ratio of advective transport rate to that of diffusive is defined as

$$Pe = \frac{u_x L_x}{D} \quad (6.31)$$

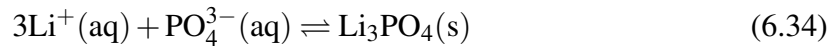
where the characteristic length scale ( $L_x$ ) is 1 mm. In the direction of flow  $Pe = 450 - 1800$ , therefore the diffusional contribution to transport along the  $x$ -axis is negligible. In the transverse direction, however, diffusion is the main form of transport with negligible advective contribution, hence Fick's second law can describe the evolution of concentration along the  $y$ -axis prior to nucleation. The input flow builds up a stationary concentration profile where the coordinate along the flow ( $x$ ) expresses the mixing or residence time between the two liquids as  $t = x/u_x$ . Since the input solutions are homogeneous, an analytical solution exists for the concentration profiles with diffusion along the  $y$ -axis and advection along the  $x$ -axis

according to

$$[\text{Li}^+] = \frac{[\text{Li}^+]_0}{2} \left[ 1 + \operatorname{erf} \left( \frac{y}{2\sqrt{x}D/u_x} \right) \right] \quad (6.32)$$

$$[\text{PO}_4^{3-}] = \frac{[\text{PO}_4^{3-}]_0}{2} \left[ 1 + \operatorname{erf} \left( \frac{-y}{2\sqrt{x}D/u_x} \right) \right] \quad (6.33)$$

where  $D$  is the diffusion coefficient of ions, approximated to be  $2000 \mu\text{m}^2/\text{s}$  for dilute aqueous solutions. For the reaction



it results in a stationary reaction quotient  $Q = [\text{Li}^+]^3[\text{PO}_4^{3-}]$ , that defines a zone of supersaturation along the contact line, as shown in Fig. 6.18 for  $R = 6$ .

The line of maximum supersaturation is located on the side of lithium input because of the greater exponent of lithium in the reaction quotient. The increase in the maximum value is in the order of a few percent within the observation window, therefore nucleation along this line can occur anywhere with approximately the same probability.

By considering the spatial distribution of the supersaturation the growth rate of precipitate particles can be rationalized. In the vicinity of the contact line, the vertical  $xz$ -plane is characterized by an almost constant supersaturation, hence the growth rate of isolated particles ( $r_x$ ) along the flow remains constant. Transverse growth on the other hand encounters a significant lowering of supersaturation, therefore the growth rate decreases in time. The scaling exponent is greater than 0.5, which indicates that the fresh reactants are transported by advective transport besides diffusion to the surface of the precipitate particles.

For a more accurate simulation to describe the spatial distribution of the precipitate particles at the time of nucleation, the density difference between the injected liquids has to be considered as well. Although in the experimental conditions the density of the reactant solutions,  $1.0153 \text{ g/cm}^3$  for the  $0.1 \text{ M Na}_3\text{PO}_4$  and  $1.0111 \text{ g/cm}^3$  for the  $0.6 \text{ M LiCl}$ , are comparable, weak buoyant forces can arise in the  $yz$ -plane transverse to the main flow. This additional fluid motion will further increase the asymmetry in the spatial distribution of precipitate particles sedimented in the microfluidic reactor.

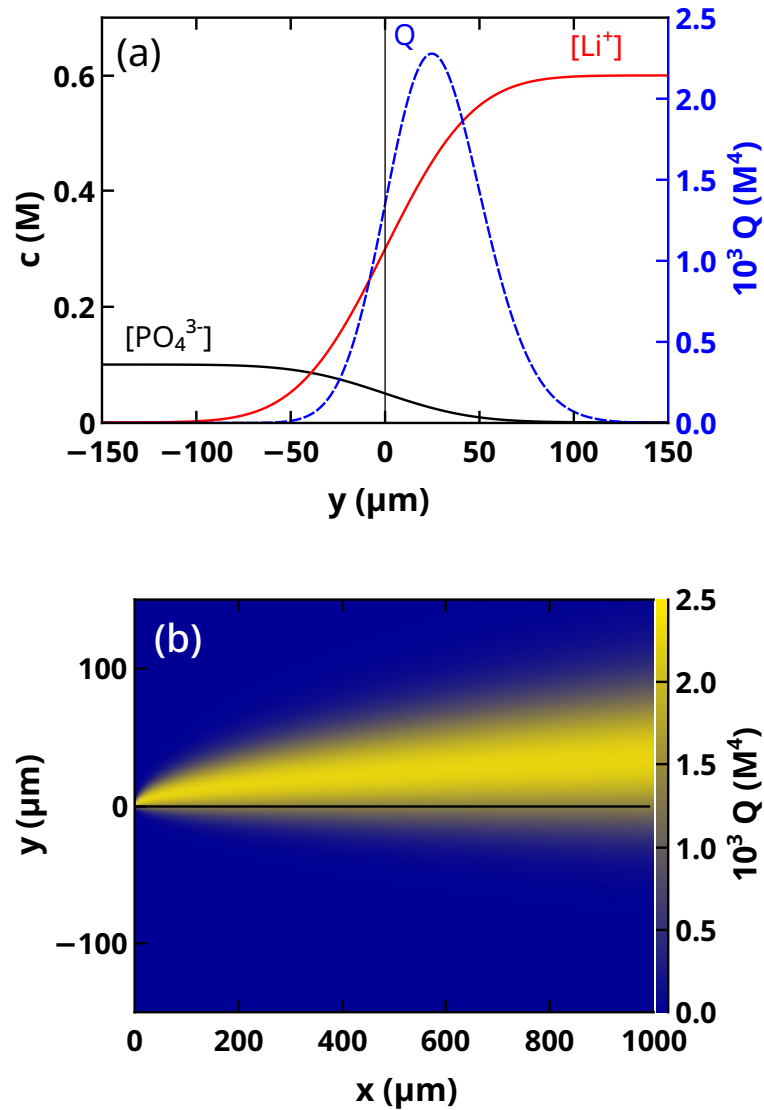


Figure 6.18: Stationary concentration profiles of reactants (solid lines) and the reaction quotient (dashed line) at position  $x = 500 \mu\text{m}$  with  $R = 6$  and  $[\text{PO}_4^{3-}] = 0.1 \text{ M}$  (a). Spatial distribution of reactant quotient  $Q$ , characterizing the supersaturation in the view area (b).

### 6.3.2 Microstructure of lithium phosphate from microchannels

The morphology visualized by SEM images of the particles from the well-stirred experiment (reference) and the microchannels appear similar (see Fig. 6.19), spherical particles with the spherulite-like structure are formed that consist of small rod-like crystallites of about  $1\text{--}2 \mu\text{m}$  in size. Besides the crystallites, amorphous particles are also observable.

From the diffractograms in Fig. 6.20, it was identified that the crystals are the orthorombic, low form of lithium phosphate [198]. The X-ray diffraction data also indicate that the lithium phosphate obtained from both the microchannel and the well-stirred reference system belong to the same space group of  $\text{Pmn}2_1$  (orthorombic) [198] which corresponds to the  $\beta\text{-Li}_3\text{PO}_4$  prepared mostly from wet chemical reaction (see Fig. 6.10) [203], with corner-

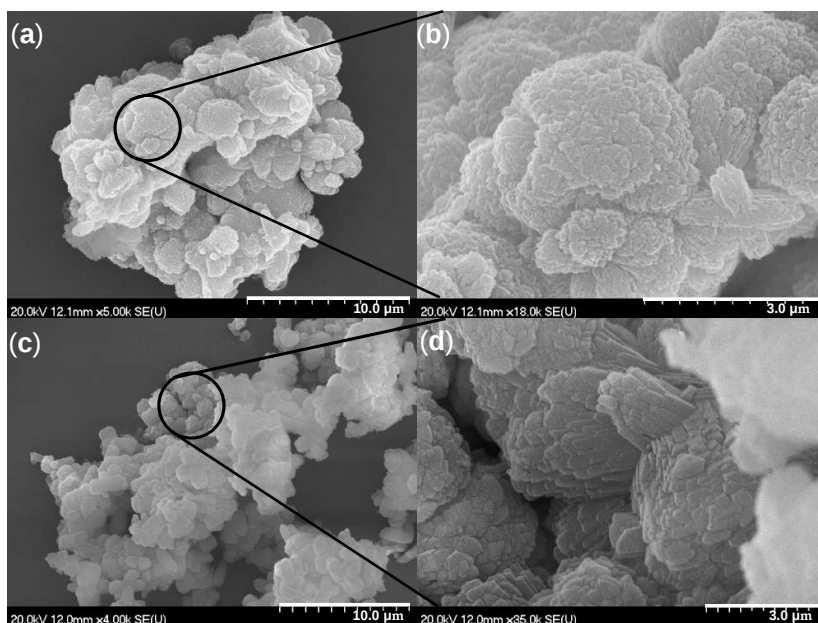


Figure 6.19: SEM images of precipitate particles (a) from a well-stirred system with (b) an enlargement and (c) from the microchannel with (d) an enlargement for  $R = 6$ .

sharing tetrahedra pointing towards the same direction along the  $c$  main axis [204, 205]. Crystallinity of the samples is  $\sim 67\%$  from both the reference and the microfluidic system within the experimental error. The average size of the crystallites comprising the polycrystalline aggregates calculated from the Scherrer equation, Eqn. 5.1, is  $183 \text{ \AA}$  and  $233 \text{ \AA}$  in the well-stirred and in the microfluidic system, respectively, indicating that microfluidics offers a simple possibility to increase the crystallite size in a controlled manner.

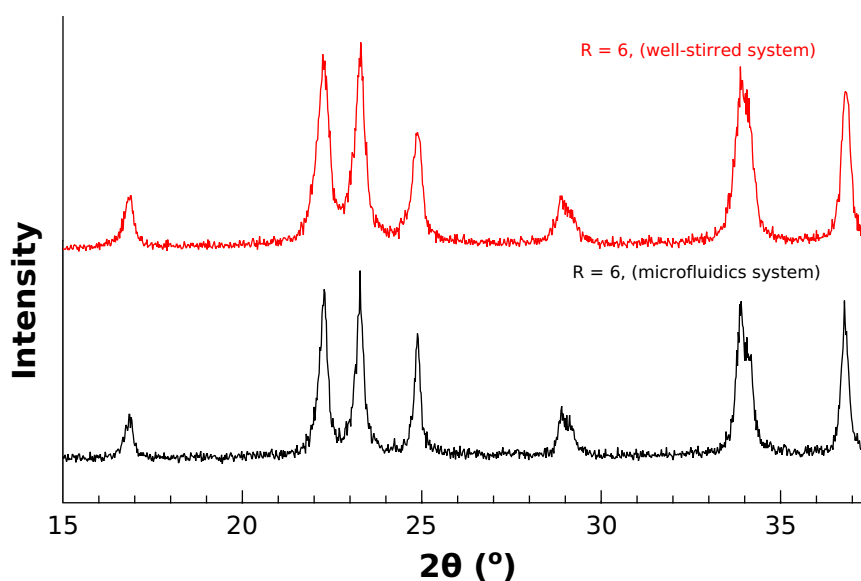


Figure 6.20: X-ray diffractograms of samples from microfluidic experiments (black line), and from well-stirred experiments (red line), at room temperature with  $R = 6$ .

## 6.4 3D temporal evolution of precipitate structure

In preliminary experiments, we placed a pellet made from LiCl into a 0.6 M  $\text{Na}_3\text{PO}_4$  solution and allowed to stand for 3 hours (Fig. 6.21(a)). The dissolution of the LiCl in the  $\text{Na}_3\text{PO}_4$  solution led to the formation of a pH gradient as osmosis continuously forces the  $\text{Na}_3\text{PO}_4$  solution into the pellet causing the formation of a  $\text{Li}_3\text{PO}_4$  precipitate membrane and, hence, an upward elongation forming strands of precipitate structures. Although this method provides qualitative data for the formation of the  $\text{Li}_3\text{PO}_4$  chemical garden structures, it lacks consistency in providing quantitative data since the number of tubes cannot be predicted or controlled from one experiment to the other.

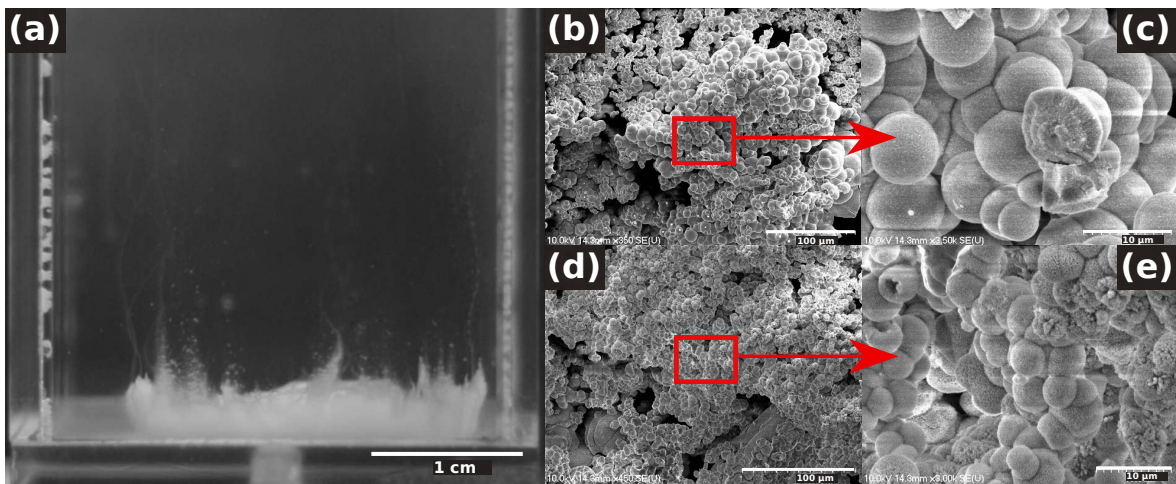


Figure 6.21: Lithium phosphate chemical garden obtained from a pellet of LiCl placed in a 0.6 M  $\text{Na}_3\text{PO}_4$  solution (a), SEM image of the outer surface of the precipitate strand (b,c), and the inner one (d,e).

Upon the injection of LiCl solution into the stagnant solution of  $\text{Na}_3\text{PO}_4$  from below, corresponding to the classical chemical garden scenario, a thin vertical jet reaching the liquid surface arises. The momentum of the injected liquid dominates the fluid motion at these flow rates because buoyant forces remain weak due to the small density difference between the two solutions ( $\rho_{\text{LiCl}} = 1.1283 \text{ g/cm}^3$  and  $\rho_{\text{Na}_3\text{PO}_4} = 1.1041 \text{ g/cm}^3$ ). The small precipitate particles forming around the perimeter of the jet make it clearly visible, however, they travel with the flow and no contiguous structure is being built. Instead, close to the upper liquid surface larger flakes of lithium phosphate appear that later sink to the bottom due to their greater density. In the reverse configuration, when the solution of sodium phosphate is injected into the LiCl solution, the previously described processes are significantly less pronounced. Here, following the formation of the jet, the steady growth of a precipitate structure around it is observed that creates a vertical column (see Fig. 6.22(a)).

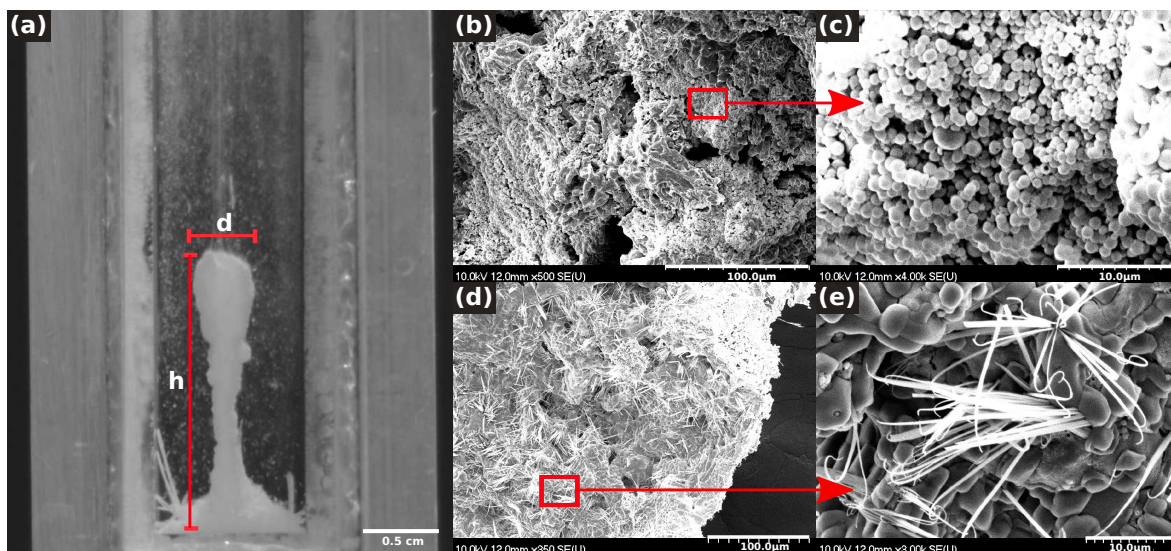


Figure 6.22: Lithium phosphate chemical garden obtained by injecting 0.6 M  $\text{Na}_3\text{PO}_4$  solution into 6.0 M  $\text{LiCl}$  solution (a), SEM image of the outer surface of the tube (b,c), and the inner one (d,e).

The architecture initially, continuously builds upward until a maximum height is reached when the vertical only growth almost stops (Fig. 6.23), while the diameter of the tubular structure further increases, especially in the vicinity of the tip.

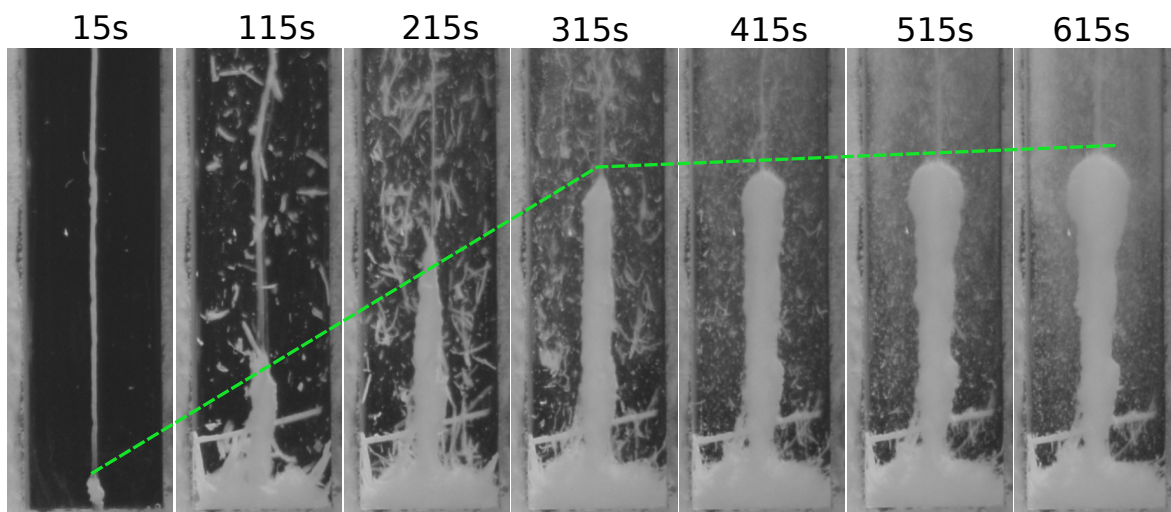


Figure 6.23: Lithium phosphate chemical garden showing the evolution in height of the precipitate structure. The green broken line indicates a typical profile.

The resultant precipitate tube is sufficiently rigid so that it can easily be removed from the solution, then dried, and used for SEM analysis. The microstructures of the inner and the outer surfaces of the tube are shown in Fig. 6.22(b-e). The outer parts of the structure are comprised of nano spherical crystals with rough a surface (Fig. 6.22(b,c)), while the inner surface has filled spheres with hairy crystals (Fig. 6.22(d,e)). The observed difference in

morphology is a result of the presence of concentration gradients that maintains a distinct chemical environment on the opposite sides; common characteristics of tubular precipitate assemblies in chemical gardens [206, 207]. On the other hand, when the precipitate from the pellet experiment was collected and observed under a SEM, both the inner and outer parts of the tube comprises of nanospheres with smooth surfaces. The outer part is similar to that obtained from liquid–liquid system, whereas the inner parts differ. The hairy crystals are seen in Fig. 6.22(d,e) are not seen in the inner portion of the precipitate structure from pellets. The similarity in the microstructure of the crystals from the pellet experiment is due to the fact that there is no significant flow, hence, very little or no concentration gradients are generated.

The tube dimensions can be generally characterized by the height and diameter, and from the temporal evolution of these data, the linear and volume growth rate can be determined. The tube height increases linearly as time progresses up to a certain height as illustrated in Fig. 6.23 and 6.24(a) for several flow rates. The initial steady growth is independent of the injection rate. The linear growth rate, determined from the slope of the vertical growth before attaining maximum height, is  $u_1 = 74.0 \pm 0.6 \mu\text{m/s}$  which is significantly smaller than the fluid jet velocity that is in the range of 200-1000  $\mu\text{m/s}$ . The vertical growth rate suddenly drops significantly, hence the maximum height  $h_{max}$ , reached by the initial evolution at  $t_{max}$  is defined by the intersection of the two growth regimes.

With our selected injection rates, the height reached during the first stage is independent of the width of the container, i.e., the return bulk flow has a negligible contribution. In addition, the solution height of the originally stagnant fluid has to be sufficiently large so that the tip does not come into the vicinity of the liquid surface. The growth rate in the second stage is also independent of the injection rate with  $u_2 = 2.86 \pm 0.33 \mu\text{m/s}$ , therefore a universal growth profile can be constructed for all the measurements where height is scaled to the maximum height reached by the precipitate structure during the first stage. By plotting the dimensionless height, defined as  $H = h/h_{max}$ , as a function of the dimensionless time, with  $\tau = t/t_{max}$ , the data merges onto a single curve (Fig. 6.24(b)) with

$$H = \begin{cases} \tau & \tau \leq 1 \\ 1 + \frac{u_2}{u_1}(\tau - 1) & \tau > 1 \end{cases} \quad (6.35)$$

for all the investigated injection rates, where  $u_2/u_1$  is the ratio of the linear growth rates in the two regimes [208]. Furthermore, there is a linear relationship between the injection rate  $q_v$  and both the maximum height  $h_{max}$  and the time required to reach that height  $t_{max}$ , as illustrated in Fig. 6.25.

The presence of a gradual diffusive reduction in the pH of the jet as it advances, together with a critical pH below which precipitation stops, leads to the saturation in the height of the precipitate structure [144, 174, 207]. The ratio of the slopes from Fig. 6.25, highlights the

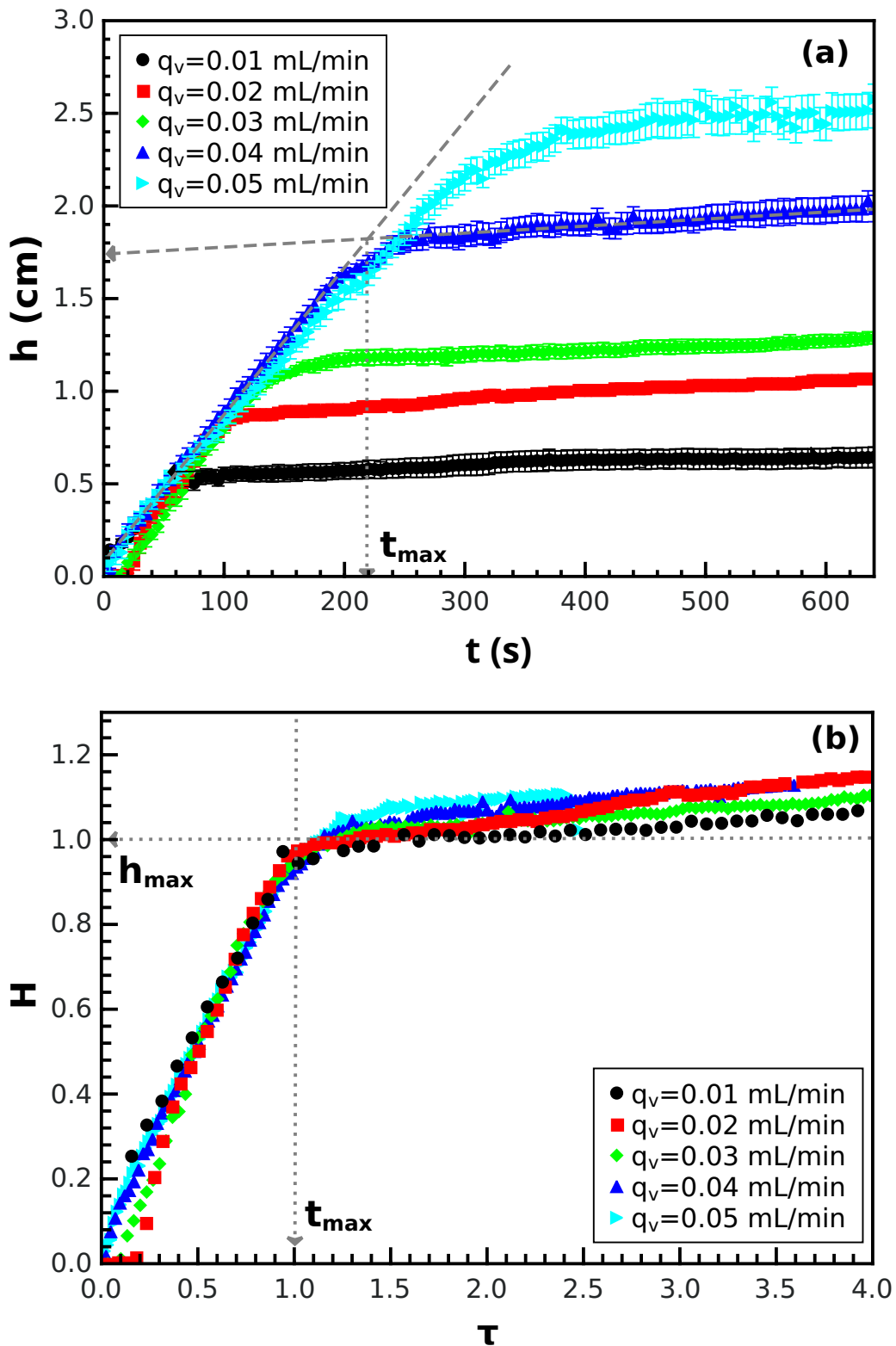


Figure 6.24: Growth profile of the precipitate structure at different injection rates giving a constant linear growth before reaching maximum height (a) and dimensionless height  $H$ , as a function of dimensionless time  $\tau$  (b). The dashed lines correspond to the dotted lines while the dotted lines aid the eye.

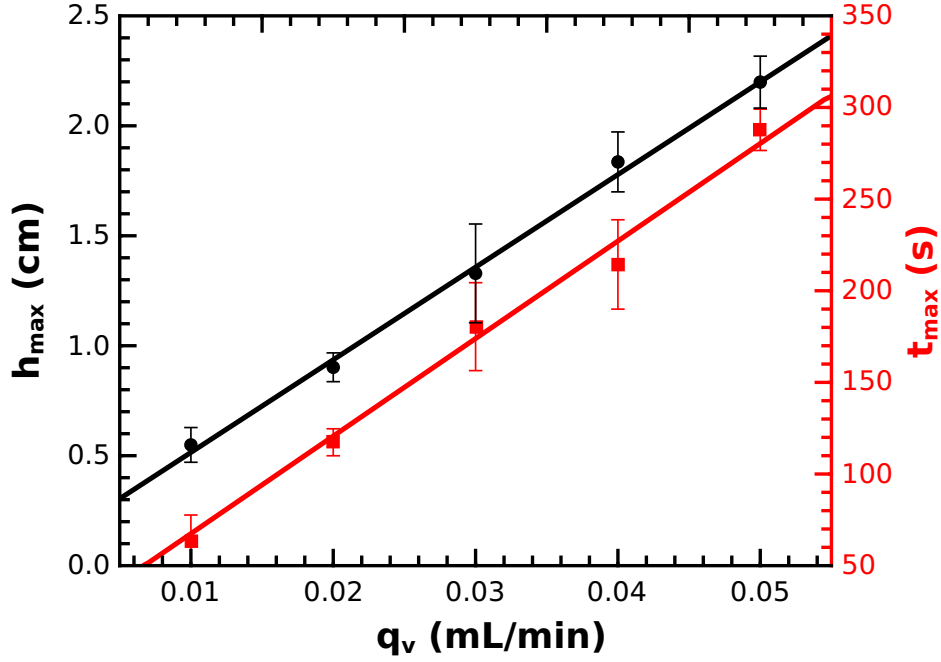


Figure 6.25: The maximum height maximum height reached by a growing chemical garden  $h_{max}$  and the corresponding time  $t_{max}$  as a function of injection rate the injection or flow rate  $q_v$ , with their corresponding fitting.

inherent linear growth rate of  $75 \pm 8 \mu\text{m/s}$ .

In a similar vein, to determine the volume of the tube, we first converted the images into binary form, then found the centroid, i.e., the center of mass. We divided the image vertically through its center of mass and measured the radius of rotation at the height of the centroid ( $R_s$ ). Because the structure can be approximated by symmetric solid of revolution, [209] the volume was calculated following Pappus 2<sup>nd</sup> centroid theorem

$$V = 2\pi A_{1/2} R_s \quad (6.36)$$

with  $A_{1/2}$ , being the area of half cross-section of the structure divided through its centroid. From the area of the half structure and  $R_s$ , we calculated the volume using Eqn. 6.36. The obtained volume increases with time in the manner depicted in Fig. 6.26(a). The volume growth rate depends on the injection rate, but in a single experiment it remains constant even when the growth characteristics change at  $t = t_{max}$ . Even though the extension in height of the structure follows two growth regimes, the volume of the entire material remains constant and increases linearly with time. Upon comparing it with the injection rate, (see Fig. 6.26(b)) a linear relation is revealed with a slope of  $0.55 \pm 0.05$ . This implies that the precipitate tube does not form a closed structure, the injected solution can leak out through the porous membrane into the external solution or through any opening, mostly at the tip of the tube.

Once this growing precipitate structure reaches a maximum height, the diameter at the

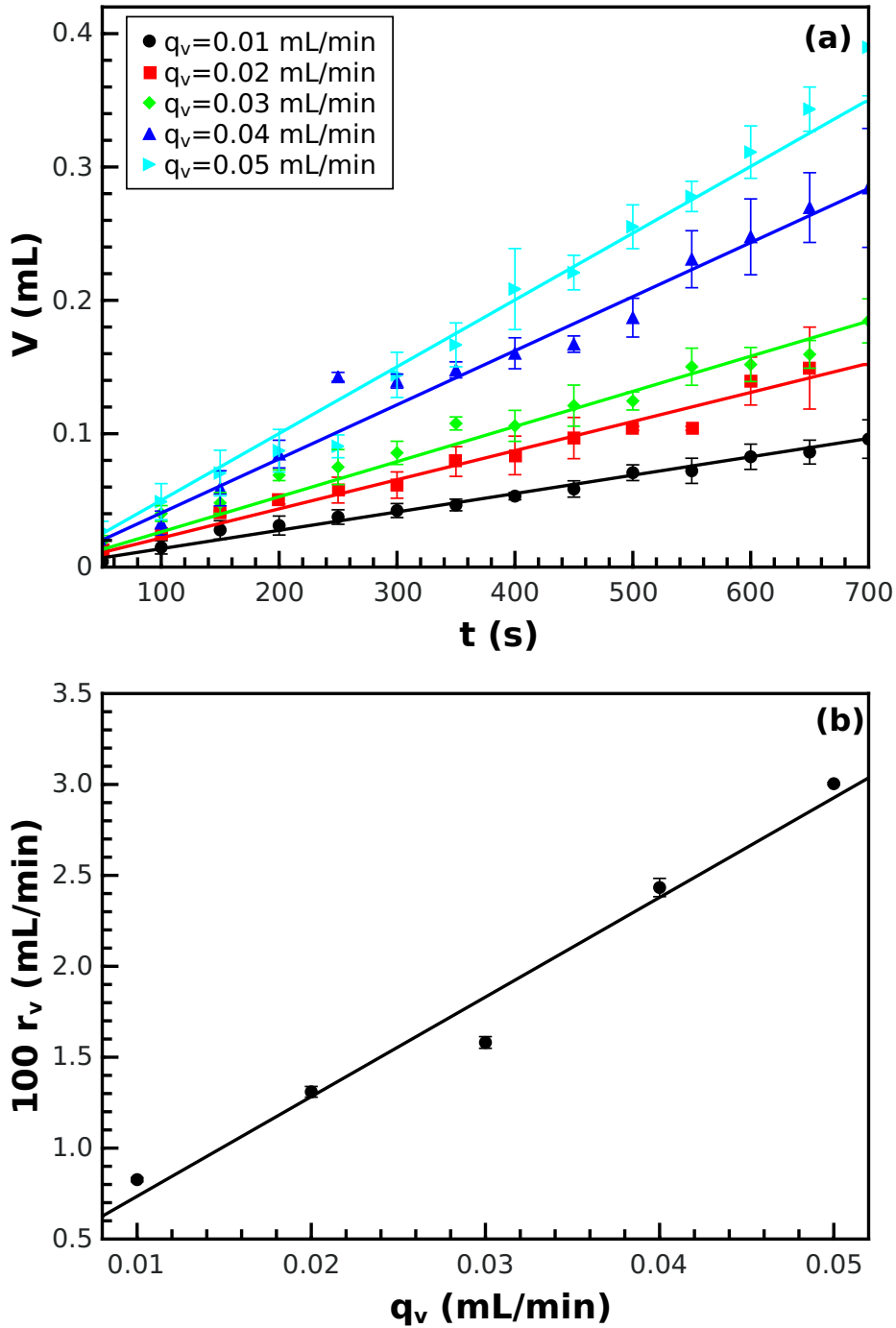


Figure 6.26: Temporal evolution of the precipitate volume for various injection rates (a), volume growth rate  $r_v$  as a function of injection rate  $q_v$  (b).

tip (Fig. 6.27) begins to increase. This expansion follows a simple power law function

$$\Delta d = (d - d_0) = k (t - t_0)^\eta \quad (6.37)$$

where  $d$  is the diameter at any time  $t$ ,  $d_0$  is the initial diameter at the time vertical growth stopped  $t_0 = t_{max}$ ,  $k$  is a proportionality constant, and  $\eta$  is the growth order. By fitting the

curves in Fig. 6.27 to Eqn. 6.37, we obtain  $\eta = 0.75 \pm 0.01$  and  $k = (3.12 \pm 0.03) \times 10^{-3} \text{ cm/s}^\eta$ . Since the exponent is greater than 0.5, convection plays a role in the structure formation besides diffusion.

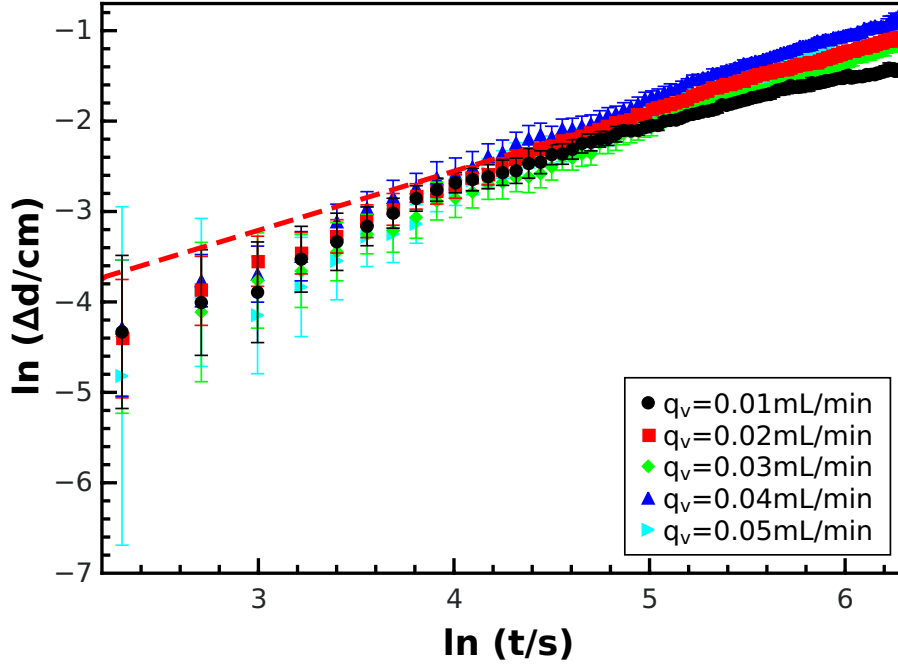


Figure 6.27: Temporal change in the tip diameter of the precipitate after  $h_{max}$  was reached.

The flow characteristics are determined from the Reynolds number defined as

$$Re = \frac{4 q_v}{\pi v_i d} \quad (6.38)$$

where  $q_v$  is the injection rate,  $v_i = 0.0322 \text{ cm}^2/\text{s}$  is the kinematic viscosity of the injected solution, and  $d = 0.04 \text{ cm}$  is the inlet diameter. In our experiments, the flow is laminar with  $0.08 < Re < 0.4$ , which can maintain the steady elongation of the tubular structure in the first growth regime driven by convective transport.

# Chapter 7

## Summary

Several steps are involved in the precipitation of materials from solution, and there are numerous methods to study its kinetics. These precipitation steps include nucleation, growth, and sometimes aggregation. We employed the well-stirred system of a small solution volume to study the kinetics of  $\text{Li}_3\text{PO}_4$  nucleation by measuring the turbidity of the stirred solution as a function of time using a UV-visible spectrophotometer. We also studied the growth of  $\text{Li}_3\text{PO}_4$  in a quasi 2-dimensional microfluidic system by measuring the change in the diameter of the polycrystalline precipitate material formed in the microchannel. Lastly, we investigated the growth of  $\text{Li}_3\text{PO}_4$  in a 3-dimensional chemical garden system, by measuring the change in the height and volume of the precipitate material formed.

We carried out a numerical speciation calculation to determine the relative amount of species in the solution at different pH ranges. At  $11 < \text{pH} < 12$ , the precipitate is dominantly  $\text{Li}_3\text{PO}_4$  with a negligible amount of  $\text{LiOH}$ . This enabled us to use the tribasic sodium phosphate, the solution of which has a pH of 12 for maximum precipitate yield. The minimum pH for the appearance of lithium phosphate precipitate decreases as the reactant ratios increase. The relative percentages of the lithium ion consumed also decrease as the reactant ratio increases.

We then studied the precipitation of  $\text{Li}_3\text{PO}_4$  in a well-stirred system by stirring an equal volume of  $\text{LiCl}$  and  $\text{Na}_3\text{PO}_4$  solutions with a stoichiometric ratio in a thermostated UV-visible spectrophotometer. From the turbidity-time profiles we determined the induction times for the precipitation. The induction time, which is inversely proportional to the nucleation rate, was used to calculate nucleation parameters. Results from the power law fitting of a plot of induction time as a function of reactant concentration gave a fourth order for the nucleation of  $\text{Li}_3\text{PO}_4$ , which is in accordance with the predictions of the law of mass action kinetics. Classical nucleation theory revealed that the formation of  $\text{Li}_3\text{PO}_4$  follows a homogeneous pathway involving only the ions in solution with no or negligible foreign surface interference. The interfacial tension was calculated, having values consistent with values predicted by the Mersmann equation[197]. The value of  $\gamma$  for  $\text{Li}_3\text{PO}_4$  is higher than those for  $\text{CaCO}_3$  and  $\text{SrCO}_3$  indicating lower solubility of the  $\text{Li}_3\text{PO}_4$  precipitates [194].

Increasing the temperature affects the precipitation of  $\text{Li}_3\text{PO}_4$  and even the microstructure. We fixed the supersaturation of the reactant solutions and varied the temperature from 25–50 °C. An Arrhenius-type equation was employed on the induction times determined to calculate the activation energy for the nucleation process under the working conditions. The apparent activation energy at temperatures above 35 °C has a value about half of that obtained at lower temperatures, suggesting that the rate determining step follows reactions with different activation energies. At 25 °C, the crystals formed are mostly amorphous with smaller crystallite size. The size of the crystals increases with temperature and the aggregation of the crystals at a longer precipitation time causes a lowering in the crystallinity at 50 °C, as obtained from XRD.

In order to study the growth kinetics of lithium phosphate, we employed a microfluidic system, where we injected solutions of  $\text{LiCl}$  and  $\text{Na}_3\text{PO}_4$  into a microchannel from two inlets. At a stoichiometric concentration of reactants, many nucleation sites and small sizes of rhombohedral  $\text{Li}_3\text{PO}_4$  crystals are formed, thus, this reaction condition does not provide adequate data for the study of crystal growth. We then increased the ratio of the reactants with  $\text{Li}^+$  having a concentration 6 times that of  $\text{PO}_4^{3-}$ . We observed the formation of well-spaced polycrystalline particles along the contact line of the two reacting solutions. We varied the injection rates, the channel size, and also the ratio of the reactant concentrations always keeping the concentration of  $\text{Li}^+$  higher than in a stoichiometric ratio of the reactants. Analysis of the growth profile revealed that along the direction of flow, the polycrystalline material grows linearly with time and shows no dependence on the injection rate for a reactant ratio of 6. On the other hand, transverse to the direction of flow, particle growth is slower and follows a power law. The exponent in the power law has a value greater than 0.5, indicating that both diffusive and advective forces play a role in the growth of the particle in this direction. Lowering the concentration of the reactants and maintaining the ratio of 6:1, the growth rate of the particle along the flow dropped from  $\approx 0.032 \mu\text{m/s}$  to  $0.014 \mu\text{m/s}$ . Thus, the supersaturation of the reacting species plays a part in the growth of the polycrystalline particles. At a constant injection rate the use of higher ratios results in faster growth along the direction of the flow, while the transverse growth remains constant.

The shape of the particle formed depends on the injection speed. We observed a gradual transformation of the shape of the polycrystalline particle in the microchannel from a circular to an obovate as the injection rate is increased. This is a result of the increased residence time set by the low injection rate making it possible for the supersaturation to be distributed evenly along and transverse to the directions of flow.

With negligible advective forces acting transverse to the direction of flow, we used Fick's  $2^{\text{nd}}$  diffusion law to model the concentration along this direction. This describes the evolution of concentration along the  $y$ -axis prior to nucleation, building up a stationary concentration profile. The maximum supersaturation is located on the side containing  $\text{Li}^+$  due to its greater exponent in the reaction quotient.

We reported for the first time the formation of a chemical garden from an alkali metal. By injecting a solution of LiCl into a solution of Na<sub>3</sub>PO<sub>4</sub> in a cuvette, we were able to study the formation and growth of Li<sub>3</sub>PO<sub>4</sub> chemical garden or hydrothermal vent-type structure. We analyzed the growth in the height and volume of the structure as a function of time. The structure first evolves linearly in height at a fast rate until a maximum height is reached, then this growth slows down significantly and the structure begins to expand at the tip. This initial growth rate is constant, regardless of the injection rate, but the maximum height depends linearly on it. The volume of the structure is proportional to the time of injection throughout the experiment. The volume increases as the injection rate with slopes of the volume-time plot giving a value consistently lower than the injection rate under investigation. This indicates that the structure is porous and Li<sup>+</sup> flows through this membrane or the opening at the tip into the bulk solution of the sodium phosphate. The growth at the tip of the structure after the maximum height is reached was also characterized, which follows a simple power law having an exponent of 0.75, suggesting the contribution of both advection and diffusion to the growth along this direction.

This research provides a better understanding of the nucleation of lithium phosphate and, hence, makes lithium recovery from different sources, especially from brine and used lithium ion batteries, easier in future applications. The microfluidic system serves as a model technique for investigating the crystal growth of other useful salts. We reported for the first time the formation of a chemical garden from an alkali metal. The chemical gardens used to be thought of as silicates of transition metals and other alkaline–earth metals. Our study has opened a door to the exploitation of the behaviours of chemical gardens from other simple precipitating systems. Important applications of the lithium phosphate chemical garden that should be investigated in the future are catalysis and the synthesis of gradient composites.

# Glossary

<i>A</i>	kinetic parameter in the equation of classical nucleation theory
<i>A'</i>	prefactor when $t_{ind} = (JV)^{-1}$
$A_{1/2}$	cross-sectional area of half of a symmetrical chemical garden structure
<i>B</i>	thermodynamic parameter in in the equation of classical nucleation theory
<i>D</i>	diffusion constant
<i>L</i>	conductance
<i>H</i>	dimensionless height
<i>J</i>	nucleation rate
<i>PDI</i>	polydispersity index
<i>Pe</i>	Péclet number
<i>Q</i>	reactant quotient
<i>R</i>	ratio of reactants concentration
$R_s$	shortest distance from the centroid of a chemical garden structure
<i>Re</i>	Reynolds number
<i>S</i>	supersaturation
<i>T</i>	absolute temperature
<i>V</i>	molecular volume
$E_a$	apparent activation energy
$M_w$	molecular weight
$N_A$	Avogadro constant
$K_{sp}$	solubility product
<i>ACC</i>	amorphous calcium carbonate
<i>CNT</i>	classical nucleation theory
<i>SEM</i>	scanning electron microscopy
<i>XRD</i>	X-ray diffraction

$\Delta G$	total excess free energy
$\Delta G_s$	surface excess free energy
$\Delta G_v$	volume excess free energy
$\Delta G_{crit}$	maximum free energy
$\Delta g_v$	the free energy change of the transformation per unit volume
$\mu$	chemical potential
$\gamma$	interfacial energy between the surface of a nuclei and the solute in solution
$\gamma_{SL}$	estimated interfacial tension between a particle surface and solute in solution
$\lambda_i$	limiting ionic conductivity
$\tau$	dimensionless time
$a'$	aparent rate constant
$b$	reaction order
$h$	height of a chemical garden at any time
$h_{max}$	maximum height reached by a growing chemical garden
$t_{max}$	time it takes a growing chemical garden to reach a maximum height
$k_b$	Boltzmann constant
$PDI$	polydispersity index
$q_v$	injection or flow rate
$r$	radius of a crystal nucleus
$r_c$	radius of a critical nucleus at maximum free energy
$r_x$	growth rate of a particle along the direction of flow in a microchannel
$r_v$	volume growth rate of a chemical garden structure
$u_1$	growth rate of a chemical garden in the first regime
$u_2$	growth rate of a chemical garden in the second regime
$\rho_c$	density of a crystal
$t_g$	the time required for a nuclei to grow from the critical size to a detectable crystal
$t_n$	the time required for the formation of a critical nuclei
$t_r$	the time required for the system to achieve a quasi-steady-state cluster distribution
$t_{ind}$	induction time
$\nu$	kinematic viscosity
$y$	particle position in a microchannel transverse to flow
$a_i$	ionic activity
$f^*$	the collision frequency of the ions

$\rho_c$	density of crystal
$\nu$	kinematic viscosity
$y$	particle position in a microchannel transverse to flow
$a_i$	ionic activity
$f^*$	the collision frequency of the ions
$c_0$	the concentration of the active nucleation site
$z$	Zeldovich factor
$\kappa$	conductivity
$\mathcal{C}$	cell constant
$\mathcal{D}$	crystallite size
$\mathcal{H}$	Scherrer constant
$\lambda$	wavelength of X-ray beam
$\beta$	the full width at half maximum
$\theta$	Bragg angle
$m$	polycrystalline particle boundary with maximum intensity
$n$	polycrystalline particle boundary with minimum intensity
$I_x$	intensity of the particle measured under a selected horizontal line
$Q$	reactants quotient
$k$	proportionality constant
$\eta$	growth order
$C$	concentration of a solution
$d_H$	hydraulic diameter

# Bibliography

- [1] J.B. Goodenough and Y. Kim. Challenges for rechargeable li batteries. *Chemical Materials*, 22:587–603, 2010.
- [2] M. S Whittingham. Lithium batteries and cathode materials. *Chemical Reviews*, 104: 4271–4302, 2004.
- [3] Z. Wang, D Orejon, K. Sefiane, and Y. Takata. Water vapor uptake into hygroscopic lithium bromide desiccant droplets: mechanisms of droplet growth and spreading. *Phys.Chem.Chem.Phys.*, 21:1046–1058, 2019.
- [4] L. Hao, J. Wei, M. Weihua, Q. Hongxia, and Z. Qin. Catalytic performances of hollow  $\text{Li}_3\text{PO}_4$  spheres for propylene oxide isomerization. *Chemical Engineering Communications*, 203:339–344, 2016.
- [5] P. K. Alaboina, J.S. Cho, M.J. Uddin, and S.J. Cho. Mechanically prelithiated silicon nano alloy as highly engineered anode material. *Electrochimica Acta*, 258:623–630, 2017.
- [6] R. Oruch, M.A. Elderbi, H.A. Khattab, I.F. Pryme, and A. Lund. Lithium: A review of pharmacology, clinical uses, and toxicity. *European Journal of Pharmacology*, 740: 464–473, 2014.
- [7] A. Hal and V-S. Angelica. Toxicity of lithium to humans and the environment—a literature review. *Ecotoxicology and Environmental Safety*, 70, 2008.
- [8] L. Kavanagh, J. Keohane, G. Garcia-Cabellos, A. Lloyd, and J. Cleary. Global lithium sources—industrial use and future in the electric vehicle industry: A review. *Resources*, 7:57, 2018.
- [9] B. Shahzad, M. Tanveer, W. Hassan, A.N. Shah, S.A. Anjum, S.A. Cheema, and I. Ali. Lithium toxicity in plants: Reasons, mechanisms and remediation possibilities - a review. *Plant Physiology and Biochemistry*, 107:104–115, 2016.
- [10] J.A. Epstein, E.M. Feist, and J. Zmora. Extraction of lithium from the dead sea. *Hydrometallurgy*, 6:269–275, 1981.

- [11] C. Fouillac and G. Michard. Sodium/lithium ratio in water applied to geothermometry of geothermal reservoirs. *Geothermics*, 10, 1981.
- [12] H. Li, S. Xing, Y. Liu, F. Li, H. Guo, and G. Kuang. Recovery of lithium, iron, and phosphorus from spent lifepo4 batteries using stoichiometric sulfuric acid leaching system. *ACS Sustainable Chemistry & Engineering*, 5:8017–8024, 2017.
- [13] W. J Brian. Lithium. *Mineral Commodity Summaries*, 2020. URL <http://pubs.acs.org/books/references.shtml>.
- [14] B. Swain. Recovery and recycling of lithium: A review. *Separation and Purification Technology*, 172:388–403, 2017.
- [15] M. T. Buntaine. *Nicholas School of the Environment*. PhD thesis, Duke University, 2011.
- [16] W. Gao, X. Zhang, X. Zheng, X. Lin, H. Cao, Y. Zhang, and Z. Sun. Lithium carbonate recovery from cathode scrap of spent lithium-ion battery: a closed-loop process. *Environmental Science & Technology*, 51:1662–1669, 2017.
- [17] Y. Song, L. He, Z. Zhao, and X. Liu. Separation and recovery of lithium from  $\text{Li}_3\text{PO}_4$  leaching liquor using solvent extraction with saponified D2EHPA. *Separation and Purification Technology*, 229:115823, 2019.
- [18] X. Wang, X. Wang, R. Zhang, Y. Wang, and H. Shu. Hydrothermal preparation and performance of  $\text{LiFePO}_4$  by using  $\text{Li}_3\text{PO}_4$  recovered from spent cathode scraps as li source. *Waste Management*, 78:208–216, 2018.
- [19] S-J. Lee and J-T. Son.  $\text{LiOH} \cdot \text{H}_2\text{O}$  recovery from nickel-rich cathode materials using the novel vacuum heat treatment method. *Journal of the Korean Physical Society*, pages 1–4, 2021.
- [20] J. G. J. Olivier, J. A Van Aardenne, F. J Dentener, V Pagliari, L. N Ganzeveld, and J. AHW Peters. Recent trends in global greenhouse gas emissions: regional trends 1970–2000 and spatial distribution of key sources in 2000. *Environmental Sciences*, 2: 81–99, 2005.
- [21] D. Liu, X. Guo, and B. Xiao. What causes growth of global greenhouse gas emissions? evidence from 40 countries. *Science of The Total Environment*, 661:750–766, 2019.
- [22] J. G. J. Olivier, J. A. H. W. Peters, et al. *Trends in global  $\text{CO}_2$  and total greenhouse gas emissions: 2017 report*. PBL Netherlands Environmental Assessment Agency The Hague, 2017.

- [23] I. Arto and E. Dietzenbacher. Drivers of the growth in global greenhouse gas emissions. *Environmental science & technology*, 48:5388–5394, 2014.
- [24] L. J Martínez, C Charbuillet, S Pompidou, and N Perry. Recycling chains: a proposal for an exhaustive definition. *Communications Sans Acte*, 2016.
- [25] D. Bradley and B. Jaskula. Lithium—for harnessing renewable energy. *Fact Sheet 2014–3035*, page 2, 2014.
- [26] B. Jaskula. Lithium. *Mineral Commodity Summaries*, page 98, 2020.
- [27] P Greim, A. A Solomon, and C Breyer. Assessment of lithium criticality in the global energy transition and addressing policy gaps in transportation. *Nature Communications*, 11:1–11, 2020.
- [28] NS Energy. Profiling the top six lithium-producing countries in the world, November 2020. URL <https://www.nsenergybusiness.com>.
- [29] D. Bogdanov, J. Farfan, K. Sadovskaia, A. Aghahosseini, M. Child, A. Gulagi, A. S. Oyewo, L. de S-N. S. Barbosa, and C. Breyer. Radical transformation pathway towards sustainable electricity via evolutionary steps. *Nature Communications*, 10:1–16, 2019.
- [30] H. M. Conesa, R. Schulin, and B. Nowack. Mining landscape: A cultural tourist opportunity or an environmental problem?: The study case of the cartagena–la unión mining district (se spain). *Ecological Economics*, 64:690–700, 2008.
- [31] C. S. Santana, D. M. M. Olivares, V. H. C. Silva, F. H. M. Luzardo, F. G. Velasco, and R. M. de Jesus. Assessment of water resources pollution associated with mining activity in a semi-arid region. *Journal of Environmental Management*, 273:111148, 2020.
- [32] M. Contestabile, S. Panero, and B. Scrosati. A laboratory-scale lithium-ion battery recycling process. *Journal of Power Sources*, 92:65–69, 2001.
- [33] L. Gaines. Lithium-ion battery recycling processes: Research towards a sustainable course. *Sustainable Materials and Technologies*, 17:e00068, 2018.
- [34] R. E. Ciez and J. F. Whitacre. Examining different recycling processes for lithium-ion batteries. *Nature Sustainability*, 2:148–156, 2019.
- [35] J. Heelan, E. Gratz, Z. Zheng, Q. Wang, M. Chen, D. Apelian, and Y. Wang. Current and prospective Li-ion battery recycling and recovery processes. *Journal of Metals*, 68:2632–2638, 2016.

- [36] D. Kushnir. lithium ion battery recycling technology 2015. *Current State and Future Prospects*, pages 1–56, 2015.
- [37] X. Zheng, W. Gao, X. Zhang, M. He, X. Lin, H. Cao, Y. Zhang, and Z. Sun. Spent lithium-ion battery recycling–reductive ammonia leaching of metals from cathode scrap by sodium sulphite. *Waste Management*, 60:680–688, 2017.
- [38] W. T. Yin, C. Y. Yan, P. H. Ma, and F. Q. Li. Crystallization kinetics of lithium carbonate. *Chemical Engineering (China)*, 37:16–19, 2009.
- [39] N. Stieger and W. Liebenberg. *Recrystallization of Active Pharmaceutical Ingredients, Crystallization - Science and Technology*. IntechOpen, United Kingdom, 2012.
- [40] S. G. Kwon and T. Hyeon. Formation mechanisms of uniform nanocrystals via hot-injection and heat-up methods. *Small*, 7:2685–2702, 2011.
- [41] M. Kitamura. Controlling factor of polymorphism in crystallization process. *Journal of Crystal Growth*, 237:2205–2214, 2002.
- [42] C. Xiao and L. Zeng. Thermodynamic study on recovery of lithium using phosphate precipitation method. *Hydrometallurgy*, 178:283–286, 2018.
- [43] Y. Song and Z. Zhao. Recovery of lithium from spent lithium-ion batteries using precipitation and electro dialysis techniques. *Separation and Purification Technology*, 206:335–342, 2018.
- [44] E. D. Bøjesen and B. B. Iversen. The chemistry of nucleation. *CrystEngComm*, 18: 8332–8353, 2016.
- [45] N. P. Das, B. Müller, Á. Tóth, D. Horváth, and G. Schuszter. Macroscale precipitation kinetics: Towards complex precipitate structure design. *Physical Chemistry Chemical Physics*, 20:19768–19775, 2018.
- [46] N. Dhakal, S. G. Salinas Rodriguez, J. C. Schippers, and M. D. Kennedy. Induction time measurements in two brackish water reverse osmosis plants for calcium carbonate precipitation. *Desalination and Water Treatment*, 53:285–293, 2015.
- [47] S. Jain and M. P. Sharma. Measurement of the oxidation stability of biodiesel using a modified karl fischer apparatus. *Journal of the American Oil Chemists' Society*, 88: 899–905, 2011.
- [48] E. İçten, Z. K. Nagy, and G. V. Reklaitis. Modelling of crystallization of solid oral drug forms in a dropwise additive manufacturing system. In *Computer Aided Chemical Engineering*, volume 37, pages 2195–2200. Elsevier, 2015.

- [49] P. Laval, J-B. Salmon, and M. Joanicot. A microfluidic device for investigating crystal nucleation kinetics. *Journal of Crystal Growth*, 303:622–628, 2007.
- [50] B. C. Batista and O. Steinbock. Growing inorganic membranes in microfluidic devices: Chemical gardens reduced to linear walls. *Journal of Physical Chemistry C*, 119:27045–27052, 2015.
- [51] M. E. Brown. Stocktaking in the kinetics cupboard. *Journal of Thermal Analysis and Calorimetry*, 2005.
- [52] A. Khawam and D. R. Flanagan. Solid-state kinetic models: basics and mathematical fundamentals. *The Journal of Physical Chemistry B*, 110:17315–17328, 2006.
- [53] A. Forgács, K. Moldován, P. Herman, E. Baranyai, I. Fábián, G. Lente, and J. Kalmár. Kinetic model for hydrolytic nucleation and growth of tio<sub>2</sub> nanoparticles. *The Journal of Physical Chemistry C*, 122:19161–19170, 2018.
- [54] X. Y Liu. A new kinetic model for three-dimensional heterogeneous nucleation. *The Journal of Chemical Physics*, 111:1628–1635, 1999.
- [55] X. Y Liu, K. Tsukamoto, and M. Sorai. New kinetics of caco<sub>3</sub> nucleation and microgravity effect. *Langmuir*, 16:5499–5502, 2000.
- [56] X. Y Liu. Generic progressive heterogeneous processes in nucleation. *Langmuir*, 16:7337–7345, 2000.
- [57] R. Boistelle and J. P Astier. Crystallization mechanisms in solution. *Journal of Crystal Growth*, 90:14–30, 1988.
- [58] A. Mersmann. *Crystallization Technology Handbook*. CRC press, 2001.
- [59] C. Devos, T. Van Gerven, and S. Kuhn. A review of experimental methods for nucleation rate determination in large-volume batch and microfluidic crystallization. *Crystal Growth & Design*, 21:2541–2565, 2021.
- [60] J. W. Mullin. Crystallization, butterworth-heinemann. London, UK, 2001.
- [61] J. H. Espenson. *Chemical Kinetics and Reaction Mechanisms*, volume 102. Citeseer, 1995.
- [62] M. Davies, P. Johnson, A. F. Wells, and H. M. Powell. General and physical chemistry. *Annual Reports on the Progress of Chemistry*, 43:5–103, 1946.
- [63] B. R. Pamplin. *Crystal Growth: International Series on the Science of the Solid State*. Elsevier, 2013.

- [64] A. A. Chernov. Formation of crystals in solutions. *Contemporary Physics*, 30:251–276, 1989.
- [65] J. Leng and J-B. Salmon. Microfluidic crystallization. *Lab on a Chip*, 9:24–34, 2009.
- [66] M. Maeki, S. Yamazaki, A. S. Pawate, A. Ishida, H. Tani, K. Yamashita, M. Sugishima, K. Watanabe, M. Tokeshi, P. A. Kenis, and M. Miyazaki. A microfluidic-based protein crystallization method in 10 micrometer-sized crystallization space. *CrystEngComm*, 18:7722–7727, 2016.
- [67] M. Ildefonso, E. Revalor, P. Punniyam, J. B. Salmon, N. Candoni, and S. Veessler. Nucleation and polymorphism explored via an easy-to-use microfluidic tool. *Journal of Crystal Growth*, 342:9–12, 2012.
- [68] P. Laval, A. Crombez, and J-B. Salmon. Microfluidic droplet method for nucleation kinetics measurements. *Langmuir*, 25:1836–1841, 2009.
- [69] M. Ildefonso, N. Candoni, and S. Veessler. Heterogeneous nucleation in droplet-based nucleation measurements. *Crystal Growth and Design*, 13:2107–2110, 2013.
- [70] J-u. Shim, G. Cristobal, D. R. Link, T. Thorsen, Y. Jia, K. Piattelli, and S. Fraden. Control and measurement of the phase behavior of aqueous solutions using microfluidics. *Journal of American Chemical Society*, 129:8825–8835, 2007.
- [71] J. Cavanaugh, M. L. Whittaker, and D. Joester. Crystallization kinetics of amorphous calcium carbonate in confinement. *Chemical Science*, 10:5039–5043, 2019.
- [72] Q. Wang, M. R. Bentley, and O. Steinbock. Self-organization of layered inorganic membranes in microfluidic devices. *Journal of Physical Chemistry C*, 121:14120–14127, 2017.
- [73] Q. Wang and O. Steinbock. Materials synthesis and catalysis in microfluidic devices: Prebiotic chemistry in mineral membranes. *Chemical Catalysis Catalytical Chemistry*, 12:63–74, 2020.
- [74] I. W. Donald. Preparation, properties and chemistry of glass-and glass-ceramic-to-metal seals and coatings. *Journal of Materials Science*, 28:2841–2886, 1993.
- [75] J. D. Gunton. Homogeneous nucleation. *Journal of Statistical Physics*, 95:903–923, 1999.
- [76] W. J. Gibbs. *The Collected Works. Vol. 1. Thermodynamics*. Yale University Press, 1948.
- [77] P. G. Debenedetti. *Metastable liquids*. Princeton University Press, 2021.

- [78] S. Karthika, T. K. Radhakrishnan, and P. Kalaichelvi. A review of classical and non-classical nucleation theories. *Crystal Growth & Design*, 16:6663–6681, 2016.
- [79] J. F. Lutsko and M. A. Durán-Olivencia. Classical nucleation theory from a dynamical approach to nucleation. *The Journal of Chemical Physics*, 138:244908, 2013.
- [80] J. Weber, J. N Bracco, K. Yuan, V. Starchenko, and A. G. Stack. Studies of mineral nucleation and growth across multiple scales: Review of the current state of research using the example of barite ( $\text{BaSO}_4$ ). *ACS Earth and Space Chemistry*, 5:3338–3361, 2021.
- [81] J. J. De Yoreo and P. G. Vekilov. Principles of crystal nucleation and growth. *Reviews in Mineralogy and Geochemistry*, 54:57–93, 2003.
- [82] D. Erdemir, A. Y. Lee, and A. S. Myerson. Nucleation of crystals from solution: classical and two-step models. *Accounts of Chemical Research*, 42:621–629, 2009.
- [83] R. J. Davey, S. L. M. Schroeder, and J. H. Ter Horst. Nucleation of organic crystals—a molecular perspective. *Angewandte Chemie International Edition*, 52:2166–2179, 2013.
- [84] Dimo Kashchiev. *Nucleation*. Elsevier, 2000.
- [85] D Brus, V. Ždímal, and J. Smolík. Homogeneous nucleation rate measurements in supersaturated water vapor. *The Journal of Chemical Physics*, 129:174501, 2008.
- [86] Y. J. Kim, B. E. Wyslouzil, G. Wilemski, J. Wölk, and R. Strey. Isothermal nucleation rates in supersonic nozzles and the properties of small water clusters. *The Journal of Physical Chemistry A*, 108:4365–4377, 2004.
- [87] A. A. Manka, D. Brus, A. Hyvärinen, H. Lihavainen, J. Wölk, and R. Strey. Homogeneous water nucleation in a laminar flow diffusion chamber. *The Journal of Chemical Physics*, 132:244505, 2010.
- [88] J. L. Katz and B. J. Ostermier. Diffusion cloud-chamber investigation of homogeneous nucleation. *The Journal of Chemical Physics*, 47:478–487, 1967.
- [89] P. E. Wagner and R. Strey. Measurements of homogeneous nucleation rates for n-nonane vapor using a two-piston expansion chamber. *The Journal of Chemical Physics*, 80:5266–5275, 1984.
- [90] D. W. Oxtoby. Homogeneous nucleation: theory and experiment. *Journal of Physics: Condensed Matter*, 4:7627, 1992.
- [91] A. E. Nielsen. Kinetics of precipitation, 1964.

- [92] S. Auer and D. Frenkel. Numerical prediction of absolute crystallization rates in hard-sphere colloids. *The Journal of Chemical Physics*, 120:3015–3029, 2004.
- [93] D. Reguera, R. K. Bowles, Y. Djikaev, and H. Reiss. Phase transitions in systems small enough to be clusters. *The Journal of Chemical Physics*, 118:340–353, 2003.
- [94] L. Gránásy and F. Iglói. Comparison of experiments and modern theories of crystal nucleation. *The Journal of Chemical Physics*, 107:3634–3644, 1997.
- [95] L. Gránásy. Fundamentals of the diffuse interface theory of nucleation. *The journal of Physical Chemistry*, 100:10768–10770, 1996.
- [96] P. Harrowell and D. W. Oxtoby. A molecular theory of crystal nucleation from the melt. *The Journal of Chemical Physics*, 80:1639–1646, 1984.
- [97] C. K. Bagdassarian and D. W. Oxtoby. Crystal nucleation and growth from the undercooled liquid: A nonclassical piecewise parabolic free-energy model. *The Journal of Chemical Physics*, 100:2139–2148, 1994.
- [98] P. G. Vekilov. Nonclassical nucleation. In *Crystallization via Nonclassical Pathways Volume 1: Nucleation, Assembly, Observation & Application*, pages 19–46. ACS Publications, 2020.
- [99] C. B. Whitehead, S. Özkar, and R. G. Finke. Lamer’s 1950 model of particle formation: a review and critical analysis of its classical nucleation and fluctuation theory basis, of competing models and mechanisms for phase-changes and particle formation, and then of its application to silver halide, semiconductor, metal, and metal-oxide nanoparticles. *Materials Advances*, 2:186–235, 2021.
- [100] M. H. Ramirez Acosta, L. Raphael Rodrigues, D. R. Cassar, M. Montazerian, O. Peitl Filho, and E. Dutra Zanotto. Further evidence against the alleged failure of the classical nucleation theory below the glass transition range. *Journal of the American Ceramic Society*, 104:4537–4549, 2021.
- [101] S. He, J. E. Oddo, and M. B. Tomson. The nucleation kinetics of barium sulfate in nacl solutions up to 6 m and 90 c. *Journal of Colloid and Interface Science*, 174:319–326, 1995.
- [102] F. Jones, M. I. Ogden, and T. Radomirovic. The impact of sulfite ions on barium sulfate crystallization. *Journal of Crystal Growth*, 507:213–219, 2019.
- [103] M. C. Van der Leeden, D. Kashchiev, and G. M. Van Rosmalen. Precipitation of barium sulfate: Induction time and the effect of an additive on nucleation and growth. *Journal of Colloid and Interface Science*, 152:338–350, 1992.

- [104] G. M. Van Rosmalen and P. Bennema. Characterization of additive performance on crystallization: Habit modification. *Journal of Crystal Growth*, 99:1053–1060, 1990.
- [105] K. Yuan, V. Starchenko, N. Rampal, F. Yang, X. Yang, X. Xiao, W-K. Lee, and A. G. Stack. Opposing effects of impurity ion  $\text{Sr}^{2+}$  on the heterogeneous nucleation and growth of barite ( $\text{BaSO}_4$ ). *Crystal Growth & Design*, 21:5828–5839, 2021.
- [106] A. Navrotsky. Energetic clues to pathways to biomineralization: Precursors, clusters, and nanoparticles. *Proceedings of the National Academy of Sciences*, 101:12096–12101, 2004.
- [107] A. I. Vavouraki, C. V. Putnis, A. Putnis, and P. G. Koutsoukos. An atomic force microscopy study of the growth of calcite in the presence of sodium sulfate. *Chemical Geology*, 253:243–251, 2008.
- [108] P. Bots, L. G. Benning, J-D. Rodriguez-Blanco, T. Roncal-Herrero, and S. Shaw. Mechanistic insights into the crystallization of amorphous calcium carbonate (acc). *Crystal Growth & Design*, 12:3806–3814, 2012.
- [109] J. D. Rodriguez-Blanco, S. Shaw, and L. G. Benning. The kinetics and mechanisms of amorphous calcium carbonate (acc) crystallization to calcite, via vaterite. *Nanoscale*, 3:265–271, 2011.
- [110] D. J. Tobler, J. D. Rodriguez-Blanco, K. Dideriksen, N. Bovet, K. K. Sand, and S. L. S. Stipp. Citrate effects on amorphous calcium carbonate (acc) structure, stability, and crystallization. *Advanced Functional Materials*, 25:3081–3090, 2015.
- [111] N. P. Das, R. Zahorán, L. Janovák, Á. Deák, Á. Tóth, D. Horváth, and G. Schusztter. Kinetic characterization of precipitation reactions: Possible link between a phenomenological equation and reaction pathway. *Crystal Growth & Design*, 20:7392–7398, 2020.
- [112] A. Forgacs, K. Moldovan, P. Herman, E. Baranyai, I. Fabian, G. Lente, and Jozsef Kalmar. Kinetic model for hydrolytic nucleation and growth of  $\text{TiO}_2$  nanoparticles. *The Journal of Physical Chemistry C*, 122:19161–19170, 2018.
- [113] R. Szabo and G. Lente. A comparison of the stochastic and deterministic approaches in a nucleation–growth type model of nanoparticle formation. *Chemistry of Materials*, 33:5430–5436, 2021.
- [114] K. Taguchi, J. Garside, and N. S. Tavaré. Nucleation and growth kinetics of barium sulphate in batch precipitation. *Journal of Crystal Growth*, 163:318–328, 1996.

- [115] Z. Guo, X. Zhang, W. Han, L. Li, and L. Wang. Interpretation of the ultrasonic effect on induction time during baso4 heterogeneous nucleation by a cluster coagulation model. *Crystal Research and Technology*, 53:1700124, 2018.
- [116] John McGinty, Nima Yazdanpanah, Chris Price, Joop H. ter Horst, and Jan Sefcik. Chapter 1 nucleation and crystal growth in continuous crystallization. In *The Handbook of Continuous Crystallization*, pages 1–50. The Royal Society of Chemistry, 2020. ISBN 978-1-78801-214-0. doi: 10.1039/9781788013581-00001. URL <http://dx.doi.org/10.1039/9781788013581-00001>.
- [117] C. J. Callahan and X-W. Ni. An investigation into the effect of mixing on the secondary nucleation of sodium chlorate in a stirred tank and an oscillatory baffled crystallizer. *CrystEngComm*, 16:690–697, 2014.
- [118] W. Yi, C. Yan, and P. Ma. Crystallization kinetics of  $\text{Li}_2\text{CO}_3$  from  $\text{LiHCO}_3$  solutions. *Journal of Crystal Growth*, 312:2345–2350, 2010.
- [119] B. Han, R. A. Ul-Haq, and M. Louhi-Kultanen. Lithium carbonate precipitation by homogeneous and heterogeneous reactive crystallization. *Hydrometallurgy*, 195:105386, 2020.
- [120] C. Zhao, Y. Zhang, H. Cao, X. Zheng, T. Van Gerven, Y. Hu, and Z. Sun. Lithium carbonate recovery from lithium-containing solution by ultrasound assisted precipitation. *Ultrasonics Sonochemistry*, 52:484–492, 2019.
- [121] P. G. Aguilar and T. A. Graber. Determination of the reaction kinetic parameters for  $\text{Li}_2\text{CO}_3$  crystallization from  $\text{Li}_2\text{SO}_4$  and  $\text{Na}_2\text{CO}_3$  solutions using calorimetric measurements. *Industrial & Engineering Chemistry Research*, 57:4815–4823, 2018.
- [122] G. Montante, J. R. Bourne, and F. Magelli. Scale-up of solids distribution in slurry, stirred vessels based on turbulence intermittency. *Industrial & Engineering Chemistry Research*, 47:3438–3443, 2008.
- [123] Y. J. Yi and A. S. Myerson. Laboratory scale batch crystallization and the role of vessel size. *Chemical Engineering Research and Design*, 84:721–728, 2006.
- [124] M. Bohlin and Å. C. Rasmuson. Importance of macromixing in batch cooling crystallization. *AIChE Journal*, 42:691–699, 1996.
- [125] R. Zauner and A. G. Jones. On the influence of mixing on crystal precipitation processes—application of the segregated feed model. *Chemical Engineering Science*, 57:821–831, 2002.
- [126] J. Bałdyga, W. Orciuch, et al. Double-feed semibatch precipitation effects of mixing. *Chemical Engineering Research and Design*, 85(5):745–752, 2007.

- [127] R. Zauner and A. G. Jones. Scale-up of continuous and semibatch precipitation processes. *Industrial & Engineering Chemistry Research*, 39:2392–2403, 2000.
- [128] S. Li, J. Xu, and G. Luo. Control of crystal morphology through supersaturation ratio and mixing conditions. *Journal of Crystal Growth*, 304:219–224, 2007.
- [129] M. L. J. Van Leeuwen, O. S. L. Bruinsma, and G. M. Van Rosmalen. Influence of mixing on the product quality in precipitation. *Chemical Engineering Science*, 51:2595–2600, 1996.
- [130] L. Wang, I. Sondi, and E. Matijević. Preparation of uniform needle-like aragonite particles by homogeneous precipitation. *Journal of Colloid and Interface Science*, 218:545–553, 1999.
- [131] Y. Mao, F. Li, T. Wang, X. Cheng, G. Li, D. Li, X. Zhang, and H. Hao. Enhancement of lysozyme crystallization under ultrasound field. *Ultrasonics Sonochemistry*, 63:104975, 2020.
- [132] G. Navarra, F. Troia, V. Militello, and M. Leone. Characterization of the nucleation process of lysozyme at physiological pH: Primary but not sole process. *Biophysical Chemistry*, 177:24–33, 2013.
- [133] B. Bohner, G. Schusztter, D. Horváth, and Á. Tóth. Morphology control by flow-driven self-organizing precipitation. *Chemical Physics Letters*, 631:114–117, 2015.
- [134] G. Schusztter, F. Brau, and A. De Wit. Flow-driven control of calcium carbonate precipitation patterns in a confined geometry. *Physical Chemistry Chemical Physics*, 18:25592–25600, 2016.
- [135] Q. Wang, K. S. Hernesman, and O. Steinbock. Flow-driven precipitation patterns with microemulsions in a confined geometry. *ChemSystemsChem*, 2:e1900037, 2020.
- [136] I. Ziemecka, S. Gokalp, S. Stroobants, F. Brau, D. Maes, and A. De Wit. Polymorph selection of rox by flow-driven crystallization. *Crystals*, 9:351, 2019.
- [137] J. J. Chen, J. J. Thomas, H. F. W. Taylor, and H. M. Jennings. Solubility and structure of calcium silicate hydrate. *Cement and Concrete Research*, 34:1499–1519, 2004.
- [138] S. Hussein, J. Maselko, and J. T. Pantaleone. Growing a chemical garden at the air–fluid interface. *Langmuir*, 32:706–711, 2016.
- [139] E. Balog, P. Papp, Á. Tóth, D. Horváth, and G. Schusztter. The impact of reaction rate on the formation of flow-driven confined precipitate patterns. *Physical Chemistry Chemical Physics*, 22:13390–13397, 2020.

- [140] E. Tóth-Szeles, G. Schusztar, Á. Tóth, Z. Kónya, and D. Horváth. Flow-driven morphology control in the cobalt–oxalate system. *CrystEngComm*, 18:2057–2064, 2016.
- [141] E. Tóth-Szeles, B. Bohner, Á. Tóth, and D. Horváth. Spatial separation of copper and cobalt oxalate by flow-driven precipitation. *Crystal Growth & Design*, 17:5000–5005, 2017.
- [142] D. A. Stone and R. E. Goldstein. Tubular precipitation and redox gradients on a bubbling template. *Proceedings of the National Academy of Sciences*, 101:11537–11541, 2004.
- [143] S. Thouvenel-Romans, J. J. Pagano, and O. Steinbock. Bubble guidance of tubular growth in reaction–precipitation systems. *Physical Chemistry Chemical Physics*, 7:2610–2615, 2005.
- [144] D. A. Stone, B. Lewellyn, J. C. Baygents, and R. E. Goldstein. Precipitative growth templated by a fluid jet. *Langmuir*, 21:10916–10919, 2005.
- [145] D. Kashchiev, D. Verdoes, and G. M. Van Rosmalen. Induction time and metastability limit in new phase formation. *Journal of Crystal Growth*, 110:373–380, 1991.
- [146] P. Coliaie, M. S. Kelkar, N. K. Nere, and M. R. Singh. Continuous-flow, well-mixed, microfluidic crystallization device for screening of polymorphs, morphology, and crystallization kinetics at controlled supersaturation. *Lab on a Chip*, 19:2373–2382, 2019.
- [147] P. Laval, C. Giroux, J. Leng, and J-B. Salmon. Microfluidic screening of potassium nitrate polymorphism. *Journal of Crystal Growth*, 310:3121–3124, 2008.
- [148] P. Laval, N. Lisai, J-B. Salmon, and M. Joanicot. A microfluidic device based on droplet storage for screening solubility diagrams. *Lab on a Chip*, 7:829–834, 2007.
- [149] S. Talreja, P. J. A. Kenis, and C. F. Zukoski. A kinetic model to simulate protein crystal growth in an evaporation-based crystallization platform. *Langmuir*, 23:4516–4522, 2007.
- [150] M. K. Yadav, C. J. Gerds, R. Sanishvili, W. W. Smith, L. S. Roach, R. F. Ismagilov, P. Kuhn, and R. C. Stevens. In situ data collection and structure refinement from microcapillary protein crystallization. *Journal of Applied Crystallography*, 38:900–905, 2005.
- [151] G. Laffite, C. Leroy, C. Bonhomme, L. Bonhomme-Coury, E. Letavernier, M. Daudon, V. Frochot, J. P. Haymann, S. Rouzière, I. T. Lucas, D. Bazin, F. Babonneau, and

- A. Abou-Hassan. Calcium oxalate precipitation by diffusion using laminar microfluidics: toward a biomimetic model of pathological microcalcifications. *Lab on a Chip*, 16:1157–1160, 2016.
- [152] Y. Zeng, J. Cao, Z. Wang, J. Guo, and J. Lu. Formation of amorphous calcium carbonate and its transformation mechanism to crystalline  $\text{CaCO}_3$  in laminar microfluidics. *Crystal Growth and Design*, 18:1710–1721, 2018.
- [153] Y. Zeng, J. Cao, Z. Wang, J. Guo, Q. Zhou, and J. Lu. Insights into the confined crystallization in microfluidics of amorphous calcium carbonate. *Crystal Growth and Design*, 18:6538–6546, 2018.
- [154] A. Perazzo, L. Sicignano, G. Tomaiuolo, R. Marotta, R. Andreozzi, and S. Guido. Tuning crystal structure in a micro-scale reactive flow. *Chemical Engineering Science*, 207:581–587, 2019.
- [155] A. Sanjoh and T. Tsukihara. Spatiotemporal protein crystal growth studies using microfluidic silicon devices. *Journal of Crystal Growth*, 196:691–702, 1999.
- [156] Y. Ding, B. Batista, O. Steinbock, J. H. E. Cartwright, and S. S. S. Cardoso. Wavy membranes and the growth rate of a planar chemical garden: Enhanced diffusion and bioenergetics. *Proceedings of the National Academy of Sciences*, 113:9182–9186, 2016.
- [157] L. M. Barge, S. S. S. Cardoso, J. H. E. Cartwright, G. J. T. Cooper, L. Cronin, A. De Wit, I. J. Doloboff, B. Escibano, R. E. Goldstein, F. Haudin, et al. From chemical gardens to chemobionics. *Chemical Reviews*, 115:8652–8703, 2015.
- [158] J. Whitfield. Origin of life: Nascence man. *Nature News*, 459:316–319, 2009.
- [159] M. J. Russell and A. J. Hall. The emergence of life from iron monosulphide bubbles at a submarine hydrothermal redox and pH front. *Journal of the Geological Society*, 154:377–402, 1997.
- [160] S. S. S. Cardoso, J. H. E. Cartwright, and C. I. Sainz-Díaz. Carbonate-hydroxide chemical-garden tubes in the soda ocean of Enceladus: Abiotic membranes and microtubular forms of calcium carbonate. *Icarus*, 319:337–348, 2019.
- [161] L. M. Barge, I. J. Doloboff, L. M. White, G. D. Stucky, M. J. Russell, and I. Kanik. Characterization of iron–phosphate–silicate chemical garden structures. *Langmuir*, 28:3714–3721, 2012.
- [162] M. J. Russell and A. J. Hall. The onset and early evolution of life. *Memoirs-Geological Society of America*, 198:1, 2006.

- [163] R. E. Mielke, K. J. Robinson, L. M. White, S. E. McGlynn, K. McEachern, R. Bhartia, I. Kanik, and M. J. Russell. Iron-sulfide-bearing chimneys as potential catalytic energy traps at life's emergence. *Astrobiology*, 11:933–950, 2011.
- [164] M. J. Russell, L. M. Barge, R. Bhartia, D. Bocanegra, P. J. Bracher, E. Branscomb, R. Kidd, S. McGlynn, D. H. Meier, W. Nitschke, et al. The drive to life on wet and icy worlds. *Astrobiology*, 14:308–343, 2014.
- [165] L. M. Barge, J-P. Jones, J. J. Pagano, E. Martinez, and J. Bescup. Three-dimensional analysis of a simulated prebiotic hydrothermal chimney. *ACS Earth and Space Chemistry*, 4:1663–1669, 2020.
- [166] B. C. Batista and O. Steinbock. Chemical gardens without silica: The formation of pure metal hydroxide tubes. *Chemical Communications*, 51:12962–12965, 2015.
- [167] F. Brau, F. Haudin, S. Thouvenel-Romans, A. De Wit, O. Steinbock, S. S. S. Cardoso, and J. H. E. Cartwright. Filament dynamics in confined chemical gardens and in filiform corrosion. *Physical Chemistry Chemical Physics*, 20:784–793, 2018.
- [168] O. Steinbock, J. H. E. Cartwright, and L. M. Barge. The fertile physics of chemical gardens. *Physics Today*, 69:44–51, 2016.
- [169] P. Kumar, C. Hajdu, Á. Tóth, and D. Horváth. Flow-driven surface instabilities of tubular chitosan hydrogel. *ChemPhysChem*, 22:488, 2021.
- [170] F. Haudin, J. H. E. Cartwright, F. Brau, and A. De Wit. Spiral precipitation patterns in confined chemical gardens. *Proceedings of the National Academy of Sciences*, 111:17363–17367, 2014.
- [171] P. Kumar, D. Horváth, and Á. Tóth. Bio-inspired flow-driven chitosan chemical gardens. *Soft Matter*, 16:8325–8329, 2020.
- [172] J. H. E. Cartwright, B. Escribano, C. I. Sainz-Díaz, and L. S. Stodieck. Chemical-garden formation, morphology, and composition. ii. chemical gardens in microgravity. *Langmuir*, 27:3294–3300, 2011.
- [173] J. H. E. Cartwright, J. M. García-Ruiz, M. L. Novella, and F. Otálora. Formation of chemical gardens. *Journal of Colloid and Interface Science*, 256:351–359, 2002.
- [174] V. Kaminker, J. Maselko, and J. Pantaleone. The dynamics of open precipitation tubes. *The Journal of Chemical Physics*, 140:244901, 2014.
- [175] Q. Wang and O. Steinbock. Chemical garden membranes in temperature-controlled microfluidic devices. *Langmuir*, 37:2485–2493, 2021.

- [176] L. M. Barge, Y. Abedian, M. J. Russell, I. J. Doloboff, J. H. E. Cartwright, R. D. Kidd, and I. Kanik. From chemical gardens to fuel cells: Generation of electrical potential and current across self-assembling iron mineral membranes. *Angewandte Chemie International Edition*, 54:8184–8187, 2015.
- [177] S. E. McGlynn, I. Kanik, and M. J. Russell. Peptide and rna contributions to iron–sulphur chemical gardens as life’s first inorganic compartments, catalysts, capacitors and condensers. *Philosophical Transactions of the Royal Society A: Mathematical, Physical and Engineering Sciences*, 370:3007–3022, 2012.
- [178] L. M. Barge, Y. Abedian, I. J. Doloboff, J. E. Nuñez, M. J. Russell, R. D. Kidd, and I. Kanik. Chemical gardens as flow-through reactors simulating natural hydrothermal systems. *Journal of Visualized Experiments*, page 53015, 2015.
- [179] W. Zhao and K. Sakurai. Realtime observation of diffusing elements in a chemical garden. *ACS Omega*, 2:4363–4369, 2017.
- [180] K. Migacz, J. Chłopek, and A. Morawska-Chochół. Gradient composite materials for artificial intervertebral discs. *Acta of Bioengineering and Biomechanics*, 16, 2014.
- [181] M. B. Bever and P. E. Duwez. Gradients in composite materials. *Materials Science and Engineering*, 10:1–8, 1972.
- [182] D. A. Skoog, F. J. Holler, and S. R. Crouch. *Principles of instrumental analysis*. Cengage Learning, 2017.
- [183] K. C. A. Smith and C. W. Oatley. The scanning electron microscope and its fields of application. *British Journal of Applied Physics*, 6:391, 1955.
- [184] G. Shiers. *Early television: A bibliographic guide to 1940*. Routledge, 2014.
- [185] A Furtado, E Batista, I Spohr, and E Filipe. Measurement of density using oscillation-type density meters calibration, traceability and uncertainties. *Proceedings of the 14ème Congrès International de Métrologie*, 2009.
- [186] H. A. Barnes, J. F. Hutton, and K. Walters. *An introduction to rheology*, volume 3. Elsevier, 1989.
- [187] David R Lide. *CRC handbook of chemistry and physics*, volume 85. CRC press, 2004.
- [188] Stanislav Kotrly and Ladislav Sucha. *Handbook of Chemical Equilibria in Analytical Chemistry*. Ellis Horwood Limited, 1985.
- [189] S. Jiang and J. H. ter Horst. Crystal nucleation rates from probability distributions of induction times. *Crystal Growth & Design*, 11:256–261, 2011.

- [190] C. Brandel and J. H. ter Horst. Measuring induction times and crystal nucleation rates. *Faraday Discussions*, 179:199–214, 2015.
- [191] M. Emmanuel, P. Papp, G. Schuszter, Á. Deák, L. Janovák, Á. Tóth, and D. Horváth. Nucleation kinetics of lithium phosphate precipitation. *CrystEngComm*, 2022.
- [192] P. G. Vekilov. Nucleation. *Crystal Growth & Design*, 10:5007–5019, 2010.
- [193] J. Anwar and D. Zahn. Uncovering molecular processes in crystal nucleation and growth by using molecular simulation. *Angewandte Chemie International Edition*, 50:1996–2013, 2011.
- [194] O. Söhnel and J.W. Mullin. A method for the determination of precipitation induction periods. *Journal of Crystal Growth*, 44:377 – 382, 1978.
- [195] J. W. Mullin and A. Amatavivadhana. Growth kinetics of ammonium- and potassium-dihydrogen phosphate crystals. *Journal of Applied Chemistry*, 17:151–156, 1967.
- [196] J. W. Mullin and H-M. Ang. Nucleation characteristics of aqueous nickel ammonium sulphate solutions. *Faraday Discussions of the Chemical Society*, 61:141–148, 1976.
- [197] A. Mersmann. Calculation of interfacial tensions. *Journal of Crystal Growth*, 102: 841–847, 1990.
- [198] E. S. Howard, C. M. Marlene, H. E. Eloise, and U. Linda. *Standard X-ray Diffraction Powder Patterns*. National Bureau of Standards, U.S. Department of Commerce, 25 edition, 1965.
- [199] C. Keffer, A. D. Mighell, F. Mauer, H. E. Swanson, and S. Block. Crystal structure of twinned low-temperature lithium phosphate. *Inorganic Chemistry*, 6:119–125, 1967.
- [200] M. Emmanuel, D. Horváth, and Á. Tóth. Flow-driven crystal growth of lithium phosphate in microchannels. *CrystEngComm*, 22:4887–4893, 2020.
- [201] R. D. Sosa, X. Geng, M. A. Reynolds, J. D. Rimer, and J. C. Conrad. A microfluidic approach for probing hydrodynamic effects in barite scale formation. *Lab Chip*, 19: 1534–1544, 2019.
- [202] L. Gálfi and Z. Rácz. Properties of the reaction front in an a+b->c type reaction-diffusion process. *Physical Review. A*, 38:3151–3154, 1988.
- [203] N. I. P. Ayu, E. Kartini, L. D. Prayogi, M. Faisal, and A. Supardi. Crystal structure analysis of Li<sub>3</sub>PO<sub>4</sub> powder prepared by wet chemical reaction and solid-state reaction by using x-ray diffraction (xrd). *Ionics*, 22:1051–1057, 2016.

- [204] N. Yabuuchi, Y. Yamakawa, K. Yoshii, and S. Komaba. Low-temperature phase of  $\text{Li}_2\text{FeSiO}_4$ : crystal structure and a preliminary study of electrochemical behavior. *Dalton Transactions*, 40:1846–1848, 2011.
- [205] M. E. Arroyo-deDompablo, R. Dominko, J. M. Gallardo-Amores, L. Dupont, G. Mali, H. Ehrenberg, J. Jamnik, and E. Morán. On the energetic stability and electrochemistry of  $\text{Li}_2\text{MnSiO}_4$  polymorphs. *Chemistry of Materials.*, 20:5574–5584, 2008.
- [206] Q. Wang and O. Steinbock. Materials synthesis and catalysis in microfluidic devices: Prebiotic chemistry in mineral membranes. *Chemical Catalysis Catalytical Chemistry*, pages 63–74, 2020.
- [207] E. Rauscher, G. Schuszter, B. Bohner, Á. Tóth, and D. Horváth. Osmotic contribution to the flow-driven tube formation of copper–phosphate and copper–silicate chemical gardens. *Physical Chemistry Chemical Physics*, 20:5766–5770, 2018.
- [208] M. Emmanuel, E. Lantos, D. Horváth, and Á. Tóth. Formation and growth of lithium phosphate chemical gardens. *Soft Matter*, 18:1731–1736, 2022.
- [209] S. Thouvenel-Romans, W. Van Saarloos, and O. Steinbock. Silica tubes in chemical gardens: Radius selection and its hydrodynamic origin. *Europhysics Letters*, 67:42, 2004.

# Appendix I

## Pressure and injection rate parameters

Figure I.1 represents a typical pressure and injection rate data obtained for a microfluidic experiment. The graph shows a rise in the pressure settings with time for the individual channels. Despite the difference in the pressures, the solution injection rate (green and blue solid lines) remains the same due to the presence of the pressure sensor coupled in the microfluidic system. The injected solutions, therefore, enter the channel at the same rate, since the effect of the pressure fluctuation is eliminated by the pressure sensor.

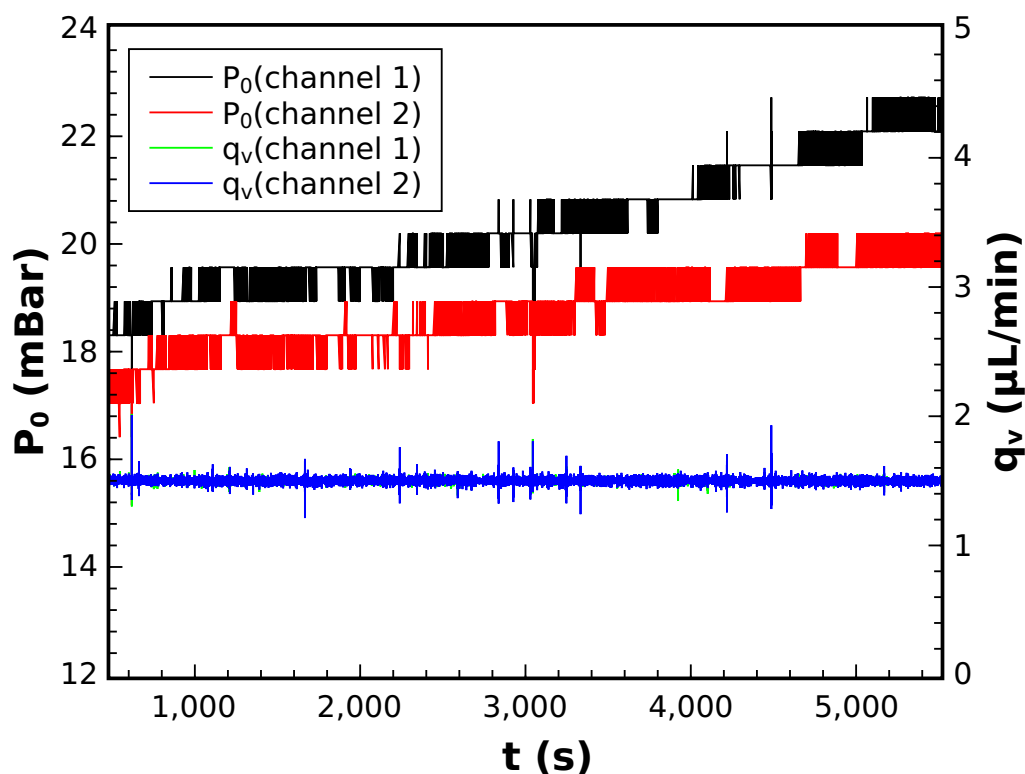


Figure I.1: Typical pressure data for injection rates set at  $1.5 \mu\text{L}/\text{min}/\text{channel}$  in a microfluidic system.

## Appendix II

### Determination of Induction time

This program is used in Mathematica to read from a file containing the turbidity data as a function of time. It makes a plot of the data to a given range. It carries out a linear fit of the data until there is a significant deviation from linearity. The point at which this deviation is observed is registered as the induction time. It allows for tuning the range of deviation to be used and also allows for tuning out the scattered data due to noise during measurement.

```
KinRead[fn_, tur_] :=
Module[{data, i, np = 1},
data = Cases[Import[fn, "Table"], {_?NumberQ, ___}];
While[data[[np, 2]] < tur, np++];
Table[data[[i]], {i, np}]
]
IndTime[data_, nl_, nu_, lim_] :=

Module[{datafilt = {}, i, nuc, ni, n, lm},
lm = LinearModelFit[Table[data[[i]], {i, 1, nl}], x, x];
For[i = 1, i <= nl, i++,
If[(Abs[lm["StandardizedResiduals"][[i]]] < lim),
datafilt = AppendTo[datafilt, data[[i]]]];
For[i = nl + 1, i <= nu, i++,
datafilt = AppendTo[datafilt, data[[i]]]];
nuc = ni = Dimensions[datafilt][[1]];
For[n = nuc, n >= nl, n--,
lm = LinearModelFit[Table[datafilt[[i]], {i, n}], x, x];
Print[datafilt[[n, 1]], " ", lm["StandardizedResiduals"][[n]]];
If[[(ni == nuc) && (Abs[lm["StandardizedResiduals"][[n]]] < 1.0)],
ni = n + 1]];
Print[datafilt[[ni]]];
```

```

lm = LinearModelFit[Table[datafilt[[i]], {i, ni}], x, x];
Show[ListPlot[{Table[data[[i]], {i, 1, nu}],
Table[datafilt[[i]], {i, 1, nuc}],
Table[datafilt[[i]], {i, ni, nuc}]}],
Plot[lm[x], {x, 0, datafilt[[nuc, 1]}]]
]
ds = KinRead["directory_filename.extention",
0.02];

ListPlot[ds, PlotRange -> All]
IndTime[ds, lower_lim, upper_lim, stdev]

```

# Appendix III

## Converting and renaming image list files

This program reads and converts all images in a working directory with different extensions, to portable network graphics (png) versions of the image files, and saves them in a defined directory, with newly given filenames. A new \*.dat file is created containing the original details of the filenames and the corresponding  $\Delta t$ .

```
set ext [lindex $argv 0]
set tdir [lindex $argv 1]
set source [lsort [glob ".*$ext"]]
set n [llength $source]
set c "_"

set fbase [lindex $argv 2]
set dt [lindex $argv 3]
set f [open "$tdir/$fbase.dt" w]
puts $f [format "# %s %7s %10s %20s" "image" "t" "dt" "capture time"]
for {set i 0} {$i < $n} {incr i} {
if {$i == 0} {
#   set ext [lindex [split [lindex $source $i] "."] end]}
set io [format "%03d" $i]
puts -nonewline $f [format "%5d" $i]
puts -nonewline $f [format "%12.1f" $t]
puts -nonewline $f [format "%10.1f " $dt]
puts $f [format "%18s" [lindex [split [lindex $source $i] "."] 0]]
set t [expr ($t+$dt)]
# file rename [lindex $source $i] "$fbase$c$i.$ext"
# file copy [lindex $source $i] "$tdir/$fbase$c$i.$ext"
exec convert [lindex $source $i] "$tdir/$fbase$c$i.png"
close $f
```

# Appendix IV

## ImageJ Macro for measuring particle size

This macro reads all images in a working directory, draws a line of different orientations such as vertical, horizontal, and even diagonal, to select the image profile under the line and overlay all the selected profiles.

```
//
var wd; var fbase; var counter; var dig; var ext; var imin; var imax;
var iskip = 0; var dir var x; var x0; var x1; var y; var y0; var y1;

macro "Image Sequence Operation Action Tool -C037R02caP2c2eeee4c40" {

init_seq();

if (dir=="Vertical")
len=y1-y0;
else
len=x1-x0;
scan=floor((imax-imin))+1;
xval=newArray(0);
if (dir=="Vertical") {
for (xd=y0; xd<=y1; xd++)
xval=append(xval,xd);
f=File.open(wd+fbase+"-v"+i20c(x,4)+".dat");
} else {
for (xd=x0; xd<=x1; xd++)
xval=append(xval,xd);
f=File.open(wd+fbase+"-h"+i20c(y,4)+".dat");
}
print(f,"#len= "+len);
```

```

print(f,"#scan= "+scan);
for (i=imin; i<=imax; i++) {
i+=iskip;
open(fbase+"_"+i20c(i,dig)+"."+ext);
run("Find Edges");
//    yval=newArray(0);
print(f,"@type xy");
if (dir=="Vertical")
for (y=y0; y<=y1; y++)
print(f,i2c(xval[y-y0],4)+" "+i2c(grayscale(getPixel(x,y)),4));
else
for (x=x0; x<=x1; x++)
print(f,i2c(xval[x-x0],4)+" "+i2c(grayscale(getPixel(x,y)),4));
print(f,"&");
wait(1000);
close;
}
File.close(f);
}
function init_seq() {
open("");
wd=getInfo("image.directory");
fn=getInfo("image.filename");
iul=lastIndexOf(fn,"_");
idot=lastIndexOf(fn,".");
fbase=substring(fn,0,iul);
fcounter=substring(fn,iul+1,idot);
dig=lengthOf(fcounter);
counter=parseInt(fcounter);
ext=substring(fn,idot+1,lengthOf(fn));
ilist=newArray(0);
for (i=0; i<pow(10,dig); i++) {
fn=fbase+"_"+i20c(i,dig)+"."+ext;
if (File.exists(wd+fn))
ilist=append(ilist,i);
}
Array.getStatistics(ilist,imin,imax,imean,istd);
dirs=newArray(0);
dirs=append(dirs,"Vertical");

```

```

dirs=append(dirs,"Horizontal");
Dialog.create("Select direction");
Dialog.addChoice("Direction",dirs,"Vertical");
Dialog.show();
dir=Dialog.getChoice();
setTool("rectangle");
waitForUser("Select a rectangle");
getSelectionBounds(xi,yi,w,h);

if (dir=="Vertical") {
y0=yi;
y1=y0+h;
x=xi+w/2;
} else {
x0=xi;
x1=x0+w;
y=yi+h/2;
}
Dialog.create("Parameters");
Dialog.addString("fbase",fbase);
Dialog.addString("ext",ext);
Dialog.addNumber("iMin", imin);
Dialog.addNumber("iMax", imax);
Dialog.addNumber("iSkip", 0);
if (dir=="Vertical") {
Dialog.addNumber("x", x);
Dialog.addNumber("y0", y0);
Dialog.addNumber("y1", y1);
} else {
Dialog.addNumber("x0", x0);
Dialog.addNumber("x1", x1);
Dialog.addNumber("y", y);
}
Dialog.show();
fbase=Dialog.getString();
ext=Dialog.getString();
imin=Dialog.getNumber();
imax=Dialog.getNumber();
iskip=Dialog.getNumber();

```

```

if (dir=="Vertical") {
x=Dialog.getNumber();
y0=Dialog.getNumber();
y1=Dialog.getNumber();
} else {
x0=Dialog.getNumber();
x1=Dialog.getNumber();
y=Dialog.getNumber();
}
close();
return 0;
}
function i20c(i,ndig) {
s=toString(i);
while (lengthOf(s)<ndig)
s="0"+s;
return s;
}
function i2c(i,ndig) {
s=toString(i);
while (lengthOf(s)<ndig)
s=" "+s;
return s;
}
function append(arr, value) {
arr2 = newArray(arr.length+1);
for (i=0; i<arr.length; i++)
arr2[i] = arr[i];
arr2[arr.length] = value;
return arr2;
}
function grayscale(rgb) {
r=(rgb & 0xff0000) >> 16;
g=(rgb & 0x00ff00) >> 8;
b=rgb & 0x0000ff;
return (floor(0.2989*r+0.5870*g+0.1140*b));
}

```

# Appendix V

## Calculation of the speciation of ions

This program calculates the concentrations of the species in solution for the formation of lithium phosphate precipitates. It was written in Wolfram Mathematica software. The constants used are defined in the text section 6.1.

Protonation constants, stability constants of complexes:

```
logK = {12.35, 7.199, 2.148}
b1 = {10^logK[[1]], 10^(logK[[1]] + logK[[2]]),
      10^(logK[[1]] + logK[[2]] + logK[[3]])}
Reverse[b1]
```

Ionic product of water

```
Kw = 1.0 10^-14
```

Solubility product of lithium phosphate

```
KspLi3P04 = 1.3 10^-9
```

Concentration of protonated complexes

```
HP04 = b1[[1]] H P04
```

```
H2P04 = b1[[2]] H^2 P04
```

```
H3P04 = b1[[3]] H^3 P04
```

```
b2 = 10^0.36 Kw
```

```
LiOH = b2 Li/H
```

```
cP04 = P04 + HP04 + H2P04 + H3P04
```

```
cLi = Li + LiOH
```

```
c = {}
```

```
res =
```

```

FindRoot[{(cP04 /. H -> 10^-3) == 0.03, (cLi /. H -> 10^-3) ==
  0.18}, {{P04, 0.00000003}, {Li, 0.009}}]
P040 = P04 /. res
Li0 = Li /. res

Do[
  res = FindRoot[{(cP04 /. H -> 10^-pH) ==
    0.03, (cLi /. H -> 10^-pH) == 0.18}, {{P04, P040}, {Li, Li0}}];
  P040 = P04 /. res; Li0 = Li /. res;
  s = {H -> 10^-pH, res[[1]], res[[2]]};
  AppendTo[
    c, {pH, 10^-pH, P04 /. s, HP04 /. s, H2P04 /. s, H3P04 /. s,
      Li /. s, LiOH /. s,
      If[(Li^3 P04 /. s) > KspLi3P04, 1, 0]};,
    {pH, 0, 8.5, 0.001}]

```

the generated table is exported to a directory, where it is further processed

```
Export["9-Li3P04.dat", c]
```

A parametric plot to display the amounts of the species in solution

```

ParametricPlot[
  Table[{c[[Floor[i], 1]], c[[Floor[i], j]]}, {j, 1, 6}], {i, 1,
    100}, {AspectRatio -> 1, PlotRange -> {Automatic, {0, 0.01}},
    PlotLegends -> Automatic}, Frame -> True,
  FrameStyle -> Directive[Black, Thickness[Medium]]]

```

A modification to account for the presence of lithium phosphate precipitate is as shown below;

```

logK = {12.35, 7.199, 2.148}
b1 = {10^logK[[1]], 10^(logK[[1]] + logK[[2]]),
  10^(logK[[1]] + logK[[2]] + logK[[3]])}
Reverse[b1]
Kw = 1.0 10^-14
KspLi3P04 = 1.3 10^-9

HP04 = b1[[1]] H P04
H2P04 = b1[[2]] H^2 P04

```

```

H3P04 = b1[[3]] H^3 P04

b2 = 10^0.36 Kw
LiOH = b2 Li/H

Total phosphate ion concentration

cP04 = P04 + HP04 + H2P04 + H3P04 + Li3P04s

Total lithium ion concentration
cLi = Li + LiOH + 3 Li3P04s
Calculating the actual amounts of the species
c = {}
res =
  FindRoot[{(cP04 /. H -> 10^-13.01) ==
    0.03, (cLi /. H -> 10^-13.01) ==
    0.09, (Li^3 P04 /. H -> 10^-13.01) == KspLi3P04}, {{P04,
    0.0003}, {Li, 0.001}, {Li3P04s, 0.003}}]
P040 = P04 /. res
Li0 = Li /. res
Li3P04s0 = Li3P04s /. res
Do[
  res = FindRoot[{(cP04 /. H -> 10^-pH) ==
    0.03, (cLi /. H -> 10^-pH) == 0.09, (Li^3 P04 /. H -> 10^-pH) ==
    KspLi3P04}, {{P04, P040}, {Li, Li0}, {Li3P04s, Li3P04s0}}];
  P040 = P04 /. res; Li0 = Li /. res;
  Li3P04s0 = Li3P04s /. res;
  s = {H -> 10^-pH, res[[1]], res[[2]], res[[3]]};
  AppendTo[
    c, {pH, 10^-pH, P04 /. s, HP04 /. s, H2P04 /. s, H3P04 /. s,
      Li /. s, LiOH /. s,
      Li3P04s /. s}];,
  {pH, 8.2, 14, 0.001}]

Export["6-1-Li3P04.dat", c]

ParametricPlot[Table[{c[[Floor[i], 1]], c[[Floor[i], j]]},
  {j, 1, 8}], {i, 1, 300}, {AspectRatio -> 1,
  PlotRange -> {Automatic, {0, 0.01}}, PlotLegends -> Automatic}]

```

# Acknowledgments

I would like to express my sincere gratitude to my supervisors and the leaders of the Non-Linear Dynamics group; Dr. Ágota Tóth and Dr. Dezső Horváth for granting me the opportunity to be part of their group. Their mentorship and ceaseless dedication to my research brought me this far. With their high expectations toward quality, they have transformed me into a better researcher looking back to my first year in the program. Their effort can not be forgotten. In a country thousands of kilometers away, I found a loving and caring family in them.

I would also like to use this opportunity to appreciate the rest of the members of the Non-Linear Dynamics research group, especially Dr. Gábor Schuszter, Dr. Pawan Kumar, Emese, Cinti, Edina, Paszkál, and Reka, for their support towards the success of my program. Being in Szeged exposed me to many friendly people whom I gladly call friends; Yasmin, Lilien, Judit, Ntombi, Oris, Dori, and Szábina, thank you all for your encouragement and support, and I wish you all the best in your endeavors.

To my wife lovely Magdaline, my son Dietrich, my daughter Angela, my father and late mother, my brothers, sisters, and friends back in Nigeria thank you all for your sacrifices and good wishes.

I want to also appreciate the Hungarian government through the Tempus Public Foundation which in partnership with the Nigerian government provided for my studies at the University of Szeged. Thanks to Gombe State University for granting me a study fellowship opportunity outside of Nigeria.